Novel Approaches to Mechanistic Pharmacokinetic/Pharmacodynamic Modeling

Lumping of PBPK Models and Systems Biology

Dissertation zur Erlangung des Grades
eines Doktors der Naturwissenschaften (Dr. rer. nat.)
am Fachbereich Mathematik & Informatik der Freien Universität Berlin

vorgelegt von

Sabine Pilari

April 2011

Betreuer: Prof. Dr. Wilhelm Huisinga

1. Gutachter: Prof. Dr. Christof Schütte
2. Gutachter: Dr. Frédéric Y. Bois

Tag der Disputation: 12.07.2011

Acknowledgements

First and foremost, I want to express my deep thanks to my supervisor Wilhelm Huisinga for his guidance through the past challenging but inspiring years of my life. His constant support and patience were invaluable for carrying out this project and have always been a great motivation.

I also thank my mentor from the Abbott GmbH & Co. KG, Peter Nörtersheuser, for giving me the opportunity to repeatedly present my Ph.D. project in his Pharmacometrics group. The helpful comments from an industrial point of view by many group members and in particular by Olaf Lichtenberger contributed to this thesis. My warm thanks also go to Alexander Hoffmann for the biochemical guidance on the development of the mathematical model of the IKK activation cycle and to Frédéric Y. Bois for discussions and comments on the final manuscript. My gratitude also applies to Stephan Menz, Ludivine Fronton, Valerie Nock, Ronald Niebecker for carefully proofreading parts of this thesis.

I warmly thank Christof Schütte for hosting me at the Bio Computing Group at the Freie Universität Berlin and integrating me into the academic teachings. I am particularly grateful to my friends at the Bio Computing Group, Axel Rack, Stephan Aiche, Maximilian Weiss and Jan Wigger that regularly joined me for coffee. I also want to thank the friends I made at the Hamilton Institute, my housemates Shravan Sajja Kumar and Fernando Lopez, for making my time in Ireland as enjoyable as it was.

Last and most importantly, I want to thank Martin Held who was always there for me in the past few years, listening, patiently tolerating all of my ups and downs and encouraging me in any circumstances.

The work was funded by the Graduate Research Training Program 'PharMetrX: Pharmacometrics and Computational Disease Modelling' jointly at the Martin-Luther-Universität Halle-Wittenberg, the Freie Universität Berlin, and the Universität Potsdam.

Publications

Parts of this thesis have been published during my Ph.D. studies: Section 2.2.1 has been published in the *Journal of Pharmacokinetics and Pharmacodynamics* in corporation with Wilhelm Huisinga with the title 'Lumping of Physiologically-Based Pharmacokinetic Models and a Mechanistic Derivation of Classical Compartmental Models'. Section 2.4 reflects a part of a manuscript that has been submitted for publication in the *Journal of Pharmacokinetics and Pharmacodynamics* together with Ludivine Fronton and Wilhelm Huisinga with the title 'Monoclonal Antibody Disposition beyond Target Binding: Impact of FcRn on Clearance and Derivation of Mechanistic Compartment Models'. Section 2.3 is part of a manuscript in preparation together with Alexander Solms, Ludivine Fronton and Wilhelm Huisinga.

An article not covered in this thesis has been published in the *European Journal of Pharmaceutical Sciences* with the title 'Gestational Influences on the Pharmacokinetics of Gestagenic Drugs: A Combined *In Silico*, *In Vitro* and *In Vivo* Analysis' together with Cornelia Preusse and Wilhelm Huisinga.

Contents

CHAPTER 1

Introduction

Modeling and simulation forms an integral part of various stages of drug discovery and development. In the pharmaceutical industry, modeling and simulation is used to support decision-making processes, e.g., drug candidate selection, dose selection, clinical trial design, and benefit/risk assessment for new drugs [1–6]. Yet, for a given drug, the ultimate goal is to determine the optimal dose and dosing regimen for a target population of patients to obtain the maximal desired effect while minimizing adverse events [1, 7–9]. The description and prediction of the time course of the drug effects in the patient play the most crucial role to achieve this attempt [7, 10].

The science of relating drug intake to drug effect is referred to as pharmacokinetics and pharmacodynamics [1, 7, 11]. Pharmacokinetics aims at describing all relevant processes that influence the absorption, distribution, metabolism, and excretion (ADME) of an administered drug in the body in order to describe and predict the time course of drug concentration [8, 9, 12]. Pharmacodynamics, on the other hand, aims at establishing a relationship between drug exposure and drug effect [9, 12]. By integrating pharmacokinetic and pharmacodynamic modeling the time course of drug effect in the patient can be described and predicted, see Figure 1.1 for a schematic overview.

Several methods have been developed to determine the pharmacokinetic and pharmacodynamic profile of a compound. In both domains, empirical approaches rely on evaluating experimental data by means of mathematical modeling [8, 9, 13]. In pharmacokinetics, experimental data refers to time series measurements of drug concentration in plasma or blood, whereas in pharmacodynamics, experimental data is a direct or indirect measure of drug effect, e.g., pain relief or the concentration of a certain hormone [7, 9]. In the empirical approach, the model structure and the model parameters are derived from the experimental measurements, and parameter estimation forms an integral part of model development [1, 7, 12]. A main drawback of empirical pharmacokinetic/pharmacodynamic modeling is its need for *in vivo* data that might not be accessible in certain scenarios, e.g., for children and pregnant women.

More recent approaches integrate the mechanistic understanding of biochemical, physiological and/or physical processes involved in drug disposition and drug response into pharmacokinetic/pharmacodynamic model development [3, 6, 14–16]. Here, the model structure and the model parameters are derived from the knowledge of the physiology and biochemistry of the organism and some *in vitro* and/or *ex vivo* properties of the drug under consideration [17–20]. The mechanistic models can be used to predict drug concentration and drug effect prior to *in vivo* experiments. As soon as *in vivo* measurements become available, the comparison of the data to the model predictions can be used to assess the reliability of the underlying model assumptions [14].

In pharmacokinetics, currently, the most frequently used mechanistic models are whole-body physiology-based pharmacokinetic (PBPK) models, see e.g., [6, 16, 17, 19–21]. PBPK models aim at incorporating the most relevant ADME processes involved in drug disposition and can be used to predict the time course of drug concentration in plasma or blood

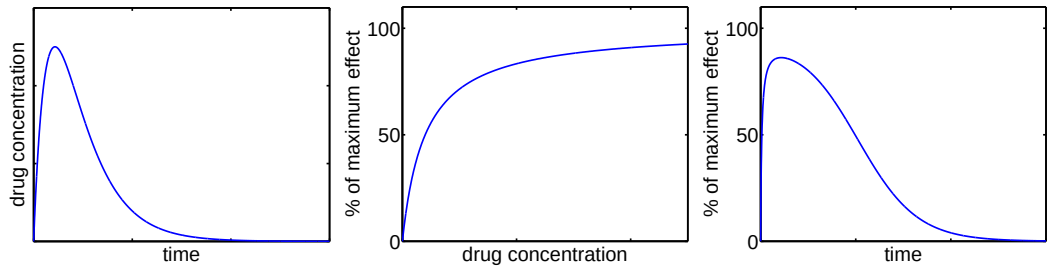

Figure 1.1: Pharmacokinetics (left) describes the concentration-time profile of the drug, i.e., simply spoken 'what the body does to the drug'. Pharmacodynamics (middle) defines the relation between drug concentration and response, i.e., simply spoken 'what the drug does to the body' [11]. Finally, combined pharmacokinetic/pharmacodynamic modeling (right) allows for describing the time course of the drug effect.

as well as in various organs and tissues prior to any *in vivo* studies, solely based on *in vitro* data. If gradually refined and evaluated against preclinical and early clinical data, a PBPK model can be seen as reflecting a coherant collection of parts of the current knowledge about a drug candidate. Such models, however, are more complex than the empirical pharmacokinetic models in terms of number of equations and parameters. Due to the increased complexity, PBPK models are less suitable, e.g., for application in a population analysis of clinical trials in later developmental stages, and for this reason, the empirical models are prevalently employed in this field of application.

So far, the classical, empirical and the physiology-based pharmacokinetic approaches are used independently or in parallel, with little to no overlap or cross-fertilization; and none of the approaches takes advantage of the other approach. Figure 1.2 schematically depicts the drug discovery and development chain and highlights the kind of modeling approach that is primarily applied at different developmental stages. In drug discovery and preclinical development, PBPK modeling is frequently used, e.g., to optimize the selection of drug candidates based on *in silico* and *in vitro* data that are likely to have the desired *in vivo* pharmacokinetic properties, and to determine the first dose in man based on preclinical data [8, 10, 14]. After entry into clinical development, there is a shift from mechanistic to empirical modeling. In particular, mechanistic PBPK modeling is underrepresented in the analysis of clinical data and is rarely used to support or guide empirical model development. So far, clinical drug development does not directly benefit from the effort that has been made to develop a PBPK model in the preclinical stage. Thus, an approach that establishes the link between the mechanistic PBPK models and the empirical models is highly desirable to bridge the gap between preclinical and clinical model development.

In pharmacodynamics, mechanism-based modeling strategies are routinely employed [7, 15, 22, 23], but in contrast to the PBPK models in pharmacokinetics, the structure and detailedness of the pharmacodynamic models varies tremendously [22, 24]. An obvious reason lies in the complexity of the biochemical processes involved in drug response and our partly limited understanding thereof. The simplest pharmacodynamic models describe the appearance or disappearance of an *in vivo* observed response by a single equation with only one or two parameters [22, 25, 26]. However, to lower risks and to preserve time and resources, it is desirable to predict the drug effect as early as possible. In drug discovery, new compounds are routinely tested for *in vitro* potency, e.g. the half maximal inhibitory drug concentration, IC_{50}, from binding assay studies. Those data can be used as a first approximation to define a concentration-response relationship [14]. However, due to the complexity of the *in vivo* system, a rationale for a reliable *in vitro-in vivo* extrapolation is hard to be defined.

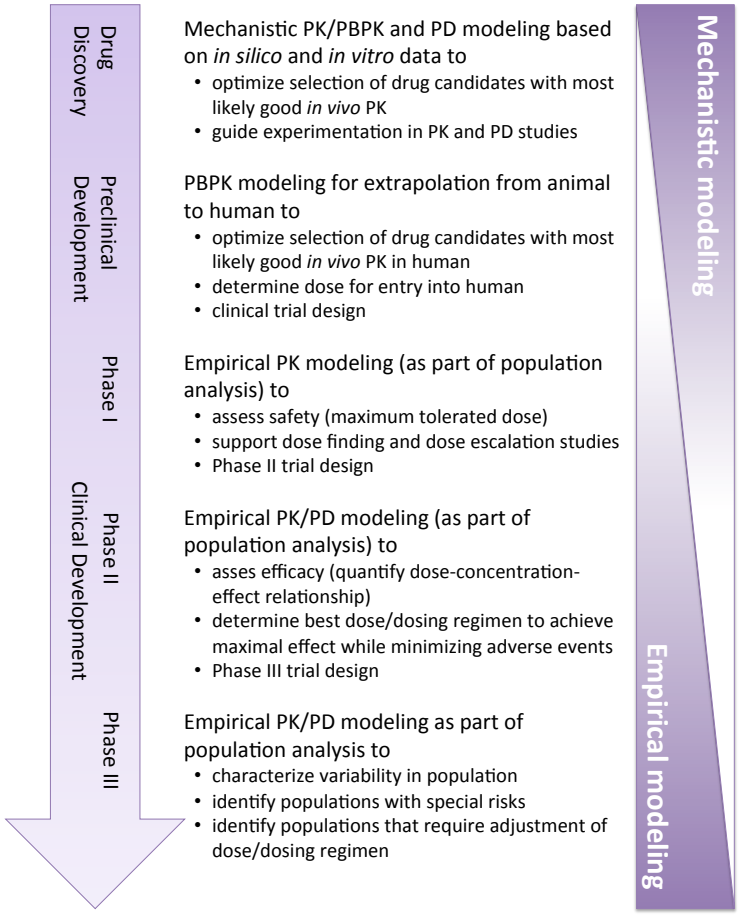

Figure 1.2: Role of pharmacokinetic (PK) and pharmacodynamic (PD) modeling in drug discovery and development. Mechanistic and physiology-based pharmacokinetic (PBPK) modeling approaches are frequently used in drug discovery and preclinical development, while in later stage clinical development empirical modeling approaches are prevalently applied.

The emerging discipline of systems biology provides a framework for considering relevant processes that may have an impact on the drug response [3, 18, 27, 28]. Systems biology models describe complex metabolic and gene-regulatory reaction networks and signaling pathways as a whole, i.e., they consider all interacting players and the corresponding reactions that take place, as e.g., association/dissociation, activation/inactivation, etc. [3, 18, 27, 28]. The detailed model structure allows for an adequate integration of the mechanism of action of a drug. For example, if a drug is known to inhibit the catalytic activity of an enzyme, an equation describing the catalytic reaction is adjusted for the presence of drug. *In vitro* information on, e.g., the IC_{50} can easily be integrated; and simulating the model yields predictions for the *in vivo* situation. Thus, the systems biology approach provides a sophisticated modeling strategy to integrate *in vitro* data to predict the drug concentration-response relationship *in vivo*. However, so far, complex systems biology models are only rarely used in the context of pharmacodynamic modeling.

In this thesis, we address the above stated problems of

i) defining the missing link between empirical pharmacokinetic and mechanistic PBPK modeling to carry the mechanistic knowledge forward into classical compartmental model development, and

ii) exemplary illustrating the application of systems biology in the context of mechanistic pharmacokinetic/pharmacodynamic modeling to *a priori* predict the *in vivo* time course of drug response.

Lumping of whole-body PBPK models to derive empirical low-dimensional compartment models

We propose to make use of the mechanistic knowledge present in a whole-body PBPK model in order to support classical compartmental model development by lumping of the PBPK model. Our approach is based on a new lumping method that determines the number and composition of lumped compartments based on the drug pharmacokinetic profiles in different organs and tissues in the body. The proposed lumping approach establishes a direct derivation of low-dimensional compartment models from PBPK models and enables a mechanistic interpretation of empirical pharmacokinetic models.

In the literature, several approaches for the reduction and lumping of whole-body PBPK models have been proposed [29–32]. These methods, however, rely on restrictive lumping rules that have difficulties to justify lumping a whole-body PBPK model to, e.g., a 1- or 2-compartment model. Such low dimensional models, however, are frequently used in all stages of the development process to describe clinical data [9, 12, 33]. In addition, only the drug concentrations in the lumped compartments are predicted by the existing lumping approaches, while no link to the drug concentration in the original organs and tissues is established (unless a tissue is left unlumped, as suggested in [30]).

Our proposed new lumping procedure overcomes these limitations. It exploits the fact that drug concentrations in different compartments of the whole-body PBPK model are often strongly kinetically dependent of each other. We quantify and exploit this dependence to establish a lumped model and to relate the lumped concentrations to the concentrations in the individual organs/tissues. We derive a general lumping strategy based on a generic whole-body PBPK model for the disposition of small molecule drugs. To inform classical pharmacokinetic model development, we introduce the concept of a minimal lumped model that allows for predicting the venous plasma/blood concentration with as few compartments as possible. The minimal lumped parameter values may serve as initial values for any subsequent parameter estimation process. By applying our lumping method to 25 diverse drugs, we identify characteristic features of lumped models for moderate-to-strong bases, weak bases and acids.

The nature of PBPK models allows for predicting the time course of drug concentrations for individuals that differ in their physiological characteristics, as e.g., organ volumes. We apply our lumping approach to analyze how the physiological variability as present in patient populations is carried forward into classical compartmental pharmacokinetic model development. This approach is a first attempt to mechanistic covariate modeling as part of a population pharmacokinetics analysis.

We additionally extend our lumping approach to support classical compartmental pharmacokinetic model development for biologics such as monoclonal antibodies. Despite the detailed knowledge about molecular processes involved in monoclonal antibody disposition, there is, so far, no established model-building strategy to translate the mechanistic understanding into pharmacokinetic model development. In this study, we derive a generic low-dimensional compartment model incorporating the mechanistic, target-independent processes involved in monoclonal antibody disposition. We exemplify our strategy for the monoclonal antibody 7E3 in mice.

Employing systems biology models in the context of mechanistic pharmacokinetic/pharmacodynamic modeling

In this thesis, we make use of a combined PBPK-systems biology modeling approach to demonstrate the utility of mechanistic modeling in early stages of drug discovery and development. As an example, we choose the down-regulation of the inflammatory biomarker

NFκB. The transcription factor NFκB is a key regulator of the innate and adaptive immune system (reviewed in e.g. [34–37]) and an increased activity of NFκB was shown for a variety of inflammatory diseases, neurodegenerative disorders, viral diseases, as well as cancer [34, 38, 39].

In the past decade, the development of NFκB inhibitors has been driven by the pharmaceutical industry [38, 39]. Currently, most NFκB inhibitors under development are selective inhibitors of the IκB kinase, IKK [38–40]. IKK can be regarded as the convergence point of all NFκB activating stimuli [35, 41–44] and, thus, inhibiting IKK activity is thought to prevent the activation of NFκB in the diseased cell. For a wide range of IKK inhibitors under development, the *in vitro* potency of inhibiting the kinase activity, that is responsible for downstream NFκB activation, has been demonstrated [39]. However, the observed *in vitro* effect has not been confirmed *in vivo* in humans since to date almost all of the IKK inhibitors under development are still in the pre-clinical stage. The regulation of IKK and NFκB activity is a complex system driven by the interaction of multiple inhibitors and activators, several phosphorylation and dephosphorylation steps, feedback loops, degradation processes etc. Due to this complexity, it is not clear from the *in vitro* observations whether the IKK inhibitors under development would be able to downregulate IKK and NFκB activation *in vivo*.

We develop a new mathematical model of the regulation of IKK activation and inactivation in the presence of drug and link it to a previously published systems biology model of the NFκB signaling pathway [45–50]. The combined IKK-NFκB model allows for relating the concentration of a given IKK inhibitor at the target site to the response of the pathway, i.e., increase or decrease in IKK and downstream NFκB activity. We show that the desired effect of IKK and NFκB activity decrease is only achieved for high drug concentrations, while for low drug concentrations, we predict the contrary effect of an increase in IKK and NFκB activity.

Integrating the systems biology model into the generic PBPK model allows for the prediction of the IKK inhibitor concentration at the target site and, thus, the concentration-dependent drug effect in each organ/tissue of the body.

CHAPTER 2

Pharmacokinetic Modeling

In drug discovery and development, empirical, low-dimensional compartment models and physiology-based pharmacokinetic (PBPK) models are successfully used to analyze and predict the pharmacokinetics of drugs. In this chapter, we develop a novel technique to carry forward prior knowledge on the pharmacokinetics of a compound given in form of a whole-body PBPK model into the development of low-dimensional pharmacokinetic models.

Motivating example. Based on a generic 13-compartment PBPK model, we derive a mechanistically lumped 3-compartment model to predict the plasma concentration-time profile for our reference compound Lidocaine in human (see right). Then, in the analysis of the Lidocaine plasma data by the empirical model fitting approach, the lumped model structure defined the model structure of the classical, empirical model and the lumped model parameters served as initial values in the parameter estimation process.

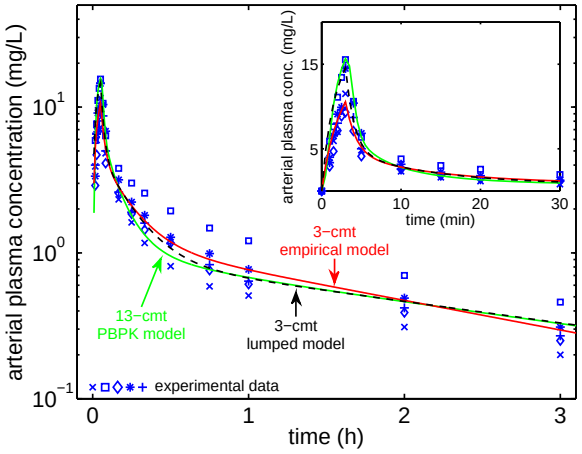

The chapter is organized as follows: In the first section, we introduce general concepts of classical, i.e., empirical, and mechanistic PBPK modeling. In the second section, we present our novel lumping strategy illustrated for the reference compound Lidocaine and additionally compare the PBPK and lumped model predictions for barbiturates in the rat. We relate the lumped model parameters to the parameters of classical compartment models and introduce the concept of a minimal lumped model that aims at predicting only the plasma or blood concentration accurately, as it is typically the case in the classical approach. We further discuss a potential influence of the route of drug administration on the lumped models and demonstrate it in the analysis of experimental Lidocaine plasma data based on both, the classical and the minimal lumping approach. Additionally, we derive characteristic features of the lumped models for moderate-to-strong bases, weak bases, and acids. The third and fourth sections deal with examples of applications of the lumping approach. On the one hand, we exploit the lumping approach to study how variability in physiological parameters (e.g., tissue volumes, blood flows) is carried forward into low-dimensional compartment models to be used in population analyses of large clinical trials. On the other hand, we use the lumping method to translate the mechanistic understanding of monoclonal antibody disposition, when the target is not expressed, given in form of a detailed PBPK model into the design of low-dimensional compartment models.

2.1 Pharmacokinetic Modeling Approaches

Pharmacokinetics (PK) is the study of the fate of a drug in the body [1, 7–9, 12, 33]. It aims at quantitatively describing the processes that influence absorption, distribution, metabolism, and elimination (ADME) of a drug in the body. To analyze the PK profile of a drug, experimentally collected data, e.g., time series measurements of drug concentration in plasma or blood, is evaluated by means of mathematical modeling [8, 9]. The classical, i.e., empirical, modeling approaches are classified into non-compartmental and compartmental methods. The non-compartmental technique relies on fitting a sum of exponentials function to the experimental data [8]. Based on the estimated parameters, typical PK characteristics are determined to characterize the drug, e.g., area under the concentration time curve (AUC), elimination half-life ($t_{1/2}$), total plasma clearance, etc. [8, 9]. Compartmental PK analysis is based on dividing the organism into spaces with identical kinetics (compartments). Both, the model structure and the model parameters, are derived from the experimental data [9, 12, 51]. The typical model finding procedure includes the development and parameter estimation of competing models. Model discrimination is based on a statistical criterion to select the model that best fits the experimental data [9, 12, 17]. The compartmental PK models can then be used to describe and predict the concentration-time profile of the drug in plasma or blood.

While the classical compartmental PK models are empirical, newer methods have been developed that are considered to be mechanistic or mechanism-based [51]. The model structure and model parameters are defined in terms of the anatomical and/or physiological characteristics of the organism and some properties of the drug under consideration. The most promising and most popular mechanistic modeling technique is physiology-based PK (PBPK) modeling [6, 16, 19–21].

2.1.1 Classical Compartmental Modeling

In classical PK modeling, the body is typically divided into one, two, or three compartments that represent distributional spaces with identical kinetics [8]. The most frequently used models are depicted in Figure 2.1. Within each compartment, drug distribution is assumed to occur instantaneously and homogeneously. The barriers between compartments represent rate-limited disposition processes, e.g., due to slow perfusion by the blood flow, limited permeability through membranes, active transporters, metabolic conversion, protein binding, distribution into tissue constituents, etc. The compartments are interconnected by first-order rate constants, while input rate constants may follow zero-order kinetics [8, 9]. Elimination is typically assumed to occur from the central compartment based on either a linear or a saturable Michaelis-Menten process [8, 9, 12].

The simplest compartment model depicts the body as a single compartment (see Figure 2.1) assuming homogenous distribution into accessible body spaces [9]. The rate of change of drug concentration after an i.v. bolus dose is described by the following ordinary differential equation (ODE):

$$V_\mathrm{d} \frac{\mathrm{d}}{\mathrm{dt}} C_1 = -\mathrm{CL} \cdot C_1 \tag{2.1}$$

with initial condition

$$C_1(t=0) = \frac{\mathrm{dose}}{V_\mathrm{d}}, \tag{2.2}$$

where V_d, denotes the volume of distribution being defined as an apparent volume into which the total amount of drug would have to distribute in order to produce the observed plasma concentration [9, 10]. It is a measure of drug distribution, e.g., small values (< 3 L) indicate that the drug is mainly present in plasma and does not translocate into tissue spaces, while values exceeding the body volume indicate that the drug distributes into tissue. CL denotes

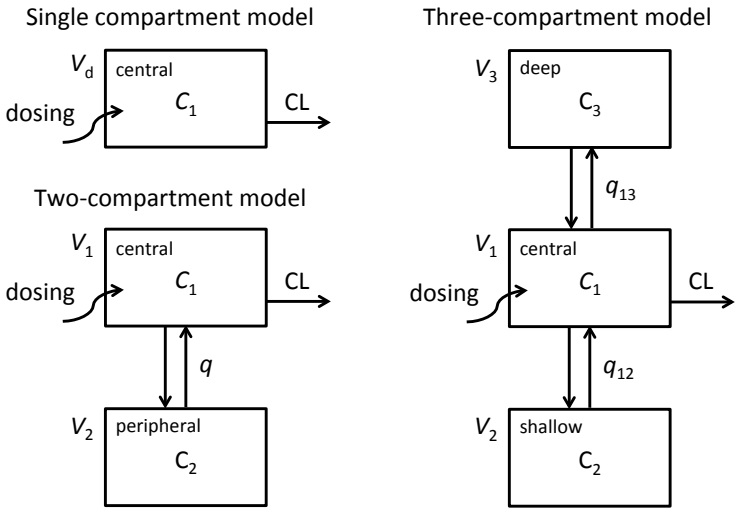

Figure 2.1: Most frequently used low-dimensional compartment models to describe drug disposition in the body. In all models, the concentration in the central compartment, C_1, represents the drug concentration at the site of measurement (plasma, blood, etc.). Within each compartment, drug distribution is assumed to be instantaneous and homogeneous. The barriers between compartments represent rate-limited disposition processes. The inter-compartmental clearances, e.g., q, q_{12}, q_{13}, account for the inflow and outflow of drug concentration. Elimination is typically assumed to occur from the central compartment with clearance, CL. The volumes of the compartments, e.g., V_1, V_2, V_3, are apparent volumes and have typically no direct physiological interpretation.

the clearance and is defined as the volume of body fluid that is cleared from the drug per unit time [9]. Since elimination may occur through multiple routes, CL as determined based on the compartmental analysis represents a sum of several individual clearance processes, as e.g., renal and bilary excretion and hepatic metabolism [9, 10].

To account for an i.v. infusion or extravascular drug administration, eq. (2.1) is amended to

$$V_{\mathrm{d}} \frac{\mathrm{d}}{\mathrm{dt}} C_1 = -\mathrm{CL} \cdot C_1 + r_{\mathrm{admin}} \qquad \text{with } C_1(t=0) = 0, \tag{2.3}$$

where r_{admin} describes the mass inflow per unit time. For an infusion, it is

$$r_{\mathrm{iv}} = \begin{cases} \mathrm{dose}/\Delta T; & t \in [T_0, T_0 + \Delta T] \\ 0; & \text{otherwise,} \end{cases} \tag{2.4}$$

where T_0 and ΔT are the starting time and the duration of the infusion, respectively. Drug absorption following, e.g., oral, intramuscular or subcutaneous drug administration is, most frequently, modeled by [8, 9, 12]

$$r_{\mathrm{abs}} = \mathrm{dose} \cdot F \cdot k_{\mathrm{a}} \cdot e^{-k_{\mathrm{a}} \cdot t}, \tag{2.5}$$

where k_{a} denotes the first order absorption rate constant. The bioavailability, F, is the fraction of dose that reaches the systemic circulation. Reasons for an incomplete oral absorption include a limited resorption from the gastrointestinal tract, e.g., due to poor solubility, metabolism by enzymes in the gut wall and an extensive first pass metabolism in the liver [8, 9]. More complex, often mechanism-based models (particularly models accounting for absorption from the gastrointestinal tract) exist, e.g., [52–55].

Two- or three-compartment models are used to describe the PK of a drug if drug disposition is rate-limited so that the whole body cannot be considered as a single, homogenous distributional space. This could be caused, e.g., by a pronounced distribution into slowly perfused tissues such as adipose (perfusion-rate limited distribution) or poor diffusion across membranes (permeability-rate limited distribution), active transporters, saturable protein binding, etc. [8, 9, 12]. The most widely-used two- and three-compartment models are depicted in Figure 2.1. For each compartment, the rate of change of drug concentration is described by an ODE. For example, the two-compartment model accounting for drug concentration in the central, C_1, and peripheral compartment, C_2, is given by

$$V_1 \frac{\mathrm{d}}{\mathrm{dt}} C_1 = q \cdot C_2 - q \cdot C_1 - \mathrm{CL} \cdot C_1 + r_{\mathrm{admin}} \tag{2.6}$$

$$V_2 \frac{\mathrm{d}}{\mathrm{dt}} C_2 = q \cdot C_1 + q \cdot C_2, \tag{2.7}$$

where $r_{\mathrm{admin}} = r_{\mathrm{iv,abs}}$ depending on the route of administration. Drug elimination is assumed to occur from the central compartment with clearance, CL, and q denotes the intercompartmental clearance.

2.1.2 Physiology-Based Pharmacokinetic Modeling

Physiology-based pharmacokinetic (PBPK) modeling makes use of the knowledge about physiological, physical and biochemical processes that are involved in drug disposition in order to predict the time course of drug concentration in various organs and tissues of the body. PBPK models are mechanistic in nature; the model structure and parameters are determined by anatomical and/or physiological characteristics of the species and physicochemical properties of the drug under consideration [6, 16, 17, 19–21]. Typically, a PBPK model consists of multiple compartments that represent the most relevant anatomical spaces of the body, e.g., single organs or tissues. The interconnections of the compartments represent transport fluids such as the blood flow or the lymph flow [6, 16, 17, 19–21].

The parameters of a PBPK model are classified to be either species- or drug-specific. Drug-specific data include physico- and biochemical properties of the compound that are ideally independent of the species, e.g., lipophilicity, ionization, protein binding, permeability, microsomal clearance. Species-specific data are related to the species only, e.g., organ volumes, blood flow rates, etc. Replacing the species-specific data, allows for extrapolation to different species or to human. To date, most PBPK models have been developed to be applied to small molecule drugs [17, 21].

A generic PBPK model for small molecule drugs

In the following, a generic PBPK model for small molecules is introduced. The model comprises 13 compartments representing the most relevant tissues, organs, and vascular spaces within the body: arterial and venous blood, lung, adipose tissue, skeleton, brain, gut, heart, kidney, liver, muscle, skin, spleen. The abbreviations for the organ/tissues names are given in Table 2.1. The topology of the model is depicted in Figure 2.2. For simplicity, the subscript 'tis' is used in the following to refer to tissues and organs.

As typically done in the generic setting and in the absence of more specific information, it is assumed that the drug distributes within the body via transport by the blood flow and via passive diffusion instantaneously and homogeneously into organs and tissues, and that the drug is metabolized in the liver. In the presence of more specific information, the generic PBPK model can be adapted accordingly, e.g., to account for active transport via membranes, excretion by the kidneys, specific protein binding, saturable metabolism etc.

Based on the perfusion-limited (well-stirred) organ model, the following ODE describes

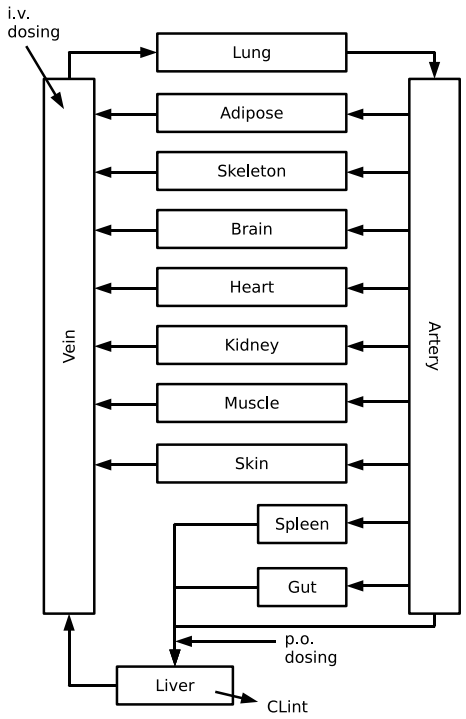

Figure 2.2: Organ and tissue topology of a generic 13-compartment PBPK model for small molecule drugs. In the generic model, only hepatic elimination is incorporated. If knowledge about further routes of elimination (e.g., renal) is available, this can easily be integrated.

the distribution processes in each non-eliminating organ/tissue:

$$V_{\text{tis}} \frac{\text{d}}{\text{dt}} C_{\text{tis}} = Q_{\text{tis}} \cdot \left(C_{\text{in,tis}} - \frac{C_{\text{tis}}}{K_{\text{tis}}} \right), \tag{2.8}$$

where C_{tis} represents the total drug concentration in the tissue part of an organ/tissue and $C_{\text{in,tis}}$ represents the inflowing concentration. In most cases, this is the arterial concentration (see below for more details). V_{tis} and Q_{tis} denote the tissue volume and the blood flow, respectively. The tissue-to-blood partition coefficient, K_{tis}, relates the steady state tissue concentration to the steady state concentration in the vascular part of an organ/tissue:

$$K_{\text{tis}} = \frac{C_{\text{tis,ss}}}{C_{\text{blood,ss}}}. \tag{2.9}$$

Thus, in eq. (2.8), the term $C_{\text{tis}}/K_{\text{tis}}$ denotes the blood concentration leaving the compartment. Since metabolism is assumed to occur in the liver, the corresponding ODE is

$$V_{\text{liv}} \frac{\text{d}}{\text{dt}} C_{\text{liv}} = Q_{\text{liv}} \cdot \left(C_{\text{in,liv}} - \frac{C_{\text{liv}}}{K_{\text{liv}}} \right) - \text{CL}_{\text{int}} C_{\text{liv}}, \tag{2.10}$$

where CL_{int} denotes the hepatic intrinsic clearance. Alternatively, some PBPK models assume that only the unbound drug concentration in liver tissue is subject to degradation, resulting in a term $\text{CL}_{\text{int}} C_{\text{u,liv}}$ instead of $\text{CL}_{\text{int}} C_{\text{liv}}$. Assuming that $C_{\text{u,liv}} = \text{fu}_{\text{liv}} C_{\text{liv}}$ with fu_{liv} denoting the hepatic fraction unbound, this could easily be integrated in the generic PBPK model by changing CL_{int} to $\text{CL}_{\text{int}} \text{fu}_{\text{liv}}$.

For the artery and vein compartments, the ODEs are

$$V_{\text{art}} \frac{\text{d}}{\text{dt}} C_{\text{art}} = Q_{\text{co}} \cdot (C_{\text{in,art}} - C_{\text{art}}) \tag{2.11}$$

$$V_{\text{ven}} \frac{\text{d}}{\text{dt}} C_{\text{ven}} = Q_{\text{co}} \cdot (C_{\text{in,ven}} - C_{\text{ven}}), \tag{2.12}$$

where Q_{co} denotes the cardiac output. For all organs, except lung, artery, liver, and vein, the inflowing concentration, $C_{\mathrm{in,tis}}$, is given by

$$C_{\mathrm{in,tis}} = C_{\mathrm{art}}. \tag{2.13}$$

For the lung and artery, it is

$$C_{\mathrm{in,lun}} = C_{\mathrm{ven}} \tag{2.14}$$
$$C_{\mathrm{in,art}} = C_{\mathrm{lun}} \tag{2.15}$$

The inflowing concentrations into the liver and venous compartments are defined by the blood flow weighted sum of all organ concentrations supplying these compartments. For the liver, it is

$$C_{\mathrm{in,liv}} = \frac{1}{Q_{\mathrm{liv}}} \sum_{\mathrm{tis}} Q_{\mathrm{tis}} C_{\mathrm{tis}}, \tag{2.16}$$

where the sum is taken over spleen, gut, and arterial hepatic vein. For the vein, it is

$$C_{\mathrm{in,ven}} = \frac{1}{Q_{\mathrm{co}}} \sum_{\mathrm{tis}} Q_{\mathrm{tis}} C_{\mathrm{tis}}, \tag{2.17}$$

where the sum is taken over adipose tissue, skeleton, brain, heart, kidney, muscle, liver, skin.

Frequently used routes of drug administration comprise i.v. bolus administration, i.v. infusion and p.o. administration. This requires to extend the venous blood and the liver ODE correspondingly. For a bolus i.v. administration, the initial condition for the system of ODEs is set to $C_{\mathrm{ven}}(t = 0) = \mathrm{dose}/V_{\mathrm{ven}}$, while all other initial concentrations are set to zero. For an i.v. infusion, the venous ODE has to be changed to

$$V_{\mathrm{ven}} \frac{\mathrm{d}}{\mathrm{dt}} C_{\mathrm{ven}} = Q_{\mathrm{ven}} \cdot (C_{\mathrm{in,ven}} - C_{\mathrm{ven}}) + r_{\mathrm{iv}}, \tag{2.18}$$

where 'r_{iv}' denotes the mass influx due to an i.v. infusion given by eq. (2.4)

$$r_{\mathrm{iv}} = \begin{cases} \mathrm{dose}/\Delta T; & t \in [T_0, T_0 + \Delta T] \\ 0; & \text{otherwise,} \end{cases}$$

with starting time T_0 and duration ΔT. In the case of a p.o. drug administration, the liver ODE has to be amended to

$$V_{\mathrm{liv}} \frac{\mathrm{d}}{\mathrm{dt}} C_{\mathrm{liv}} = Q_{\mathrm{liv}} \cdot \left(C_{\mathrm{in,liv}} - \frac{C_{\mathrm{liv}}}{K_{\mathrm{liv}}} \right) - \mathrm{CL}_{\mathrm{int}} C_{\mathrm{liv}} + r_{\mathrm{po(F_{F\cdot G})}}, \tag{2.19}$$

where '$r_{\mathrm{po(F_{F\cdot G})}}$' denotes the mass influx due to a p.o. administration. For a first order absorption model, it is

$$r_{\mathrm{po(F_{F\cdot G})}} = \mathrm{dose} \cdot F_{\mathrm{F\cdot G}} \cdot k_{\mathrm{a}} \cdot e^{-k_{\mathrm{a}} \cdot t}, \tag{2.20}$$

where k_{a} denotes the first order absorption rate constant and $F_{\mathrm{F\cdot G}}$ denotes the product of the fraction absorbed, F_{F}, and fraction not metabolized in the gut, $F_{\mathrm{G}} = (1 - \mathrm{E_{gut}})$. Using the hepatic extraction ratio $\mathrm{E_{hep}}$ (see eq. (2.24) below), it is

$$F = (1 - \mathrm{E_{hep}}) \cdot \underbrace{(1 - \mathrm{E_{gut}}) \cdot F_{\mathrm{F}}}_{F_{\mathrm{F\cdot G}}}, \tag{2.21}$$

where F denotes the bioavailability of the compound. Based on eqs. (2.20) and (2.21), we

obtain the absorption model defined in eq. (2.5):

$$r_{\mathrm{po(F)}} = \mathrm{dose} \cdot F \cdot k_{\mathrm{a}} \cdot e^{-k_{\mathrm{a}} \cdot t},$$

in which case the oral absorption model already accounts for hepatic extraction.

Parameterization

A PBPK model requires species-specific anatomical and physiological parameters in addition to drug-specific data. In the following, we consider the standard male adult with a body weight of 73 kg, a body height of 1.76 m and a cardiac output of 6.5 L/min [56, 57]. All tissue volumes and blood flow rates are listed in Table 2.1. The tissue volumes were derived from the respective tissue masses reported in [56] and the tissue densities. For all tissues except adipose and skeleton, the tissue density is approximately 1 g/mL [58]. For adipose and skeleton, it is 0.92 g/mL and 1.3 g/mL, respectively [56, 58]. In the generic PBPK model, the adipose compartment refers to the separable adipose tissue and the muscle compartment refers to the total skeletal muscle listed in [56]. The volume of the gut is the sum of the volumes of small intestine wall, large intestine left and right colon, and rectosigmoid wall. The blood flow rates were taken from [56]. The organs/tissues considered in the PBPK model account for 93.4 % of total body weight and 92.5 % of the cardiac output. For consistency, the blood flow rates of lung, artery, and vein were set to 92.5 % of the cardiac output.

Table 2.1: Tissue-specific data of the human PBPK model. All data refer to the standard male adult with a body weight of 73 kg, a body height of 1.76 m and a cardiac output of 6.5 L/min [56, 57]. The tissue volumes, not including blood, were taken from [56] underlying a tissue density of 1 g/mL for all tissues except adipose and skeleton [58]. For adipose and skeleton, it was 0.92 g/mL and 1.3 g/mL, respectively [56, 58]. The tissues and organs of the PBPK model account for 93.4 % of the body weight and 92.5 % of the cardiac output. For consistency, the blood flow of lung, artery, and vein is set to 92.5 % of the cardiac output. The right column shows the tissue-to-blood partition coefficient, K_{tis}, for our reference drug Lidocaine. K_{tis} (see eq. (2.22)) were predicted based on the tissue-to-unbound partition coefficient according to [59–62].

		tissue volume (L)	blood flow (L/min)	tissue-to-blood partition coefficient
Adipose	(adi)	15.76[a]	0.325	1.508
Brain	(bra)	1.45	0.780	1.847
Gut	(gut)	1.02[b]	0.910	3.536
Heart	(hea)	0.33	0.260	2.993
Kidney	(kid)	0.31	1.235	5.880
Liver	(liv)	1.80	1.658	5.615
Lung	(lun)	0.50	6.013	4.550
Muscle	(mus)	29.00[c]	1.105	2.435
Skeleton	(ske)	8.08[d]	0.325	1.903
Skin	(ski)	3.30	0.325	2.090
Spleen	(spl)	0.15	0.195	3.946
Artery	(art)	1.56	6.103	–
Vein	(ven)	3.74	6.103	–

[a] separable adipose tissue
[b] sum of small intestine wall, large intestine left and right colon wall and rectosigmoid wall
[c] skeletal muscle
[d] total skeleton

Table 2.2: Physicochemical and pharmacokinetic data of 25 diverse compounds.

Drug	pK_a	$\log P_{ow}$	fu^p	B:P	CL_{blood} mL/min/kg
Moderate-to-strong bases					
Amitriptyline	9.40[a]	4.90[a]	0.056[a]	0.86[a]	12.00[b]
Caffeine	10.40[a]	−0.09[a]	0.700[a]	1.04[a]	1.40[c]
Desipramine	10.32[a]	4.90[a]	0.190[a]	0.96[a]	12.00[b]
Diltiazem	7.70[a]	2.67[a]	0.200[a]	1.03[a]	12.00[b]
Diphenhydramine	8.98[a]	3.31[a]	0.089[a]	0.80[a]	9.50[b]
Imipramine	9.50[a]	4.80[a]	0.130[a]	1.12[a]	12.00[b]
Lidocaine	8.01[a]	2.26[a]	0.296[a]	0.84[a]	15.00[c]
Metoprolol	9.70[a]	2.15[a]	0.900[a]	1.14[a]	12.15[c]
Pindolol	8.80[a]	1.75[a]	0.410[a]	0.81[a]	4.20[c]
Sildefanil	7.60[a]	2.75[a]	0.040[a]	0.62[a]	6.00[c]
Theophylline	8.71[a]	0.26[a]	0.600[a]	0.83[a]	0.65[c]
Weak bases					
Alprazolam	2.40[d]	2.09[d]	0.320[b]	0.78[b]	0.76[b]
Diazepam	3.38[d]	2.84[d]	0.013[b]	0.71[b]	0.60[b]
Flunitrazepam	1.80[d]	2.06[d]	0.250[e]	1.20[e]	9.80 (mL/min)[e]
Midazolam	6.01[d]	3.15[d]	0.050[b]	0.53[b]	8.70[b]
Triazolam	2.00[d]	2.42[d]	0.100[b]	0.62[b]	4.70[b]
Acids					
Amobarbital	7.90[d]	1.89[d]	0.390[b]	1.50[b]	0.35[b]
Diclofenac	4.15[f]	3.90[f]	0.005[b]	0.55[b]	7.60[b]
Hexobarbital	8.29[d]	1.74[d]	0.530[b]	1.00[b]	3.60[b]
Ibuprofen	4.70[d]	4.06[d]	0.010[b]	0.55[b]	1.50[b]
Methohexital	8.30[d]	1.72[d]	0.270[b]	0.70[b]	16.00[b]
Thiopental	7.53[d]	2.93[d]	0.180[d]	0.88[h]	2.02[i]
Tolbutamide	5.29[d]	2.39[d]	0.040[b]	0.55[b]	0.36[b]
Valproate	4.60[d]	2.76[d]	0.099[d]	0.55[j]	0.11[j]
Warfarin	5.08[g]	3.00[g]	0.010[b]	0.55[b]	0.081[b]

[a][63], [b][64], [c][65], [d][66], [e][67], [f][68], [g][69], [h][70], [i][71], [j][72]

Physicochemical and pharmacokinetic data for a number of drugs from different classes are summarized in Table 2.2. The tissue-to-blood partition coefficients, K_{tis}, are determined from the tissue-to-unbound plasma partition coefficient, $K_{tis}^{t:up}$, via the relation

$$K_{tis} = \frac{fu^p}{B:P} K_{tis}^{t:up}, \tag{2.22}$$

where fu^p and B:P are the fraction unbound in plasma and the blood-to-plasma ratio, respectively. A method to a priori predict $K_{tis}^{t:up}$ is introduced in [59–62]. The predicted $K_{tis}^{t:up}$ values agree with experimental values within a factor of three in 84-89 % of the tested cases (reported for the species rat [59, 61]). Situations that can give rise to under- or over-predictions of $K_{tis}^{t:up}$ values include active transport processes, non-linear pharmacokinetics and binding to tissue constituents not accommodated in the mechanistic equations.

Additionally, insufficiently long infusion times for the experimental determination of $K_{\text{tis}}^{\text{t:up}}$ result in deviations between *in silico* and *in vivo* values. Drug-specific input parameters are fu^{p}, pK_{a}, $\log P_{\text{ow}}$ and potentially B:P. For our reference compound Lidocaine, the numerical values of K^{tis} are listed in Table 2.1. Further approaches to a priori predict the tissue-to-unbound plasma partition coefficients are presented in [73–75].

While often the intrinsic clearance, CL_{int}, is used to model the hepatic metabolism in PBPK models, clinical studies and associated pharmacokinetic analyses usually use the hepatic blood clearance, CL_{blood}. Employing the widely used well-stirred liver model [9], both are related according to

$$\text{CL}_{\text{blood}} = \frac{Q_{\text{liv}}\text{CL}_{\text{int}}K_{\text{liv}}}{Q_{\text{liv}} + \text{CL}_{\text{int}}K_{\text{liv}}}, \tag{2.23}$$

where K_{liv} denotes the liver tissue-to-blood partition coefficient and Q_{liv} is the hepatic blood flow. For later reference, the hepatic extraction ratio, E_{hep}, is defined as

$$\text{E}_{\text{hep}} = \frac{\text{CL}_{\text{int}}K_{\text{liv}}}{Q_{\text{liv}} + \text{CL}_{\text{int}}K_{\text{liv}}}, \tag{2.24}$$

with $0 \leq \text{E}_{\text{hep}} \leq 1$.

Given a PBPK model, the volume of distribution at steady state, V_{ss}, can be readily estimated by [10]

$$V_{\text{ss}} = V_{\text{ven}} + V_{\text{art}} + \sum_{\text{tis}} V_{\text{tis}}K_{\text{tis}} + V_{\text{liv}}K_{\text{liv}}(1 - \text{E}_{\text{hep}}), \tag{2.25}$$

where the sum is taken over all non-eliminating organs/tissues of the detailed PBPK model.

2.2 Lumping of Physiology-Based Pharmacokinetic Models

In the sequel, we describe our novel lumping approach. The drug Lidocaine serves as reference compound to demonstrate the lumping of the generic, perfusion rate-limited PBPK model introduced in section 2.1.2. We also illustrate our lumping approach for a mixed perfusion and permeability rate-limited PBPK model that has been developed to describe the disposition of barbiturates in the rat [76]; and we present lumping results for a diverse set of compounds (listed in Table 2.2).

The drug Lidocaine is typically indicated in the treatment of ventricular arrhythmias, as a local anesthetic, and in the management of status epilepticus [8, 77–80]. In the treatment of ventricular arrhythmia or in the management of status epilepticus, Lidocaine therapy is typically initiated with an i.v. bolus dose followed by a continuos i.v. infusion to maintain effective drug concentrations [78, 80]. Therapeutic concentrations range from 2-6 mg/L [8], whereas no more than 600 mg should be given in any 12 hour period [77].

For illustration purposes, we assume that Lidocaine is administered via a 60 min infusion. We choose a total dose of 400 mg Lidocaine so that after approximately 10 min a blood concentration within the therapeutic window is reached (see Figure 2.3, vein). For reasonable comparison of lumping results for a diverse set of compounds, we base the simulations on the same route of administration for all drugs. As for Lidocaine, we assume that all of the drugs are given via a 60 min i.v. infusion even though infusion may not be the proper route of drug administration for some of these drugs. Exemplified for Lidocaine, we also discuss the influence of the route of drug administration on the lumped model and we compare the PBPK modeling and lumping results to experimental data from [81].

Pilari, S. and Huisinga, W.: Lumping of Physiologically-Based Pharmacokinetic Models and a Mechanistic Derivation of Classical Compartmental Models. Journal of Pharmacokinetics and Pharmacodynamics, 37.2010,4. 365-405 S.

2.2.1 A Novel Approach to Lumping of Whole-Body PBPK Models

The original article is online available at http://dx.doi.org/10.1007/s10928-010-9165-1

Figure 2.3. shows the simulation results of the generic whole-body PBPK model for Lidocaine following a 60 min infusion of 400 mg. The predicted concentration-time profiles in the different organs, tissues and blood compartments of the PBPK model are the input data for our lumping approach.

(a) Identification of organs and tissues to be lumped together

Figure 2.4 (left) is the key to understand the new lumping method. It depicts *normalized* concentration-time profiles of all 13 compartments of the detailed PBPK model (for Lidocaine). Each concentration-time profile $C_{\text{tis}}(t)$ was normalized by its elimination-corrected tissue-to-blood partition coefficient

$$\widehat{K}_{\text{tis}} = K_{\text{tis}}(1 - \text{E}_{\text{tis}}) \tag{2.26}$$

resulting in

$$\text{Normalized Concentration} = \frac{C_{\text{tis}}(t)}{\widehat{K}_{\text{tis}}}, \tag{2.27}$$

where E_{tis} denotes the tissue extraction ration. For non-eliminating organs/tissues, it is $\text{E}_{\text{tis}} = 0$. In the generic PBPK model, the liver is the only extracting organ/tissue, in which case E_{liv} denotes the hepatic extraction ratio as defined in eq. (2.24). For artery and vein, we formally set $\widehat{K}_{\text{art}} = \widehat{K}_{\text{ven}} = 1$.

In Figure 2.4 (left) two distinct phases can be identified: (i) an initial transient phase resulting from distributional processes; and (ii) a quasi-steady state elimination phase (approximately after 4 h). Apparently, the "kinetic diversity" of concentration-time profiles is much smaller than the potential 13 dimensions of the PBPK model. We easily identify four

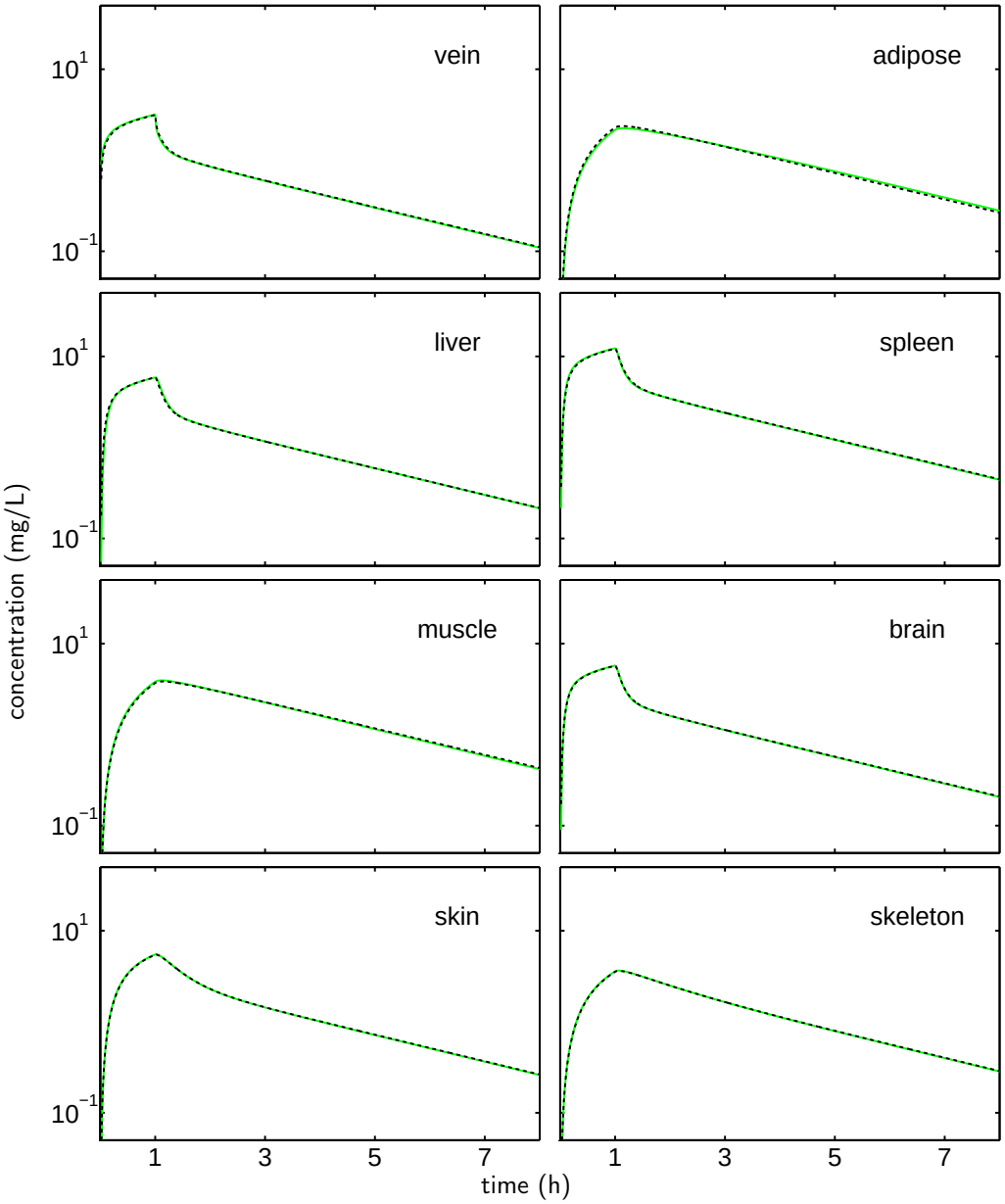

Figure 2.3: Predictions of the 13-compartment whole-body PBPK model (green solid lines) and the lumped 4-compartment model (black dashed lines) following a 60 min infusion of 400 mg of Lidocaine in human for eight representative organs/tissues. The detailed PBPK model and the lumped model show excellent agreement.

different groups of organs/tissues with almost identical normalized concentration-time profiles: {skeleton}, {adipose, muscle}, {skin} and {rest = all remaining tissues and organs}. These four groups defined the lumped compartments of the reduced model for Lidocaine. Since the generic PBPK model is linear, the grouping does not depend on the administered dose.

A slightly different scaling gives further insight about the elimination phase. In Figure 2.4 (right), the concentration-time profiles of all 13 compartments of the detailed PBPK model are scaled according to $C_{\text{tis}}(t)/C_{\text{tis}}(t_{\text{el}})$, where the time t_{el} has been chosen to lie safely in the quasi-steady state elimination phase (e.g., $t_{\text{el}} = 8$ h for Lidocaine).

This scaling shows more clearly the differences in the initial distributional phase and

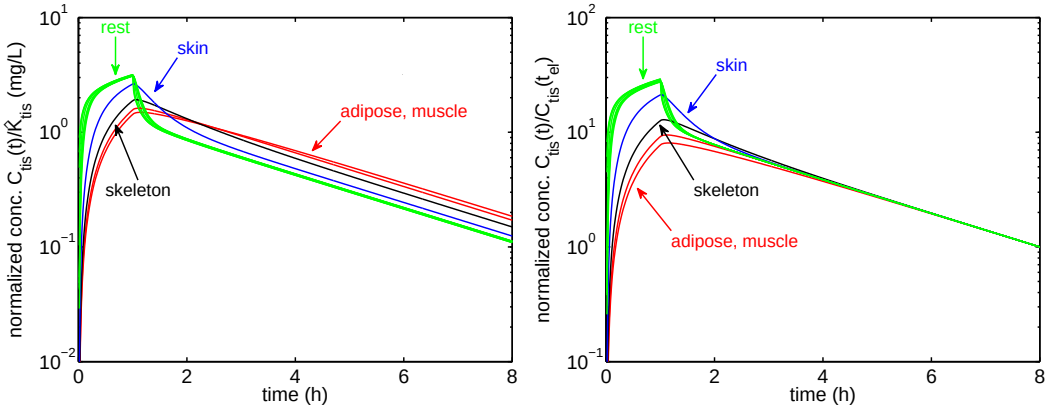

Figure 2.4: Normalized tissue concentrations for Lidocaine based on predictions of the detailed 13-compartment PBPK model. Left: Normalization of tissue concentrations $C_{\text{tis}}(t)$ based on the elimination-corrected tissue-to-blood partition coefficient $\widehat{K}_{\text{tis}}$ (see eq. (2.26)). Vein and artery were not scaled. Right: Normalization of tissue concentrations $C_{\text{tis}}(t)$ based on the concentration $C_{\text{tis}}(t_{\text{el}})$ at some timeâ t_{el} associated with the elimination phase (for non-eliminating tissues/organs and correspondingly for eliminating organs, artery and vein). We chose $t_{el} = 8$ h in this example. Identical colors indicate the proposed grouping of organs according to similar concentration-time profiles. Data correspond to a 60 min infusion of 400 mg Lidocaine.

the identical decay in the elimination phase. It can alternatively be obtained from the first one by including a factor SF_{tis} into the scaling factor $\widehat{K}_{\text{tis}}$, such that $C_{\text{tis}}(t_{\text{el}}) = \widehat{K}_{\text{tis}} \cdot \text{SF}_{\text{tis}}$. This additional factor has a physiological interpretation: The normalized concentrations $C_{\text{tis}}(t)/\widehat{K}_{\text{tis}}$ correspond to the venous blood concentrations leaving the compartments (by definition of the tissue-to-blood partition coefficient). Figure 2.4(left) shows that venous blood concentrations leaving the compartments are *not* identical in the elimination phase. Since the liver is continuously eliminating drug from the blood, there is a net loss of drug from each compartment as a result of the decreasing concentration in the perfusing blood. This net loss depends on both, physiological parameters (like blood flows and organ volumes), as well as drug-specific parameters, and is determining the additional factor SF_{tis}.

In summary, we used the normalized concentration-time profiles in Figure 2.4(left) to identify groups of compartments of the detailed PBPK model that behave kinetically similar. While the organs to be lumped were identified based on visual inspection, an automated procedure to identify organs with similar kinetics was derived based on linear dependence of the normalized concentration-time profiles (see Appendix B.4 for details).

(b) Lumping condition

In accordance with Figure 2.4(left), organs/tissues are lumped together based on the following

Lumping criteria:

$$\frac{C_1(t)}{\widehat{K}_1} = \frac{C_2(t)}{\widehat{K}_2} = ... = \frac{C_n(t)}{\widehat{K}_n}, \tag{2.28}$$

where C_1, C_2, C_n refer to compartments to be lumped together. In practice, we require to hold it only approximately, i.e., it is only required that the normalized concentrations are (very) close to each other, as it is also done in existing lumping approaches.

It is worth noticing that the above lumping criteria does not make any assumptions on whether organs or compartments are in series or parallel, as the lumping method by Nestorov *et al.* [29] does. By definition, the central compartment ('cen') is the lumped compartment

that contains the vein; and the lumped compartment that contains the liver is denoted as 'Liv'.

(c) Parameters of the lumped compartments

The volume of a lumped compartment, V_{L}, is defined as

$$V_{\mathrm{L}} = \sum_{\mathrm{tis}} V_{\mathrm{tis}}, \tag{2.29}$$

where the sum is taken over all original tissues/organs that are lumped together. The concentration of the lumped compartment, C_{L}, is determined based on the conservation of mass as

$$C_{\mathrm{L}}(t) = \frac{1}{V_{\mathrm{L}}} \sum_{\mathrm{tis}} V_{\mathrm{tis}} C_{\mathrm{tis}}(t). \tag{2.30}$$

Exploiting the lumping criteria and dividing the above equation by the blood concentration, C_{blood}, yields the defining equation for the tissue-to-blood partition coefficient, K_{L},

$$K_{\mathrm{L}} = \frac{1}{V_{\mathrm{L}}} \sum_{\mathrm{tis}} V_{\mathrm{tis}} \widehat{K}_{\mathrm{tis}}, \tag{2.31}$$

where we formally set $\widehat{K}_{\mathrm{ven}} = \widehat{K}_{\mathrm{art}} = 1$. For any lumped compartment except the central compartment, the lumped blood flow, Q_{L}, is given by

$$Q_{\mathrm{L}} = \sum_{\mathrm{tis}} Q_{\mathrm{tis}}, \tag{2.32}$$

where the sum is taken over all compartments that are lumped together into 'L'. The blood flow Q_{cen} of the central compartment is defined as

$$Q_{\mathrm{cen}} = \sum_{\mathrm{L}} Q_{\mathrm{L}}, \tag{2.33}$$

where the sum is taken over all lumped compartments supplying the central compartment.

(d) Differential equations for the lumped compartments

Based on eq. (2.30) equations for the rate of change of the concentration in the lumped compartment are derived. The derivation is given in Appendix B.2. For each lumped compartment except the central compartment, it is

$$V_{\mathrm{L}} \frac{\mathrm{d}}{\mathrm{dt}} C_{\mathrm{L}} = Q_{\mathrm{L}} \cdot \left(\frac{C_{\mathrm{cen}}}{K_{\mathrm{cen}}} - \frac{C_{\mathrm{L}}}{K_{\mathrm{L}}} \right). \tag{2.34}$$

For the central compartment, there are two situations. If the liver is part of the central compartment, it is

$$V_{\mathrm{cen}} \frac{\mathrm{d}}{\mathrm{dt}} C_{\mathrm{cen}} = Q_{\mathrm{cen}} \cdot \left(C_{\mathrm{in,cen}} - \frac{C_{\mathrm{cen}}}{K_{\mathrm{cen}}} \right) - \mathrm{CL}_{\mathrm{blood}} \frac{C_{\mathrm{cen}}}{K_{\mathrm{cen}}} + r_{\mathrm{iv,po(F)}}, \tag{2.35}$$

where $\mathrm{CL}_{\mathrm{blood}}$ denotes the hepatic blood clearance defined in eq. (2.23). The inflowing concentration is given by

$$C_{\mathrm{in,cen}} = \frac{1}{Q_{\mathrm{cen}}} \sum_{\mathrm{L}} Q_{\mathrm{L}} \frac{C_{\mathrm{L}}}{K_{\mathrm{L}}}, \tag{2.36}$$

and the sum is taken over all lumped compartments except the central compartment.
In case the liver is not part of the central compartment, it is

$$V_{\text{cen}} \frac{\mathrm{d}}{\mathrm{dt}} C_{\text{cen}} = Q_{\text{cen}} \cdot \left(C_{\text{in,cen}} - \frac{C_{\text{cen}}}{K_{\text{cen}}} \right) - \text{CL}_{\text{blood}} \frac{C_{\text{Liv}}}{K_{\text{Liv}}} + r_{\text{iv}}, \tag{2.37}$$

while for the 'Liv' compartment, it is

$$V_{\text{Liv}} \frac{\mathrm{d}}{\mathrm{dt}} C_{\text{Liv}} = Q_{\text{Liv}} \cdot \left(\frac{C_{\text{cen}}}{K_{\text{cen}}} - \frac{C_{\text{Liv}}}{K_{\text{Liv}}} \right) + r_{\text{po}(\text{F}_{\text{F·G}})}. \tag{2.38}$$

The incoming concentration $C_{\text{in,cen}}$ in eq. (2.37) is defined as in eq. (2.36). Note the difference in the dosing term; while it is $F = (1 - \text{E}_{\text{hep}})F_{\text{F·G}}$ in the dosing term of eq. (2.35), it is $F_{\text{F·G}}$ in the dosing term of eq. (2.38). Also note that eq. (2.35) is actually a special case of eq. (2.37). In the latter case, the term $C_{\text{Liv}}/K_{\text{Liv}}$ corresponds to the concentration of blood leaving the lumped compartment that contains the liver, which is identical to the blood concentration of the central compartment in the case, the liver is part of the central compartment according to eqs. (2.39) and (2.40).

(e) Prediction of individual organ/tissue concentrations

Based on the lumping criteria, individual concentrations of the organs/tissues are easily regained from the lumped concentrations. This process amounts to reversing the lumping procedure. Based on the concentration C_{L} and tissue-to-blood partition coefficient K_{L} of the lumped compartment, the original organ/tissue concentrations are given by

$$C_{\text{tis}} = \widehat{K}_{\text{tis}} \cdot \frac{C_{\text{L}}}{K_{\text{L}}} \tag{2.39}$$

For the venous blood, it is

$$C_{\text{ven}} = \frac{C_{\text{cen}}}{K_{\text{cen}}}. \tag{2.40}$$

It is important to notice that the scaled concentration $C_{\text{cen}}/K_{\text{cen}}$ rather then C_{cen} itself is the venous blood concentration that is to be compared to experimental data. The blood concentration can be related to the plasma concentration by $C_{\text{plasma}} = C_{\text{ven}}/\text{B:P}$ using the blood-to-plasma ratio B:P.

(f) Step-by-step lumping procedure

In summary, the proposed lumping scheme comprises the following steps:

1. Simulate the whole-body PBPK model to predict the concentrations $C_{\text{tis}}(t)$ in all organs and tissues.

2. Plot the normalized concentrations according to eq. (2.27) and identify the groups of organs/tissues with similar normalized concentration-time profiles.

3. For each group of organs/tissues, determine the lumped volume, the lumped blood flow and the lumped partition coefficient according to eqs. (2.29), (2.31)-(2.33).

4. Use eqs. (2.34)-(2.36) or eqs. (2.36)-(2.38) to simulate the lumped model and to predict the lumped concentrations, C_{L}, for all groups of organs/tissues.

5. Use eqs. (2.39)-(2.40) to predict the original organ/tissue concentration, C_{tis}, from C_{L} for each group of lumped organs/tissues.

(g) Volume of distribution

The volume of distribution at steady state V_{ss} is defined as

$$V_{\mathrm{d}} = \frac{A_{\mathrm{ss.tot}}}{C_{\mathrm{ss,ven}}}, \tag{2.41}$$

where $A_{\mathrm{ss,tot}}$ denotes the total amount of drug in the body and $C_{\mathrm{ss,ven}}$ the venous blood concentration in steady state. Since the tissue-to-blood partition coefficients K_{tis}, are the ratios of the steady state concentration in tissue to the steady state concentration in blood, and exploiting eqs. (2.29) and (2.31), it is

$$V_{\mathrm{ss}} = \sum_{\mathrm{L}} V_{\mathrm{L}} K_{\mathrm{L}} \tag{2.42}$$

$$= V_{\mathrm{ven}} + V_{\mathrm{art}} + \sum_{\mathrm{tis}} V_{\mathrm{tis}} \widehat{K}_{\mathrm{tis}}, \tag{2.43}$$

where the first sum is taken over all compartments of the lumped model, and the second sum is taken over all tissues/organs of the detailed PBPK model. Hence, the lumping method preserves the volume of distribution V_{ss}, which is identical to the volume of distribution of the original PBPK model (see eq. (2.25)). Importantly, preservation of V_{ss} does not depend on whether the liver is part of the central or of a peripheral lumped compartment.

Lumping of the 13-compartment generic PBPK model for Lidocaine

Figure 2.3 shows the predicted concentration-time profiles for the different organs/tissues based on the lumped 4-compartment model in comparison to the 13-compartment PBPK model for Lidocaine. The lumped 4-compartment model represents the groups of concentration-time profiles identified in Figure 2.4: {skeleton}, {adipose, muscle}, {skin}, and the central compartment containing all remaining organs {vein, artery, lung, brain, heart, kidney, gut, spleen, liver}. The corresponding set of ODEs and lumped parameters were derived

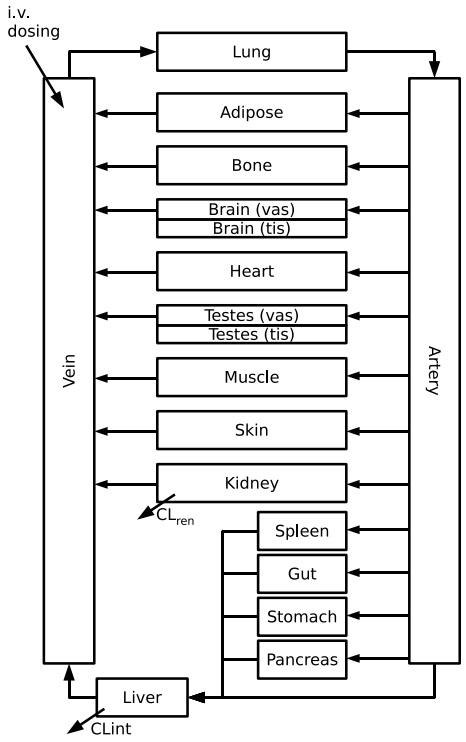

Figure 2.5: Organ and tissue topology of the detailed 18-compartment PBPK model for barbiturate in the rat. Distribution in testes and brain was assumed to be permeability-rate limited, while it was assumed to be perfusion-rate limited for all remaining tissues and organs. The required species- as well as drug-specific data are given in [76].

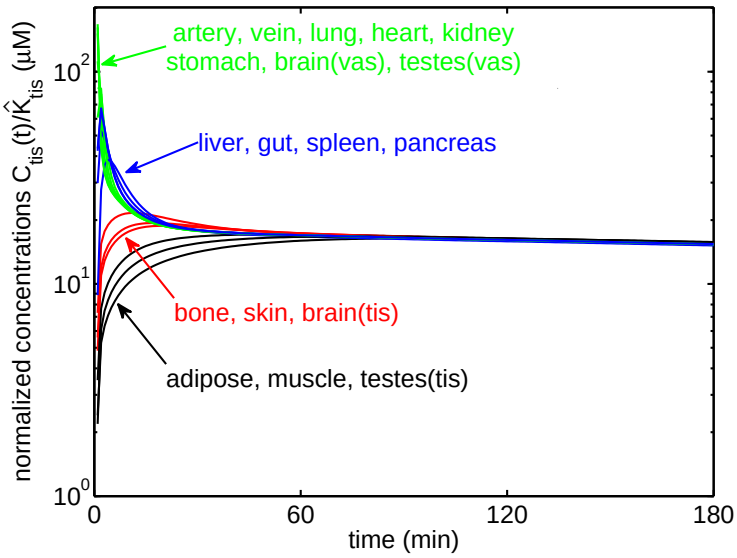

Figure 2.6: Normalized tissue concentrations for the barbiturate C3 based on predictions of an 18-compartment whole-body PBPK model [76]. The normalization was based on the elimination-corrected tissue-to-blood partition coefficient $\widehat{K}_{\text{tis}}$. Vein, artery, and the vascular parts of brain and testes were not scaled. Identical colors indicate the proposed lumping of organs/tissues according to similar concentration-time profiles. Data correspond to a 25 μmol i.v. bolus administration.

following the different steps outlined above. All predicted organ/tissue concentrations were in excellent agreement with the predictions of the detailed 13-compartment PBPK model.

Lumping of a 18-compartment whole-body PBPK model of perfusion and permeability rate-limited organs for barbiturates in the rat

A detailed whole-body PBPK model with some organs showing permeability rate-limited distribution while the remaining organs/tissues exhibit perfusion rate-limited kinetics has been developed by [29, 76] to describe the disposition of barbiturates in the rat. We used this model to illustrate the lumping approach in case of permeability rate-limited kinetics. The PBPK model comprised 18 organs, tissues and vascular compartments and is depicted schematically in Figure 2.5. For all organs/tissues but brain and testes, a perfusion rate-limited, i.e, well-stirred, tissue model was assumed, whereas for brain and testes, tissue distribution was assumed to be permeability rate-limited. In addition to the liver metabolism, drug clearance of the unbound drug in plasma by the kidneys was taken into account. The required species- as well as drug-specific data were taken from [76]. For the tissue-to-unbound plasma partition coefficients, we used the optimized values reported in [76]. Simulation results for the barbiturate C3 following a 25 μmol i.v. bolus administration are shown in Figure 2.7 (green solid line).

Figure 2.6 shows the normalized organ and tissue concentrations for all 18 compartments, where both, the vascular (vas) and the tissue (tis) concentration-time profiles for the two permeability rate-limited tissues testes and brain are included (as for plasma, we set the partition coefficients for the vascular parts of brain and testes to 1). Four sets of compartments to be lumped together can be identified: {gut, spleen, pancreas, liver}, {skin, bone, brain(tis)}, {muscle, adipose, testes(tis)}, in addition to the central compartment {lung, artery, vein, kidneys, heart, stomach, brain(vas), testes(vas)}.

The lumping approach naturally extends to permeability rate-limited organ models, as described in detail in Appendix B.3. For lumping of a permeability rate-limited organ/tissue, we derive the following

Permeability rate-limited criteria:

$$\frac{Q_{\text{tis}}}{\text{PS}_{\text{tis}} + Q_{\text{tis}}} > \frac{\text{PS}_{\text{tis}}}{\text{PS}_{\text{tis}} + Q_{\text{tis}}}. \tag{2.44}$$

This criteria ensures that permeability rather than perfusion is the rate-limiting step of tissue distribution. If this condition would be violated, the model could be considered as either mixed perfusion and permeability rate-limited, or as solely perfusion rate-limited (depending on the actual values). In the former case, the interplay between vascular and tissue part is expected to be critical, such that the compartment should be left un-lumped. In the latter case, the organ model could be changed to the simpler perfusion rate-limited model. For the barbiturate C3, the permeability rate-limited criteria was satisfied for both, brain and testes.

Under the permeability rate-limited criteria, the vascular part of a permeability rate-limited organ can be lumped together with the venous blood, while the tissue parts are lumped based on (see Appendix eq. (B.34))

$$V_{\text{tis}} \frac{\text{d}}{\text{dt}} C_{\text{tis}} = \frac{\text{PS}_{\text{tis}} \cdot Q_{\text{tis}}}{\text{PS}_{\text{tis}} + Q_{\text{tis}}} \cdot \left(C_{\text{blood}} - \frac{C_{\text{tis}}}{K_{\text{tis}}} \right). \tag{2.45}$$

Hence, when lumping the tissue part of a permeability-limited tissue model, the term

$$\frac{\text{PS}_{\text{tis}} \cdot Q_{\text{tis}}}{\text{PS}_{\text{tis}} + Q_{\text{tis}}} \tag{2.46}$$

takes the role of the tissue blood flow Q_{tis} of the perfusion rate-limited models (cmp. eq. (2.32)).

Predictions of the lumped 4-compartment model are shown in Figure 2.7 (dashed black line) for different organs and tissues. For almost all of the organs/tissues, the predictions were in excellent agreement with the predictions based on the detailed 18-compartment model. For brain and adipose, the initial concentrations were slightly overestimated. This could be improved by considering adipose as a separate compartment in the lumped model, which would then comprise 5 compartments.

The detailed whole-body PBPK model for barbiturates was used by Nestorov *et al.* [29] to demonstrate their lumping approach. As an pre-processing step, however, the permeability rate-limited tissue distribution model for brain and testes had to be transformed into a perfusion-rate limited model [29]. This reduced the number of compartments to 16, eliminating the two vascular spaces of brain and testes. The simulation results of the artificially transformed PBPK model are shown in Figure 2.7 ('vein', dot-dashed red line, 'Q-limited'). The differences of the predictions between the artificially transformed 16-compartment PBPK model and the original 18-compartment PBPK model are much larger than the differences between the predictions of the lumped 4-compartment model and the original PBPK model.

2.2.2 Relation of Classical and Mechanistically Lumped Models

The comparison of mechanistically lumped models with classical low-dimensional compartment models allows us to derive a mechanistic interpretation of the classical models. In the following, this is exemplified for one- and two-compartment models. We set $r_{\text{admin}} = r_{\text{iv,po}(\text{F}_{\text{bio}})}$.

The mechanistic 1-compartment model was obtained by applying the lumping procedure to lump all compartments of the PBPK into a single lumped compartment. The rate of change of the concentration in the central compartment, C_{cen}, is given by

$$V_{\text{cen}} \frac{\text{d}}{\text{dt}} C_{\text{cen}} = -\text{CL}_{\text{blood}} \frac{C_{\text{cen}}}{K_{\text{cen}}} + r_{\text{admin}}, \tag{2.47}$$

where V_{cen} denotes the total volume of all organs/tissues (defined as in eq. (2.29)), and K_{cen} denotes the tissue-to-blood partition coefficient for the central compartment (defined as in eq. (2.31))). The classical 1-compartment model was specified in terms of the venous blood

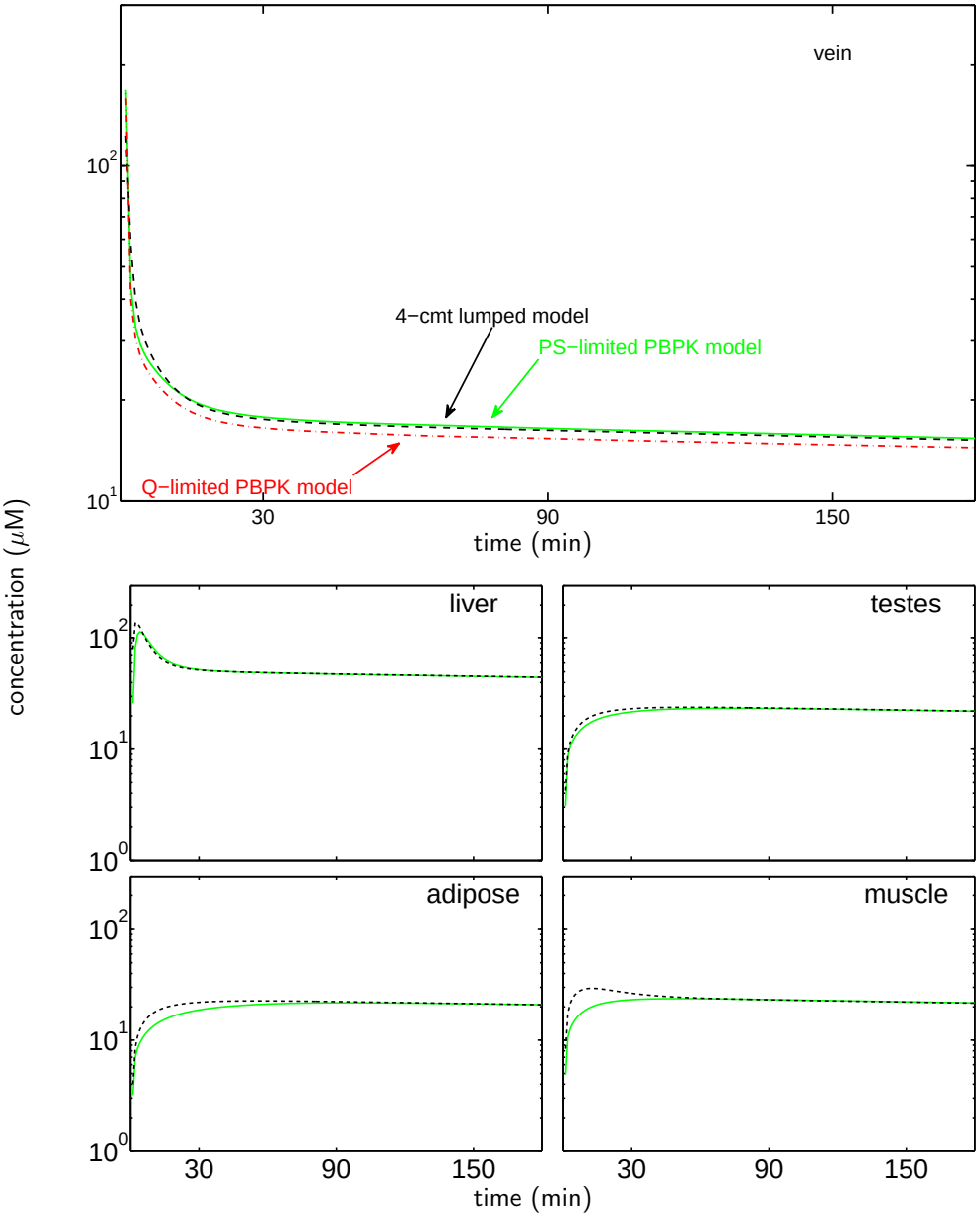

Figure 2.7: Comparison of predictions of an 18-compartment whole-body PBPK model including permeability rate-limited compartments for brain and testes (green solid line, 'PS-limited') and our lumped 4-compartment model (black dashed line, '4-cmt lumped') following a 25 μmol i.v. bolus dose of the barbiturate C3 [76] in the rat for representative organs/tissues. The permeability rate-limited PBPK model and the lumped 4-compartment model show very good agreement for almost all compartments (see liver and testes for two out of 14). For adipose and muscle, the initial concentrations are slightly overestimated. For venous blood, we additionally show predictions for an artificially transformed whole-body PBPK model where the compartments brain and tested were converted to the perfusion rate-limited model (red dot-dashed line, 'Q-limited'). This model was the starting point of existing lumping methods, since they were not able to lump permeability rate-limited models.

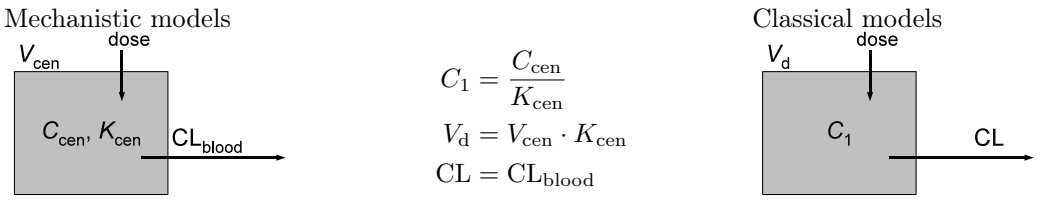

Mechanistic vs. classical 1-compartment model. The corresponding ODEs are given in eqs. (2.47) and (2.3). V_{cen} is identical to the total body volume.

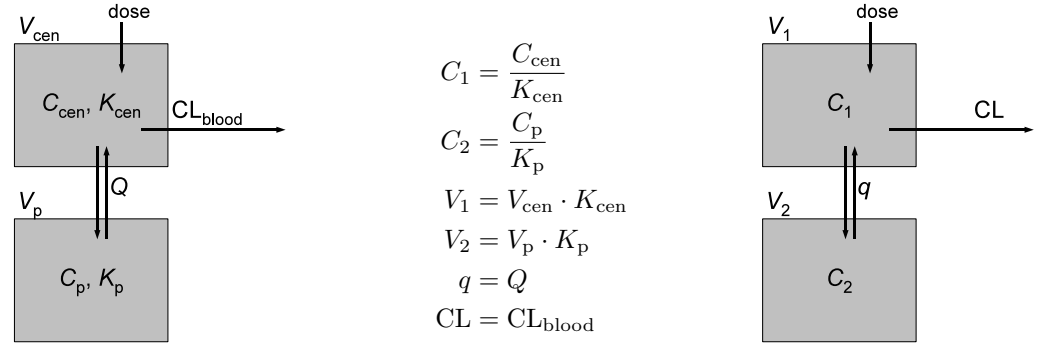

Mechanistic vs. classical 2-compartment model. The corresponding ODEs are given in eqs. (2.48)-(2.49) and eqs. (2.6)-(2.7). The sum of V_{cen} and V_p is identical to the total body volume.

Figure 2.8: Relationship between mechanistic (left) and classical (right) 1- and 2-compartment models. The equations in the middle describe the relationship between the model parameters. The central compartment is by definition the lumped compartment containing the venous blood. Here, we assume that C_1 refers to the blood concentration. If C_1 is the plasma concentration, it can be related to the central concentration by $C_1 = C_{plasma} = C_{cen}/K_{cen}/\text{B:P}$ using the blood-to-plasma ratio, B:P, and the above equations for V_d, V_1, V_2, q, and CL have to be multiplied with B:P.

concentration, C_1, eq. (2.3)

$$V_d \frac{d}{dt} C_1 = -CL \cdot C_1 + r_{admin},$$

where V_d denotes the volume of distribution and CL the total body clearance. Figure 2.8(top) illustrates the mechanistic as well as classical 1-compartment model, and shows the relationship between the model parameters (middle column).

The mechanistic 2-compartment model was derived under the assumption that the liver (as the only eliminating organ) is part of the central compartment (alternative assignments are possible). The rate of change of the concentrations in the central and peripheral compartments, C_{cen} and C_{per}, with volumes V_{cen} and V_{per} and partition coefficients K_{cen} and K_{per}, respectively, were given by

$$V_{cen} \frac{d}{dt} C_{cen} = Q \left(\frac{C_{per}}{K_{per}} - \frac{C_{cen}}{K_{cen}} \right) - CL_{blood} \frac{C_{cen}}{K_{cen}} + r_{admin} \tag{2.48}$$

$$V_{per} \frac{d}{dt} C_{per} = Q \left(\frac{C_{cen}}{K_{cen}} - \frac{C_{per}}{K_{per}} \right) \tag{2.49}$$

Analogously, the classical 2-compartment model was specified in terms of the venous blood and peripheral concentrations, C_1 and C_2, eqs. (2.6) and (2.7)

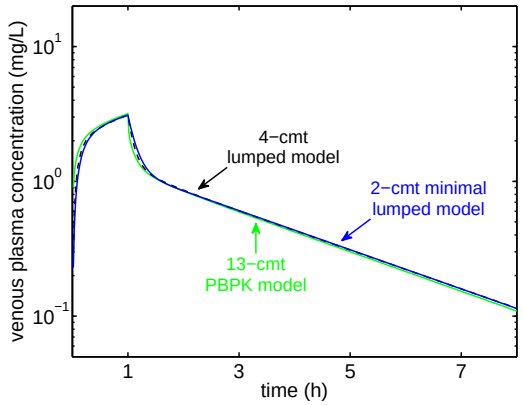

Figure 2.9: Comparison of the 13-compartment whole-body PBPK model for Lidocaine to a mechanistically lumped 4-compartment model and a minimal lumped 2-compartment model for venous blood. All model predictions show excellent agreement.

$$V_1 \frac{\mathrm{d}}{\mathrm{dt}} C_1 = q \cdot C_2 - q \cdot C_1 - \mathrm{CL} \cdot C_1 + r_{\mathrm{admin}}$$
$$V_2 \frac{\mathrm{d}}{\mathrm{dt}} C_2 = q \cdot C_1 - q \cdot C_2,$$

where V_1, V_2 denote the volumes of the central and peripheral compartment, respectively, q denotes the inter-compartmental transfer flow, and CL the hepatic blood clearance. Figure 2.8(bottom) illustrates the mechanistic and classical 2-compartment models and the relationship between the model parameters.

2.2.3 Minimal Lumped Models

The aim of the mechanistic lumping approach was to predict the concentration-time profiles of *all* organs and tissues from the lumped model as accurately as from the PBPK model. If only plasma or blood data are available, as it is typically the case in clinical trials, the question arises whether it is possible to derive lumped compartment models that allow to predict the venous blood concentration with as few compartments as possible. These models are termed 'minimal lumped models'. Again, Lidocaine serves as model compound to demonstrate minimal lumping.

The minimal lumped model was determined on the basis of the mechanistically lumped model by further lumping together additional compartments. A tentative minimal lumped model comprising a {adipose, muscle, skeleton} compartment in addition to the central compartment served as a starting point. Moving additional organs/tissues into the central compartment yielded the final minimal lumped model. Predictions were checked against the detailed PBPK model for the venous compartment.

Figure 2.9 shows the predicted blood concentrations of the mechanistically lumped 4-compartment model and a minimal lumped 2-compartment model in comparison to the prediction of the whole-body PBPK model. The minimal lumped model comprised a lumped compartment containing {adipose, muscle, skeleton} in addition to the central compartment. The parameter values were $V_{\mathrm{cen}} = 14.16$ L, $V_{\mathrm{per}} = 52.84$ L, $Q = 1.755$ L/min and $\mathrm{CL}_{\mathrm{blood}} = 1.095$ L/min. As shown in Figure 2.9, the detailed PBPK model, the mechanistically lumped 4-compartment model, and the minimal lumped 2-compartment model predicted the venous blood concentration with almost identical accuracy.

2.2.4 Influence of the Route of Drug Administration on the Lumped Models

Frequently used routes of drug administration include i.v bolus, i.v. infusion and per oral administration. In the sequel, we analyze the impact of the route of administration on the mechanistically lumped and the minimal lumped model.

Per oral administration

The detailed whole-body PBPK model was used to predict a single p.o. administration of 400 mg Lidocaine. Due to the absence of a human value for the first order absorption rate constant, we employed the canine value $k_{\mathrm{a}} = 0.018$ min^{-1} [82] and we set $F_{\mathrm{F.G}} = 1$. After oral administration of Lidocaine in human, maximum plasma concentrations have been observed between 30 and 45 min [83], which is in accordance with the chosen absorption rate constant.

Figure 2.10 (left) shows the normalized concentrations $C_{\mathrm{tis}}(t)/\widehat{K}_{\mathrm{tis}}$. The situation is almost identical to the situation of an i.v. infusion (cmp. Figure 2.4(left)), except that the normalized liver concentration shows a different 'shape'. This different shape is the result of the influx of drug through the portal vein. As a consequence, the number of compartments of the mechanistically lumped model increases by one: {skeleton}, {adipose, muscle}, {skin}, {liver} and {rest = all remaining tissues and organs}.

An increase in the number of compartments of the mechanistically lumped model does not necessarily result in an increased number of compartments of the minimal lumped model. Figure 2.10 (right) shows the venous plasma concentration as predicted by the 13-compartment whole-body PBPK model, the mechanistically lumped 5-compartment model, and a minimal lumped 2-compartment model comprising a {muscle, adipose, skeleton} compartment in addition to the central compartment. The predictions were in excellent agreement. Hence, although the p.o. administration increases the number of compartments of the mechanistically lumped model, it does not increase the number of compartments of the minimal lumped model.

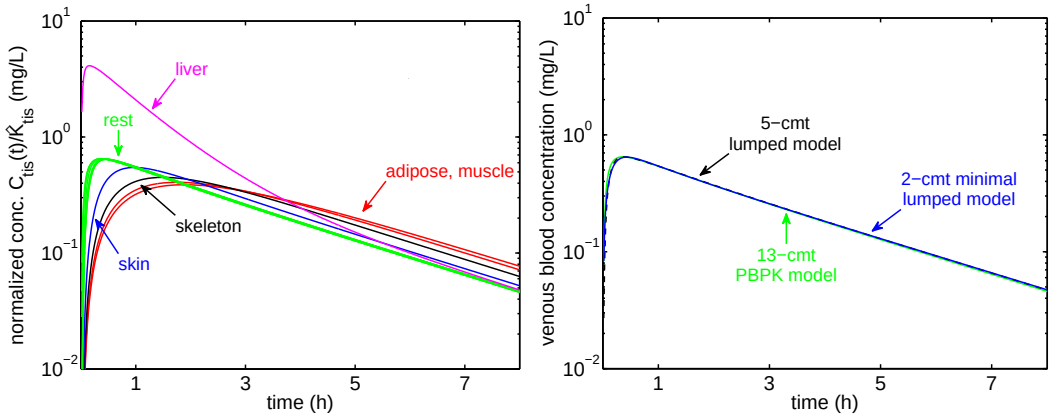

Figure 2.10: Normalized tissue concentrations for Lidocaine based on predictions of the detailed 13-compartment PBPK model following a p.o. administration. Left: Normalization of tissue concentrations $C_{\mathrm{tis}}(t)$ based on the elimination-corrected tissue-to-blood partition coefficient $\widehat{K}_{\mathrm{tis}}$. Vein and artery were not scaled. Right: Comparison of the 13-compartment whole-body PBPK model for Lidocaine to a mechanistically lumped 5-compartment model and a minimal lumped 2-compartment model for venous blood. Data correspond to a single dose of 400 mg Lidocaine and show excellent agreement.

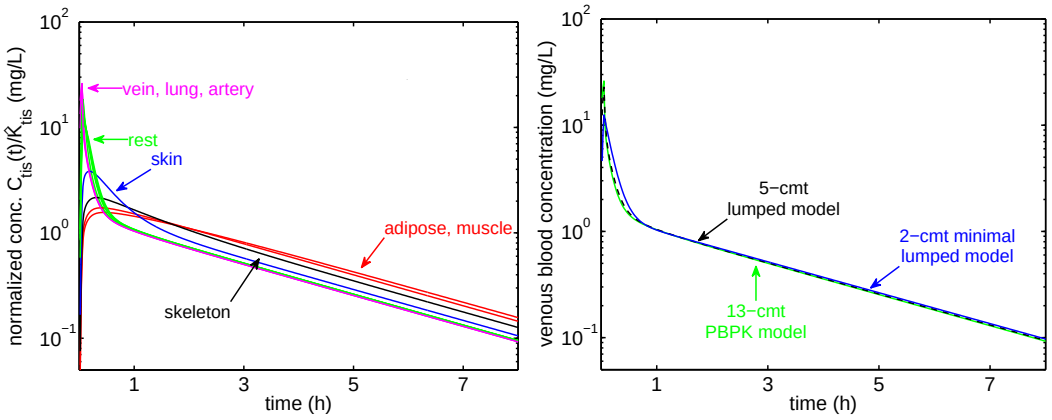

Figure 2.11: Normalized tissue concentrations for Lidocaine based on predictions of the detailed 13-compartment PBPK model following an i.v. bolus administration. Left: Normalization of tissue concentrations $C_{\text{tis}}(t)$ based on the elimination-corrected tissue-to-blood partition coefficient $\widehat{K}_{\text{tis}}$. Vein and artery were not scaled. Right: Comparison of the 13-compartment whole-body PBPK model for Lidocaine to a mechanistically lumped 5-compartment model and a minimal lumped 2-compartment mode for venous blood. Data correspond to a single dose of 400 mg Lidocaine and show good agreement.

Intravenous bolus administration

Figure 2.11 (left) shows the normalized concentrations $C_{\text{tis}}(t)/\hat{K}_{\text{tis}}$ following an i.v. bolus administration of 400 mg Lidocaine. The number of distinct concentration-time profiles in comparison to the i.v. infusion (cmp. Figure 2.4) is again increased by one to account for the very first distributional phase: {skeleton}, {adipose, muscle}, {skin}, {vein, lung, artery} and {rest = all remaining tissues and organs}.

Figure 2.11 (right) shows the venous blood concentration as predicted by the 13-compartment whole-body PBPK model, the mechanistically lumped 5-compartment model, and a minimal lumped 2-compartment model comprising a {muscle, adipose, skeleton} compartment in addition to the central compartment. All predictions are in good agreement, and the number of compartments of the minimal lumped model was the same as for an i.v. infusion administration.

However, if concentration-time profiles at early time points have to be predicted with high accuracy, the number of compartments in the minimal lumped model would have to be increased to account for the very first distributional phase. A third compartment in the minimal lumped model would comprise {vein, lung, artery} in addition to the peripheral compartments {adipose, skeleton, muscle} and {rest = all remaining tissues and organs}.

2.2.5 Minimal Lumped and Classical Pharmacokinetic Model for Lidocaine Disposition after an I.v. Bolus Administration

The following example of Lidocaine disposition following a 3 min i.v. bolus administration illustrates the above conclusion regarding the number of compartments of the minimal lumped model: In most studies, the pharmacokinetics of Lidocaine is described by a 2-compartment model with linear elimination from the central compartment [8, 78, 80, 84] (as predicted by the minimal lumping for an i.v. infusion and p.o. administration). In [81], Lidocaine plasma data of a 3 min i.v. bolus administration of 3 mg/kg have been collected following a very dense sampling scheme for early time points; and the authors fitted the plasma time course by a tri-exponential equation. Here, a minimal lumped two-compartment model would compromise the predictions for the detailed measurements of the initial distribution phase; and the number of compartments in the minimal lumped model has to be increased by one.

Figure 2.12 shows the experimental data reported in [81] and the plasma concentration-

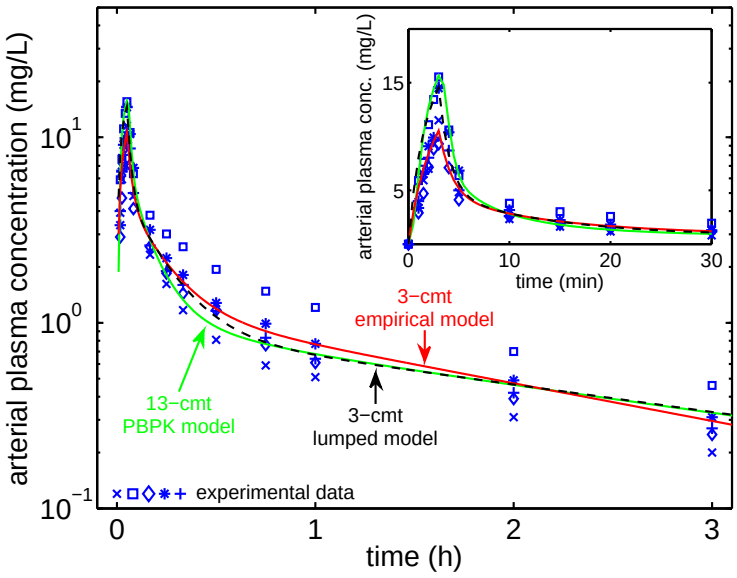

Figure 2.12: Predictions of individual experimental data for five individuals following a 3 min i.v. bolus administration of 3 mg/kg Lidocaine based on the 13-compartment whole-body PBPK model, the 3-compartment minimal lumped model, and the 3-compartment empirically fitted model. The parameter values of the 3-compartment models are summarized in Table 2.3. The experimental data was taken from [81]. The empirical model describes the elimination phase slightly better than the PBPK and minimal lumped model, but it underestimates the $C_{\max}$ values (see inset).

time profiles as predicted by the 13-compartment PBPK model and a minimal lumped 3-compartment model comprising the central {vein, lung, artery} compartment in addition to the peripheral compartments {adipose, skeleton, muscle} and {rest = all remaining tissues and organs}. The detailed as well as the minimal lumped model excellently predict the experimental data. The parameters of the minimal lumped 3-compartment model are listed in Table 2.3.

We further analyzed whether the minimal lumped 3-compartment model could serve as a structural model to fit the experimental plasma data. The estimated parameters V_1, V_2, V_3, q_{12}, q_{13} and CL of the classical 3-compartment model are given in Table 2.3 (right), and the predicted concentration-time profile for venous plasma is shown in Figure 2.12 ('3-cmt empirical model'). We did not analyze the individual experimental data based on a population pharmacokinetic approach, since this would be beyond the scope of this thesis, but estimated mean parameters based on minimizing the sum of squares (SS) of the error of the mean model predictions to the individual data:

$$SS = \sum_{ij} \left(\frac{C_{\text{pred},ij} - C_{\text{exp},ij}}{w_{ij}} \right)^2, \tag{2.50}$$

where $C_{\text{pred},ij}$ and $C_{\text{exp},ij}$ are the predicted and experimental data at time point j for individual i, respectively. The weighting factor w_{ij} is given by

$$w_{1j} = \ldots w_{5j} = (C_{\text{exp,mean}j})^2 \tag{2.51}$$

for the five individuals of the study. For each time point j, $C_{\text{exp,mean}j}$ denotes the mean of the experimental measurements.

As can be inferred from Figure 2.12, both, the minimal lumped as well as the empirically fitted 3-compartment model, describe the experimental data very well. Based on the relations given in Figure 2.8, we also determined the parameter values of V_1, V_2, V_3, q_{12}, q_{13} and

CL from the minimal lumped model, see Table 2.3 (middle) for comparison. Interestingly, while the empirically fitted and mechanistically derived V_2, q_{12}, and CL are close to each other, the empirically fitted V_1, V_3, and q_{13} are approximately 1.6, 0.8 and 1.3 times the mechanistically derived V_1, V_3, and q_{13}, respectively.

Table 2.3: Comparison of parameters of the fitted classical 3-compartment model (right) and the minimal lumped model (left and middle). Parameters of the minimal lumped model (left) were transformed into corresponding parameters of the classical compartment model as specified in the table. Volumes are given in [L] and volume flows are given in [L/min].

minimal lumped model parameters				empirical parameter estimates	
V_{cen}	5.8	$V_1 = V_{\text{cen}} \cdot K_{\text{cen}} \cdot \text{B:P}$	6.36	V_1	10.51
V_{p1}	8.36	$V_2 = V_{\text{p1}} \cdot K_{\text{p1}} \cdot \text{B:P}$	16.81	V_2	18.62
V_{p2}	52.84	$V_3 = V_{\text{p2}} \cdot K_{\text{p2}} \cdot \text{B:P}$	92.19	V_3	72.77
Q_{p1}	4.26	$q_{12} = Q_{\text{p1}} \cdot \text{B:P}$	3.58	q_{12}	4.75
Q_{p2}	1.75	$q_{13} = Q_{\text{p2}} \cdot \text{B:P}$	1.47	q_{12}	1.57
CL_{blood}	1.1	$\text{CL} = \text{CL}_{\text{blood}} \cdot \text{B:P}$	0.92	CL	1.04
K_{cen}	1.3				
K_{p1}	2.4				
K_{p2}	2.1				

2.2.6 Characteristic Features of Lumped Models for Moderate-to-Strong Bases, Weak Bases, and Acids

A major determinant of drug disposition is tissue distribution. The approach by Rodgers *et al.* to *a priori* predict tissue-to-unbound plasma partition coefficients [59–62] was used to parameterize the 13-compartment whole-body PBPK model for a number of different drugs. These *in silico* approaches regard the tissue as comprising an interstitial and an intra-cellular space. The unbound drug is possibly ionized in the interstitial and intra-cellular space and the neutral species can cross membranes by passive diffusion. In the intra-cellular space, the neutral species may distribute into neutral lipids and neutral phospholipids. In addition, a drug may bind to further tissue constituents. For moderate-to-strong bases, it is assumed that binding to acidic phospholipids is a major determinant of intra-cellular distribution. For weak bases, neutrals and acids, binding in the interstitial space is an important determinant. It is assumed that weak bases and acids bind to albumin, while neutrals are assumed to bind to lipoproteins [59, 61, 85].

A diverse set of 25 drugs was used to investigate whether mechanistically lumped models exhibit characteristic features based on the alkalinity/acidity of the drug. See Table 2.2 for the drug-specific parameters. The compounds were chosen from [63, 64, 66]. The analysis was restricted to those compounds for which all parameters for the PBPK modeling were available in the literature. The availability of the blood-to-plasma ratio, B:P, was the limiting factor in choosing the drugs.

For each drug, the concentration-time profiles were predicted based on the generic 13-compartment PBPK model shown in Figure 2.2 for a 60 min i.v. infusion. Administration by infusion was chosen, since it did not require any additional parameter values as, e.g., the absorption rate constant for oral absorption. Based on the algorithm outlined in Appendix B.4, the number of compartments for a mechanistically lumped compartment model were determined. The predicted number of compartments for the different compound classes, i.e., moderate-to-strong bases, weak bases and acids are shown in Figure 2.13(left).

For weak and moderate-to-strong bases, a lumped 3- to 5-compartment model was sufficient to predict the drug pharmacokinetics in all 13 organs/tissues. For acids, the lumped

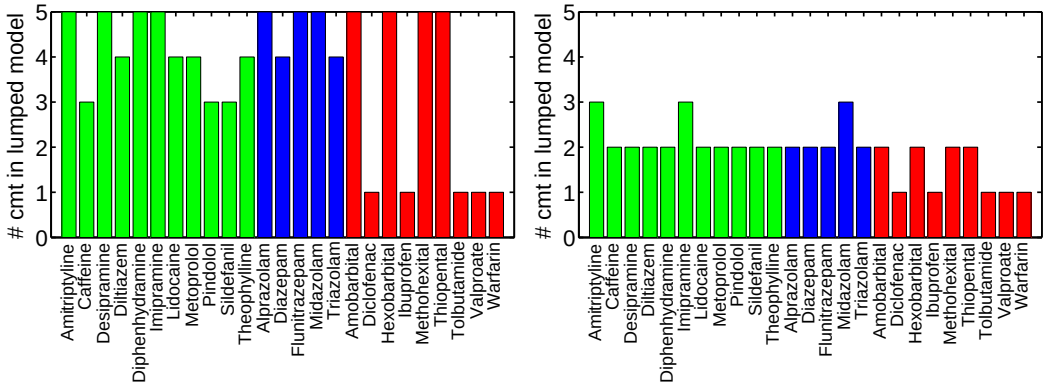

Figure 2.13: Predicted number of compartments for the mechanistically lumped model (left) and the minimal lumped model (right) based on concentration-time profiles generated by the 13-compartment whole-body PBPK models. The colors indicate the categorization of drugs as follows: moderate-to-strong bases (green, left), weak bases (blue, middle) and acids (red, right).

model comprised either a single compartment or five compartments. If a lumped model comprised more than a single compartment, then adipose, skeleton, muscle and skin were typically not part of the central compartment (see Figure 2.14). From these four tissues/organs, skin usually showed closest similarity to the central compartment.

In Table 2.4, physiological and anatomical data of adipose, skeleton, muscle and skin are listed for an average human. Their important role in tissue distribution is due to their distinct characteristics. The four organs make the largest fraction of the total body volume, with muscle being by far the largest tissue. At the same time, their blood flows are amongst the lowest. Regarding important tissue constituents influencing tissue distribution, the four tissues/organs typically show distinct characteristics at the extremes: adipose has lowest tissue water, high neutral lipids and low phospholipids; skeleton has lowest phospholipids, muscle and skin have high tissue water content. These characteristics make them key tissues/organs in drug distribution.

For a number of acidic drugs, the mechanistically lumped compartment comprised only a single compartment, while for other acids the number of compartments was 5. The fraction unbound in plasma, fu^p, was the discriminating parameter: For acids with a low fu^p (in our examples $fu^p \leq 0.1$), a mechanistically 1-compartment model was sufficient, while for acids with a moderate-to-high fu^p (in our examples $fu^p \geq 0.18$), more than one compartment were predicted.

Next, minimal lumped models for the 25 compounds of Table 2.2 were derived, see Figure 2.13(right). Also here, the distinct role of adipose, muscle and skeleton was present.

Table 2.4: Physiological and anatomical data for adipose, muscle, skeleton, skin and remaining tissues [56, 63]. Volume: fraction of total body weight; blood flow: fraction of cardiac output; tissue water, neutral lipids, phospholipds: fraction of total tissue volume. The column 'remaining organs' lists the minimum and maximum values amongst all remaining organs considered in the whole-body PBPK model depicted in Figure 2.2.

	adipose	skeleton	muscle	skin	remaining organs
Volume	0.22	0.11	0.40	0.045	0.002-0.025
Blood flows	0.05	0.05	0.17	0.05	0.03-1.00
Tissue water	0.15	0.44	0.76	0.62	0.72-0.81
Neutral lipids	0.79	0.074	0.024	0.028	0.003-0.051
Phospholipids	0.002	0.001	0.007	0.011	0.009-0.057

We used the residual error measure $\| \cdot \|_{\text{PBPK}}$ defined in eq. (A.1) to quantify the difference between the venous blood concentration as predicted by the PBPK model and as predicted by the minimal lumped model, and regarded the minimal lumped model as adequate, if the residual error was below $\epsilon = 0.09$ (a common value for all drugs allowed for unbiased comparison).

For Amitriptyline, Imipramine and Midazolam, the minimal lumped model comprised 3 compartments. For all other compounds (except for the ones where the lumped model comprised only a single compartment), a minimal 2-compartment model comprising an {adipose, muscle, skeleton} compartment in addition to the central compartment resulted in excellent predictions for venous plasma when compared to those predicted by the whole-body PBPK model.

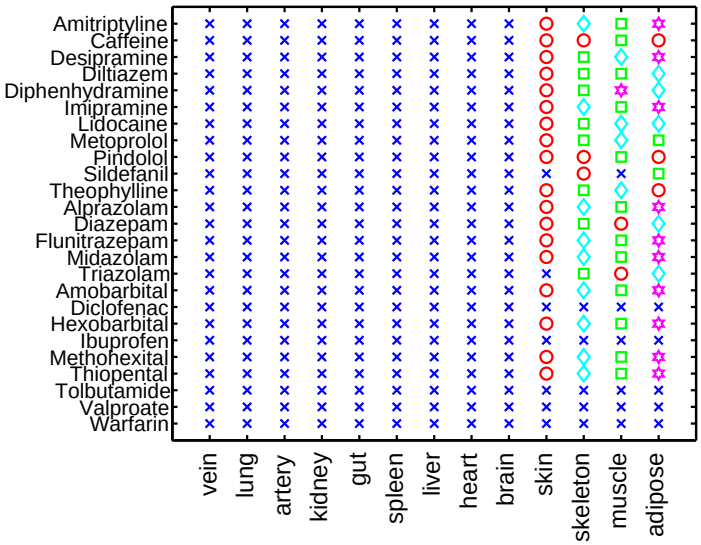

Figure 2.14: Predicted assignment of organs, tissues and other spaces of the whole-body PBPK model to the lumped compartments of the mechanistically lumped model for the same 25 compounds as in Figure 2.13. The central compartment is represented by x, potential additional peripheral compartments are represented by *o*, square, diamond etc. The number of different symbols for a given compound corresponds to the number of compartments in the mechanistically lumped model.

2.2.7 Lumping and Tissue Distribution Half-Life

Based on the well-stirred tissue model, a distributional half-life may be associated with each tissue: Rearranging eq. (2.8) yields

$$\frac{\mathrm{d}}{\mathrm{dt}} C_{\text{tis}} = \frac{Q_{\text{tis}} C_{\text{in,tis}}}{V_{\text{tis}}} - \frac{Q_{\text{tis}}}{V_{\text{tis}} \widehat{K}_{\text{tis}}} \cdot C_{\text{tis}}. \tag{2.52}$$

The pre-factor of the second summand can be interpreted as a distribution rate constant

$$k_{\text{tis}} = \frac{Q_{\text{tis}}}{V_{\text{tis}} \widehat{K}_{\text{tis}}} \tag{2.53}$$

associated with the tissue, where $V_{\text{tis}} \widehat{K}_{\text{tis}}$ can be understood as the volume of distribution associated with the tissue. Based on k_{tis}, the kinetics of tissue distribution are characterized by the

$$\text{Tissue distribution half-life} \quad = \quad \frac{\ln(2)}{k_{\text{tis}}}. \tag{2.54}$$

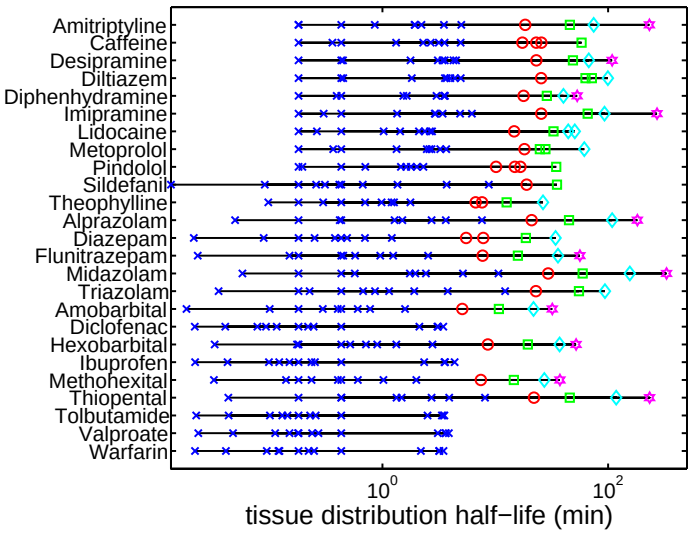

Figure 2.15: Tissue distribution half-life for all organs/tissues of the 13-compartment PBPK model for the same 25 compounds of Figure 2.13. For each compound, the 13 markers represent the 13 organs and tissues of the generic PBPK model. Identical symbols represent organs and tissues that were lumped together in the mechanistically lumped model. As in Figure 2.14, the central compartment is represented by x, potential additional peripheral compartments are represented by *o*, square, diamond etc. Artery (at 0.26 min) and vein (at 0.62 min) are clearly visible for all compounds, since these are the only two spaces whose half life does only depend on volume and blood flow, but not on a drug-specific partition coefficient.

This half-life corresponds to the situation, in which the inflowing drug concentration, $C_{\text{in,tis}}$, is assumed to be constant. Tissue distribution is the slower, the larger the product $V_{\text{tis}}\widehat{K}_{\text{tis}}$ or the smaller the blood flow Q_{tis} perfusing the tissue or organ.

In Figure 2.15, the tissue distribution half-lives for the compounds listed in Table 2.2 are shown. Organs/tissues that were clustered together by the lumping method are marked with the same marker (cross, circle, square, etc). Noticeably, the tissue distribution half-life for different lumped compartments do not overlap. A decision on how to lump organs based on their tissue distribution half-life is possible—and the lumping criteria of existing lumping methods [29, 31]—but much harder.

2.2.8 Discussion and Conclusions

In this section, we presented a novel lumping method for the reduction of whole-body PBPK models. We used the proposed method to translate knowledge present in a 13- and 18-compartment PBPK model into mechanistically lumped 4-compartment and minimal lumped 2-compartment models. The proposed method has several advantageous features: (i) there is no restriction on how organs and tissues can be lumped together; (ii) it is possible to lump perfusion rate-limited as well as permeability rate-limited compartment models; (iii) concentrations in the original compartments can be predicted based on the concentrations in the lumped compartments; and (iv) the lumping conditions have a physiological interpretation and are easily visualized. These are significant advancements over existing lumping methods [29–32].

Nestorov *et al.* [29] were the first to derive standard lumping principles for PBPK models. Their lumping approach is based on four conditions: (i) only organs can be lumped together that are either in parallel or in series (referring to the tissue topology in Figure 2.2); (ii) permeability rate-limited models have to be approximated by perfusion rate-limited models as a pre-processing step; (iii) vein, lung and artery are either lumped together or left sepa-

rate; and (iv) lumping of organs/tissues is based on similar or small time constants. For non-eliminating tissues, this time constant is defined as

$$T_{\text{tis}} = \frac{V_{\text{tis}} K_{\text{tis}}}{Q_{\text{tis}}}, \tag{2.55}$$

while for eliminating organs/tissues, it is

$$T_{\text{tis}} = \frac{V_{\text{tis}} K_{\text{tis}}}{Q_{\text{tis}} + \text{fu}_{\text{blood}} \text{CL}_{\text{int}}}, \tag{2.56}$$

where V_{tis}, Q_{tis} and K_{tis} refer to the tissue volume, the tissue blood flow and the tissue-to-blood partition coefficient, respectively; and fu_{blood} and CL_{int} denote the fraction unbound in blood and the intrinsic clearance, respectively. Thus, given the topology in Figure 2.2, the smallest lumped model consistent with the above conditions (i)-(iii) has at least four lumped compartments: {vein, lung, artery}, {spleen, gut}, {liver}, {all other compartments}. While their equations for the lumped volume, blood flow and partition coefficient are identical to our eqs. (2.29), (2.32) and (2.31), it is the lumping criterion (and thereon build derivations) that distinguishes our approach from the existing approaches. The herein proposed lumping criterion, e.g., allows a justified application of lumping, where existing lumping criteria fail. As a results, we can easily justify the reduction of a 13-compartment whole-body PBPK model to a single lumped compartment.

As in our approach, Nestorov *et al.* [29] lump together tissues with similar kinetics. Their measure of similarity is based on the time constant, T_{tis} (eqs. (2.55)-(2.56)). Some rule of thumb on how similar the time constants have to be is given in [29, p.32-33]. The time constant is related to the tissue distribution half-life by (cmp. eq. (2.54))

$$\text{Tissue distribution half-life} \quad = \quad \ln(2) \cdot T_{\text{tis}}. \tag{2.57}$$

Given a list of time constants (see Figure 2.15 for a variety of compounds), it can be very difficult to decide which compartments to lump. Moreover, the time-constants are independent of any administration details and as such cannot predict different structures of lumped models for different administrations/dosing schemes. In our approach, the lumping condition is based on the transient feature of tissue distribution as well as on the elimination phase after distribution reached quasi-steady state.

The lumping method in [29, 31] does not relate the predictions of the lumped model back to predictions in individual organs/tissues of the original whole-body PBPK model. Instead, for comparison with the predictions of the lumped model, the whole-body PBPK model predictions would have to be lumped. The same applies to a comparison with experimental data. If experimental data were only available for one, but not all of the original organs/tissues that are part of a lumped compartment, such an approach would not be applicable. As a consequence, Brochot *et al.* [30] introduced a constraint lumping approach, where some of the original variables are left unlumped. While this solves the above mentioned problem, it increases the number of compartments of the lumped model. With our proposed lumping approach both aims, a small number of compartments of the lumped model as well as the possibility to predict original organ and tissue concentration-time profiles, can be achieved at the same time.

A further reduction of the mechanistically lumped model is possible if we are only interested in predictions of the venous plasma or blood concentration (as part of the central compartment). For our reference compound Lidocaine, we were able to further reduce the lumped 4-compartment model to a minimal lumped 2-compartment model. A further reduction to one compartment did compromise the predictions for the central compartment, as one would expect due to the bi-exponential characteristics of the concentration-time profiles.

The structure and number of compartments of our minimal lumped 2-compartment model is in accordance with the majority of published pharmacokinetic models describ-

ing the disposition of Lidocaine, e.g., [8, 78, 80, 84]. However, analyzing the experimental Lidocaine plasma data published in [81] revealed that an i.v. bolus administration together with a very dense sampling scheme at early time points may require to increase the number of compartments in the low-dimensional model by one to account for the very initial distributional phase. In [81], the Lidocaine plasma data were fitted by a tri-exponential equation, indicating the adequateness of a 3-compartment model to describe the data, which is in accordance with our findings for this case.

Analyzing minimal lumped models for a variety of compounds revealed that a minimal lumped 2-compartment model comprising an {adipose, skeleton, muscle} compartment in addition to the central compartment containing all remaining tissues was almost always as good in predicting the *venous blood* concentration as the detailed PBPK model. This highlights and confirms the importance of adipose, skeleton and muscle tissue for drug distribution, which is due to their size and often distinct characteristics compared to the remaining organs/tissues (cmp. also Table 2.4). A more thorough analysis about how to systematically derive a minimal lumped model from a mechanistically lumped model subject of current research.

The presented analysis based on 25 compounds is a first step towards a more comprehensive understanding of minimal lumped compartment models. The limiting factor for the number of compounds considered herein was the availability of the blood-to-plasma ratio B:P. From the point of *in silico* modeling and simulation, this parameter is an important datum. While it is nowadays by default measured in the drug discovery phase, it seems rarely be reported in drug databases.

An important part of classical modeling is to specify the structure of the empirical compartment model. This includes specification of the number of compartments, its connections, whether processes are linear or non-linear etc. Another important question is whether elimination takes place in the central or in the peripheral compartment. This might not only impact convergence of the estimation process, but also influence pharmacokinetic characteristics like, e.g., the volume of distribution [86, 87]. Commonly, the 'elimination at the point of observation' assumption is made, while a compartmental model with peripheral elimination might give rise to a larger volume of distribution [87]. We observed that for all compounds analyzed in this study, the liver was part of the central compartment, an observation in favor of the 'elimination at the point of observation' assumption.

A minimal lumped model derived from a whole-body PBPK model evaluated against pre-clinical and early clinical data can be interpreted as extrapolating the current knowledge about the drug pharmacokinetics into the next developmental phase. At the same time, an empirical compartment model, e.g., developed as a structural model in population analysis of clinical trials based on new experimental data, might be interpreted as representing the minimal description of this new information in terms of a pharmacokinetics model. A comparison of both models, therefore, offers the possibility to compare the expectations based on translating previous insights and knowledge with the information content of new clinical data. This is a consistency check of the new data against previous knowledge. In addition, since the parameters of the empirical model have to be estimated based on experimental data, the parameters of our minimal lumped model can be used as initial values in the estimation process, addressing the critical question of how to chose initial conditions in the parameter estimation process.

Our proposed lumping method in its current form applies to the important class of linear PBPK models. Extension to include non-linear behavior seems possible. Saturable metabolism is likely to be includable based on a non-linear extraction ratio. Incorporation of further non-linearities might be more difficult, and results might then become dose dependent. A more thorough analysis of lumping including non-linearities has to be left for the future.

Applying our lumping method to a diversity of drugs allowed us to obtain some general insight on the kinetic diversity and the number of lumped compartments for different classes of compounds. Our analysis is based on recent advances to *a priori* models for predicting tissue-to-unbound plasma partition coefficients [59, 61]. Rather than grouping drugs according to therapeutic indications, we grouped them according to their alkalinity/acidity. We found that for weak and moderate-to-strong bases and for acids with a moderate to high fraction unbound, the mechanistically lumped model typically comprised three to five compartments. For acids with a low fraction unbound, i.e., high plasma protein binding, the lumped model comprised only a single compartment. For acids, the fraction unbound in plasma is used to determine the albumin association constant in the model to *a priori* predict tissue-to-unbound plasma partition coefficients [61]. From this it follows that acids with low fu^p strongly bind to interstitial albumin. This might explain why a 1-compartment model was sufficient to predict the concentration-time profile of the drug in all organs and tissues as accurately as predicted by the 13-compartment whole-body PBPK.

A first comparison to published classical PK models for analyzing clinical data showed a good agreement between the number of compartments used and the number of compartments of our minimal lumped model. For Midazolam and Thiopental, 2- and 3-compartment models have been used [88–91], while we predicted a minimal 3-compartment model for Midazolam and a minimal 2-compartment model for Thiopental. For Valproate, a 1-compartment model is reported by [92, 93], which is in agreement with our predictions (see Figure 2.13). For Tolbutamide, a 2-compartment model was used in [94], while we predict a minimal 1-compartment model. Such a comparison can only be preliminary, since it does not take into account two important facts: the sparsity of the experimental data, and the variability inherent in the patient cohort of clinical trials. The first fact might result in a lower number of compartments in the estimated classical model, while the second fact is likely to result in a larger number of compartments estimated for the classical model.

In summary, the presented lumping method is the first step towards a more comprehensive approach to translate knowledge and insight from pre-clinical and early clinical development—given in form of a whole-body PBPK model—into the development of classical compartment models. So far, we focussed on the static parameter case, i.e., the case of an individual (including the fictive mean individual). In section 2.3 we will consider variability of the type that is present in patient collectives of clinical trials. In this regard, the development of methods to generate *in silico* populations suitable for PBPK modeling [95, 96], and the development of a methodology to consider parametric variability [31] will prove useful. This opens the possibility to extend the presented lumping method to analyze and incorporate covariates and their expected impact into the lumped model.

2.3 *Case Study* Towards Mechanistic Covariate Modeling in Population Pharmacokinetics

The study of pharmacokinetics in populations of interest is referred to as population pharmacokinetics [8, 12, 97, 98]. The goals of population pharmacokinetics include the identification of patient populations that require an adjustment of the dose or dosing regimen in order to achieve the desired effect while minimizing adverse events as well as the estimation of mean pharmacokinetic parameters that characterize the population and sources of variability in the population [8, 12, 97].

Population pharmacokinetic model development includes i) the identification of a structural model that best describes the time series measurements of drug concentration for the individuals of the study population, and ii) the identification of covariates that explain the potentially observed variability in individual concentration-time profiles. The covariates are additional patient characteristics, e.g., age, sex, body weight, creatinine clearance, etc. They can be interpreted as individual scaling factors of the population mean pharmacokinetic data [7, 8, 12, 97, 98]. The successful identification of significant covariates finally allows for the recommendation of dosing adjustments for individuals or subgroups of the population [8, 98].

So far, the selection of significant covariates primarily follows an empirical technique for the inclusion or deletion of covariates from the model based on a statistical criterion [12, 99]. This empirical technique is a complex and time-consuming approach [12] and a method to include mechanistic knowledge into covariate modeling is thought to highly facilitate the identification of significant covariates and additionally provides an approach towards predictive population pharmacokinetics.

We propose to make use of PBPK modeling that allows for the integration of individual patient characteristics together with our lumping method to provide a mechanistic approach to covariate modeling in population pharmacokinetics: From a reference set of physiological parameters, we determine individual parameter values based on a scaling that incorporates relevant anthropometric patient data, e.g., body weight, body height, body surface area, lean body mass, etc. We present a general scaling factor approach to derive individual organ volumes, blood flows, tissue-to-blood partition coefficients, and hepatic clearances. Illustrated for a recent specification of the scaling factors as a function of body height and body weight [96], we predict the diversity of concentration-time profiles due to the variability in the physiological parameters for a virtual population of healthy male adults. Applying our novel lumping approach to the generic PBPK model incorporating the individual scaling factors, we derive a mechanistic low-dimensional compartment model incorporating mechanistic covariates.

2.3.1 Scaling of Physiological Parameters in PBPK Models

The generic PBPK model for small molecule drugs introduced in section 2.1.2 and depicted in Figure 2.2, is parameterized by the tissue volumes, V_{tis}, blood flows, Q_{tis}, tissue-to-blood partition coefficients, K_{tis}, and the hepatic intrinsic clearance, CL_{int} or hepatic blood clearance, CL_{blood}. In the sequel, we present a general scaling approach to derive the PBPK model parameters for an individual' i' based on a reference set of parameter values, 'ref' and some scaling factor. We also present a specification of the scaling factors in terms of anthropometric characteristics, i.e., body height, body weight (or body mass index) as presented in [96].

General scaling approach

For an individual 'i', the tissue volumes, $V_{\text{tis},i}$, are given by

$$V_{\text{tis},i} = \text{SV}_{\text{tis},i} \cdot V_{\text{tis,ref}}, \tag{2.58}$$

where $V_{\text{tis,ref}}$ are the tissue volumes of the reference and $\text{SV}_{\text{tis},i}$ denote the individual tissue volume scaling factors. For the cardiac output, it is

$$Q_{\text{co},i} = \text{SQ}_i \cdot Q_{\text{co,ref}}, \tag{2.59}$$

where $Q_{\text{co,ref}}$ is the cardiac output of the reference and SQ_i denotes the individual cardiac output scaling factor. Individual tissue blood flows, $Q_{\text{tis},i}$, were derived under the assumption that the fractions of blood flow to cardiac output are constant, i.e., $Q_{\text{tis},i}/Q_{\text{co},i} = Q_{\text{tis,ref}}/Q_{\text{co,ref}}$. From eq. (2.59) it follows

$$Q_{\text{tis},i} = \text{SQ}_i \cdot Q_{\text{tis,ref}}. \tag{2.60}$$

For our generic PBPK model introduced in section 2.1.2, we proposed to determine the tissue-to-blood partition coefficients, K_{tis}, based on the method by Rodgers *et al.* [59–62]. Assuming that the physiological parameters relevant for the determination of K_{tis} (fraction of interstitial space, fraction of water, neutral lipids, and neutral phospholipids, protein content in plasma and interstitial space, hematocrit value) are constant amongst individuals, it follows

$$K_{\text{tis},i} = K_{\text{tis,ref}} \tag{2.61}$$

for all organs and tissues (see the Discussion for more details). In the sequel, we therefore omit the index 'i'. The intrinsic hepatic clearance $\text{CL}_{\text{int},i}$ is assumed to scale with the number of hepatic cells that depends on the liver volume, $V_{\text{liv},i}$ (assuming that the number of cells per gram liver is constant). Using eq. (2.58), we obtained

$$\text{CL}_{\text{int},i} = V_{\text{liv},i} \cdot \frac{\text{CL}_{\text{int,ref}}}{V_{\text{liv,ref}}} = \text{SV}_{\text{liv},i} \cdot \text{CL}_{\text{int,ref}}, \tag{2.62}$$

where $\text{CL}_{\text{int,ref}}$ and $V_{\text{liv,ref}}$ are the intrinsic hepatic clearance and liver volume of the reference, respectively. $\text{SV}_{\text{liv},i}$ denotes the individual liver volume scaling factor. Exploiting eqs. (2.60) and (2.62), we obtain for the individual hepatic extraction ratio (based on eq. (2.24))

$$\text{E}_{\text{hep},i} = \frac{\text{SV}_{\text{liv},i} \cdot \text{CL}_{\text{int,ref}} \cdot K_{\text{liv}}}{\text{SQ}_i \cdot Q_{\text{liv,ref}} + \text{SV}_{\text{liv},i} \cdot \text{CL}_{\text{int,ref}} \cdot K_{\text{liv}}}, \tag{2.63}$$

where K_{liv} is the liver tissue-to-blood partition coefficient and $Q_{\text{liv,ref}}$ the reference hepatic blood flow. Based on $\text{E}_{\text{hep},i}$, the individual hepatic blood clearance is given by

$$\text{CL}_{\text{blood},i} = Q_{\text{liv},i} \cdot \text{E}_{\text{hep},i}, \tag{2.64}$$

where $Q_{\text{liv},i}$ denotes the individual hepatic blood flow.

Body height-based scaling approach

In [96], scaling factors for organ weights and cardiac output are specified. Assuming that the individual and reference organ/tissue densities do not differ, the organ weight scaling factors given in [96] also define tissue volume scaling factors. For all organs/tissues except adipose, brain and skin, the tissue volume scaling factor is given by

$$\text{SV}_{\text{tis},i} = \left(\frac{\text{BH}_i}{\text{BH}_{\text{ref}}} \right)^{3/4}, \tag{2.65}$$

where BH_i and $\mathrm{BH}_{\mathrm{ref}}$ denote the individual and reference body height [96]. The brain volume of individual 'i' is assumed to be equal to the reference one. Thus,

$$\mathrm{SV}_{\mathrm{bra},i} = 1. \tag{2.66}$$

For the skin volume, the scaling factor is given by

$$\mathrm{SV}_{\mathrm{ski},i} = \left(\frac{\mathrm{BW}_i}{\mathrm{BH}_i^2 \cdot \mathrm{BMI}_{\mathrm{ref}}}\right)^{0.5} \left(\frac{\mathrm{BH}_i}{\mathrm{BH}_{\mathrm{ref}}}\right)^{0.75}, \tag{2.67}$$

where BW_i and $\mathrm{BMI}_{\mathrm{ref}}$ denote the body weight of individual 'i' and the body mass index of the reference, respectively [96].

The adipose tissue weight is defined as the difference between the body weight and the sum over all non-adipose organ/tissue weights (lean body weight, LBW), resulting in

$$\mathrm{SV}_{\mathrm{adi},i} = \frac{\mathrm{BW}_i - \mathrm{LBW}_i}{\mathrm{BW}_{\mathrm{ref}} - \mathrm{LBW}_{\mathrm{ref}}} \tag{2.68}$$

with

$$\mathrm{LBW} = \sum_{\mathrm{tis}} V_{\mathrm{tis}} \cdot \mathrm{dens}_{\mathrm{tis}}, \tag{2.69}$$

where $\mathrm{dens}_{\mathrm{tis}}$ denotes the tissue density of organ/tissue 'tis'. In [96], the cardiac output scaling factor was given by

$$\mathrm{SQ}_i = \mathrm{SV}_{\mathrm{tis},i} = \left(\frac{\mathrm{BH}_i}{\mathrm{BH}_{\mathrm{ref}}}\right)^{3/4}. \tag{2.70}$$

For the individual hepatic intrinsic clearance, $\mathrm{CL}_{\mathrm{int},i}$, eq. (2.62) was applied. Since the tissue volume scaling factor of the liver and the cardiac output scaling factor are identical, eq. (2.63) for the individual hepatic extraction ratio simplifies to

$$\mathrm{E}_{\mathrm{hep},i} = \mathrm{E}_{\mathrm{hep,ref}} = \frac{\mathrm{CL}_{\mathrm{int,ref}} \cdot K_{\mathrm{liv}}}{Q_{\mathrm{liv,ref}} + \mathrm{CL}_{\mathrm{int,ref}} \cdot K_{\mathrm{liv}}}, \tag{2.71}$$

where $\mathrm{E}_{\mathrm{hep,ref}}$ is the hepatic extraction ratio for the reference individual. Since $\mathrm{E}_{\mathrm{hep},i} = \mathrm{E}_{\mathrm{hep,ref}}$, we omit the indices '$i$' and 'ref' in the following. Exploiting eqs. (2.64) and (2.70), the individual hepatic blood clearance can be specified in terms of reference parameters by

$$\mathrm{CL}_{\mathrm{blood},i} = \left(\frac{\mathrm{BH}_i}{\mathrm{BH}_{\mathrm{ref}}}\right)^{3/4} Q_{\mathrm{liv,ref}} \cdot \mathrm{E}_{\mathrm{hep}} \tag{2.72}$$

$$= \left(\frac{\mathrm{BH}_i}{\mathrm{BH}_{\mathrm{ref}}}\right)^{3/4} \mathrm{CL}_{\mathrm{blood,ref}}. \tag{2.73}$$

In [96], the above 'deterministic' scaling is followed by the addition of a random uncertainty on the scaled parameters. We omit this step since the aim of the study is to only consider explainable variability; see Discussion for more comments.

PBPK model predictions for a population of healthy male adults

Figure 2.16 depicts the diversity of venous blood concentration-time profiles for a virtually generated population of 500 healthy male adults. Each individual was characterized by its body height, BH_i, and its body mass index, BMI_i. The body weight, BW_i, was given by

$$\mathrm{BW}_i = \mathrm{BMI}_i \cdot \mathrm{BH}_i^2. \tag{2.74}$$

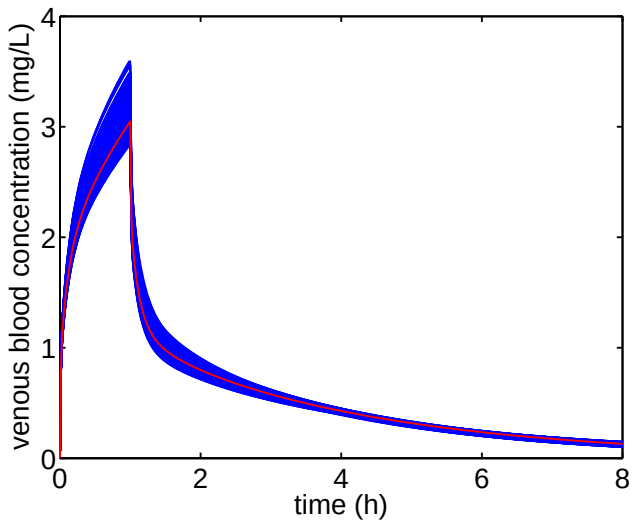

Figure 2.16: PBPK model predictions of the venous blood concentration for a population of 500 healthy male adults following a 60 min i.v. infusion of 400 mg Lidocaine. Individual PBPK model parameters were derived from a reference set of parameters (given in Table 2.1) and the body height-based scaling approach described in eqs. (2.65)-(2.72). The red line corresponds to the predicted venous blood concentration of the reference individual.

The algorithm for creating the virtual population is explained in the Appendix A.3. For our virtual population, the mean body height was 1.76 m, the mean body weight was 73 kg, and the mean body mass index was 23.59 kg/m^2. For illustration purposes and consistent with our running example in section 2.2.1, the simulations were based on a 60 min i.v. infusion of 400 mg Lidocaine for each individual. The reference set of tissue volumes and blood flows is given in Table 2.1 and the reference Lidocaine blood clearance is listed in Table 2.2. Individual PBPK model parameters were derived based on the body height-based scaling approach [96] presented above.

2.3.2 Classical Compartment Models with Mechanistic Covariates

In the sequel, we apply the lumping approach introduced in section 2.2.1 to derive low-dimensional compartment models with lumped model parameters incorporating the above scaling factors. The approach is illustrated in Figure 2.17.

Parameters of the low-dimensional compartment models

The reduction of the detailed whole-body PBPK model is based on the lumping approach as described in detail in section 2.2.1. Organs, tissues and blood spaces with similar kinetic behavior are grouped together, resulting in a low-dimensional compartment model with lumped compartment volumes, V_{L}, lumped blood flows, Q_{L}, lumped tissue-to-blood partition coefficients, K_{L}, and hepatic blood clearance, $\mathrm{CL}_{\mathrm{blood}}$. The lumped parameters are defined in eqs. (2.29), (2.31)-(2.33), respectively. The mechanistic interpretation of the lumped model is guaranteed, since the lumped parameters are functions of the parameters of the detailed whole-body PBPK model. For an individual 'i', the lumped parameters are specified

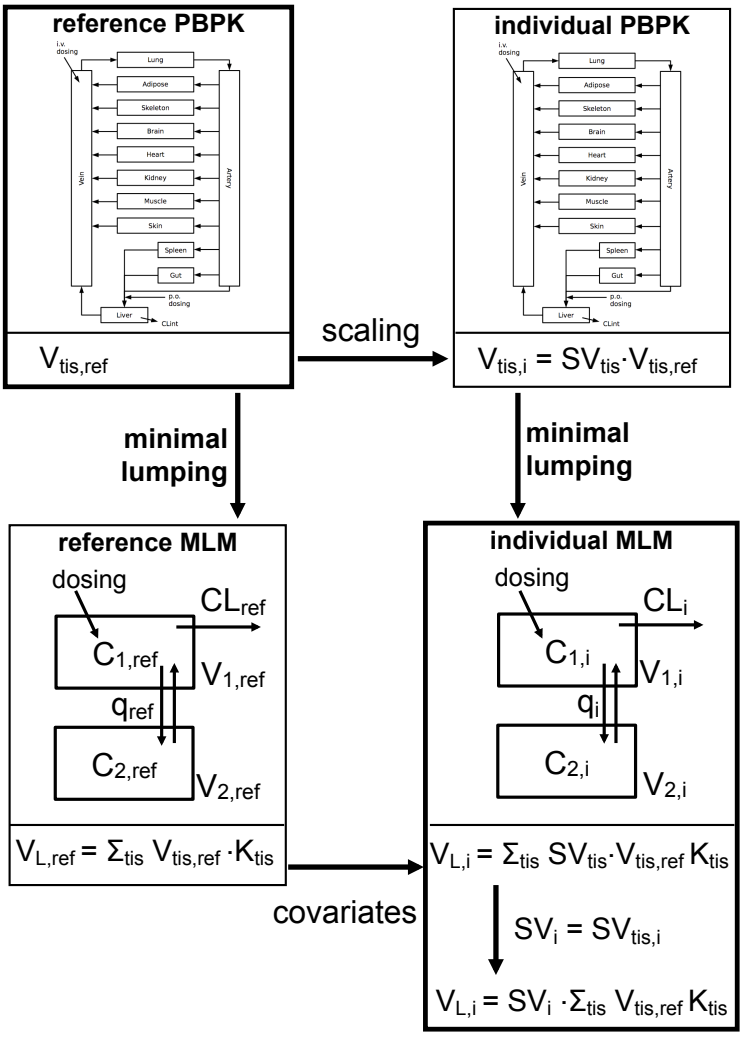

Figure 2.17: Illustration of the mechanistic approach to covariate modeling based on lumping of whole-body PBPK models. The PBPK model with a reference parameterization (denoted as reference PBPK) is the starting point. Applying the minimal lumping method to the reference PBPK model yielded a low-dimensional compartment model (MLM) with a reference parameterization. Applying our mechanistic covariate approach yielded a classical low-dimensional compartment model with individual parameter values. Note that the number of compartments and the structure of the low-dimensional compartment model depend on the drug under consideration.

in terms of the reference parameters based on eqs. (2.58), (2.60), (2.61) and (2.64) as follows

$$V_{\mathrm{L},i} = \sum_{\mathrm{tis}} \mathrm{SV}_{\mathrm{tis},i} \cdot V_{\mathrm{tis,ref}} \tag{2.75}$$

$$K_{\mathrm{L},i} = \frac{1}{V_{\mathrm{L},i}} \sum_{\mathrm{tis}} \mathrm{SV}_{\mathrm{tis},i} \cdot V_{\mathrm{tis,ref}} \cdot \widehat{K}_{\mathrm{tis}} \tag{2.76}$$

$$Q_{\mathrm{L},i} = \sum_{\mathrm{tis}} \mathrm{SQ}_i \cdot Q_{\mathrm{tis,ref}} \tag{2.77}$$

where the sum is taken over all tissues that are grouped together in the lumped compartment 'L'. Above, $\widehat{K}_{\mathrm{tis}}$ denotes the elimination corrected tissue-to-blood partition coefficient, defined as $\widehat{K}_{\mathrm{tis}} = (1 - \mathrm{E}_{\mathrm{tis}})K_{\mathrm{tis}}$ (eq. (2.26)). Here, $\mathrm{E}_{\mathrm{tis}}$ denotes the tissue-specific extraction

ratio. In our generic model, it is $E_{liv} = E_{hep}$ and $E_{tis} = 0$ for all other tissues. For artery and vein, we formally set $\widehat{K}_{ven} = \widehat{K}_{art} = 1$. For the hepatic blood clearance, we obtained

$$CL_{blood,i} = SQ_i \cdot Q_{liv,ref} \cdot E_{hep} = SQ_i \cdot CL_{blood,ref}. \tag{2.78}$$

Approximation of scaling factors

Consider a lumped compartment whose tissue volumes are all scaled with the same scaling factor SV_i, i.e., for all tissues, it is $SV_{tis,i} = SV_i$. Then, eq. (2.75) can be further simplified to

$$V_{L,i} = \sum_{tis} SV_{tis,i} \cdot V_{tis,ref} = SV_i \cdot \sum_{tis} V_{tis,ref} = SV_i \cdot V_{L,ref}. \tag{2.79}$$

Thus, the individual volume, $V_{L,i}$, can be derived from the reference volume, $V_{L,ref}$, employing SV_i. This is the defining characteristics of a mechanistic covariate approach. Since all blood flows are scaled identically with SQ_i, no approximations are needed.

For the body height-based approach [96], we defined the common volume scaling factor as

$$SV_i = \left(\frac{BH_i}{BH_{ref}}\right)^{3/4}. \tag{2.80}$$

For all tissues except adipose, brain and skin, it is $SV_{tis,i} = SV_i$. For brain and skin, we approximate their scaling factors $SV_{bra,i}$ and $SV_{ski,i}$ respectively, by SV_i. From the perspective of the drug pharmacokinetics in plasma or blood, this is a reliable approximation. Since the adipose tissue was considered of critical importance for predicting the pharmacokinetics of small molecule drugs, we retained its scaling factor $SV_{adi,i}$ defined in eq. (2.68). In summary, we used the scaling factor SV_i defined in eq. (2.65) for all organs/tissues, except for adipose, where we used $SV_{adi,i}$ defined in eq. (2.68). To denote the identical tissue volume and cardiac output scaling factors, we introduce

$$SF_i = SV_i = SQ_i. \tag{2.81}$$

In the following paragraph, we illustrate the mechanistic approach to covariate modeling for the scaling factors derived from the body height-based scaling approach.

Classical 1- and 2-compartment models with mechanistic covariates

For a large variety of drugs, it was demonstrated in section 2.2.6 that a minimal lumped 1- or a 2-compartment model is sufficient to accurately predict the venous blood concentration time profile. Based on the relation of the minimal lumped and classical pharmacokinetic parameters given in Figure 2.8, we obtained the classical 1- and 2-compartment model parameters incorporating mechanistic covariates.

The classical 1-compartment model was defined in eq. (2.3). For an individual parameterization, it is

$$V_{1,i}\frac{d}{dt}C_{1,i} = -CL_i \cdot C_{1,i} + r_{admin}, \tag{2.82}$$

where the covariate model on the parameters yields

$$V_{1,i} = SF_i \cdot V_{1,ref} + (SV_{adi,i} - SF_i) \cdot \widehat{K}_{adi} V_{adi,ref} \tag{2.83}$$

$$CL_i = SF_i \cdot CL_{ref} \tag{2.84}$$

with the common scaling factor, SF_i, defined in eq. (2.81) and the adipose tissue volume scaling factor, SV_{adi}, given in eq. (2.68).

The classical 2-compartment model was defined in eqs. (2.6)-(2.7). For an individual

parameterization, it is

$$V_{1,i}\frac{\mathrm{d}}{\mathrm{dt}}C_{1,i} = q_i\,(C_{2,i} - C_{1,i}) - \mathrm{CL}_i \cdot C_{1,i} + r_{\mathrm{admin}} \tag{2.85}$$

$$V_{2,i}\frac{\mathrm{d}}{\mathrm{dt}}C_{2,i} = q_i\,(C_{1,i} - C_{2,i}) \tag{2.86}$$

For the most common situation that the liver is part of the central compartment and the adipose tissue is part of the peripheral compartment (see section 2.2.6), the covariate model on the parameters yields

$$V_{1,i} = \mathrm{SF}_i \cdot V_{1,\mathrm{ref}} \tag{2.87}$$

$$V_{2,i} = \mathrm{SF}_i \cdot V_{2,\mathrm{ref}} + (\mathrm{SV}_{\mathrm{adi},i} - \mathrm{SF}_i) \cdot \widehat{K}_{\mathrm{adi}} V_{\mathrm{adi,ref}} \tag{2.88}$$

$$q_i = \mathrm{SF}_i \cdot q_{\mathrm{ref}} \tag{2.89}$$

$$\mathrm{CL}_i = \mathrm{SF}_i \cdot \mathrm{CL}_{\mathrm{ref}} \tag{2.90}$$

In a population analysis setting, the parameter values of the reference are taken to be the mean values of the study population.

2.3.3 Validation of the Mechanistic Approach to Covariate Modeling

In the sequel, we evaluate the low-dimensional compartment model with mechanistic covariates defined in eqs. (2.85) -(2.90) for a 2-compartment model.

Figure 2.18 shows the PBPK model predictions of the venous blood concentration for our virtually generated population of 500 healthy male adults (see Figure 2.16) in comparison to the predictions based on a low-dimensional 2-compartment model with mechanistic covariates following a 60 min i.v. infusion of 400 mg Lidocaine. The low-dimensional model was derived based on the minimal lumping for the reference; and individual parameterizations were obtained by applying our mechanistic covariate approach, eqs. (2.87)-(2.90). The resulting mechanistic low-dimensional compartment model comprised a peripheral compartment (containing adipose, skeleton and muscle) and a central compartment (containing all

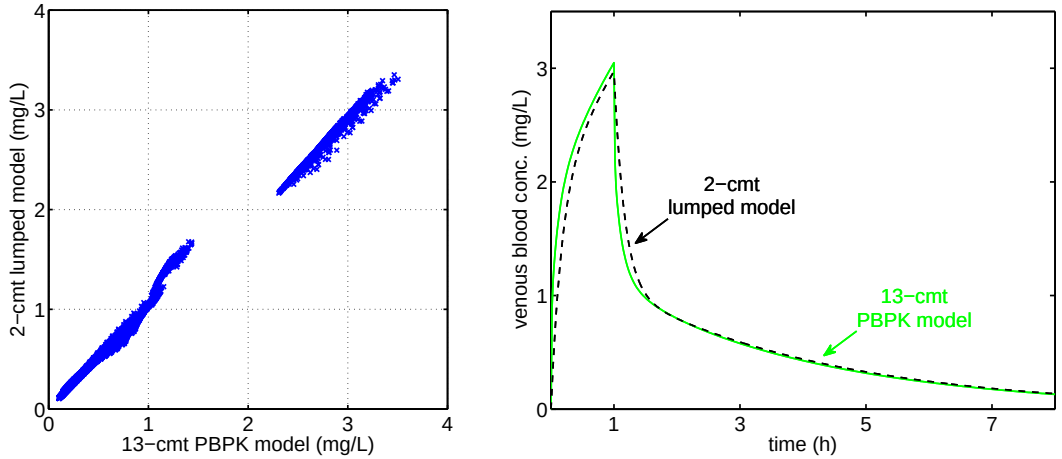

Figure 2.18: Whole-body PBPK versus mechanistic low-dimensional compartment model: Prediction of venous blood concentrations following a 60 min infusion of 400 mg Lidocaine for each individual. Left: Plot based on the virtual population of 500 healthy male adults at time points every 15 min. Right: Comparison of venous blood concentration-time profile for a single individual based on the PBPK model and the mechanistic 2-compartment model.

Table 2.5: Whole-body PBPK versus mechanistic low-dimensional compartment model: Statistics of PK parameters for a virtual population of 500 healthy male individuals after administration of 400 mg Lidocaine (60 min i.v. infusion), based on predicted venous blood concentration. Population mean values ± standard deviation.

		whole-body PBPK model with scaling factors	low-dimensional compartment model with mechanistic covariates
$C_{\max}$	mg/L	3.04 ± 0.12	3.00 ± 0.13
$\mathrm{AUC}(0 - T_{\mathrm{end}})$	mg/L/min	335.87 ± 11.71	344.95 ± 14.50
V_{ss}	L	187.84 ± 15.84	197.67 ± 19.96
$\mathrm{CL}_{\mathrm{blood}}$	L/min	1.10 ± 0.026	1.09 ± 0.035
$t_{1/2}$	min^{-1}	147.54 ± 14.60	149.88 ± 17.70

remaining organs/tissues).

As can be inferred from Figure 2.18, the scaling of the whole-body PBPK model and the mechanistic covariate modeling of the low-dimensional compartment model gives very comparable results. Based on the predicted venous blood concentration, we determined the PK parameters $C_{\max}$, $\mathrm{AUC}(0 - T_{\mathrm{end}})$, V_{ss} and $t_{1/2}$ (determination given in Appendix A.4). The population mean values and standard deviations of all PK parameters are listed in Table 2.5. Again, both approaches showed very good agreement.

2.3.4 Discussion and Conclusions

In the current analysis, we derived generic low-dimensional compartment models with mechanistic covariates based on the lumping of a whole-body PBPK model that incorporated scaling factors to determine individual physiological data from a reference set of parameters. The presented approach was illustrated for a population of healthy male adults as typically analyzed in clinical phase I studies but is also applicable to further populations as, e.g., children, if a respective reference set of physiological data is available.

Our general approach to scaling of physiological parameters allows for the integration of specific scaling factors and different scaling factor models. Here, we focussed on the scaling factor model presented in [96]. However, in order to create variability as present in a realistic population, the authors of [96] applied a stochastic variation factor to the individual tissue volumes and blood flows in addition to the deterministic scaling factors. In our study, we did not take into account the stochastic variation factors since we focussed on the derivation of mechanistic covariates that can explain the variability present in the physiological data. Research into the direction of defining scaling factors that better reflect variability in physiological data as present in a realistic population is ongoing [100].

In the general scaling approach, the parameters relevant for the determination of the tissue-to-blood partition coefficients (fraction of interstitial space, fraction of water, neutral lipids, and neutral phospholipids, protein content in plasma and interstitial space, hematocrit value) are assumed to be constant for all individuals resulting in constant tissue-to-blood partitioning. While for a homogenous population the assumption is reasonable, simulating a population of diverse individuals may have to consider possible variations in the tissue-to-blood partition coefficients.

The parameterization of the PBPK model with different reference sets of physiological data, e.g., for women, elderlies, children, etc., would allow for studying the influence of subpopulation characteristics on the structure and number of compartments of the classical pharmacokinetic model as well as the respective population mean pharmacokinetic data. However, the sparse availability of all relevant PBPK modeling data, in particular the blood flow rates, is a limiting factor in this regard. Updating the generic PBPK model for additional mechanistic processes, e.g., renal elimination, would allow for the integration of

further covariates such as creatinine clearance.

In conclusion, we presented a mechanistic approach to covariate modeling that can easily be integrated in any population pharmacokinetic analysis to account for inter-individual variability due to variations in tissue volumes and blood flows.

2.4 *Case Study* Monoclonal Antibody Disposition beyond Target Binding: Derivation of a Mechanistic Compartment Model

Therapeutic monoclonal antibodies (mAbs) are indicated in the treatment of diseases presenting specific antigens, including inflammatory and hematological diseases and cancer. For the past two decades, almost 30 mAbs have been registered at the U.S. Food and Drug Administration (FDA) [101] in these therapeutic areas. In the guideline on the clinical investigation of the pharmacokinetics of therapeutic proteins [102], the European Medicines Agency (EMEA) recommends population pharmacokinetic analysis to analyze the clinical data.

Despite the detailed mechanistic understanding of molecular processes involved in mAb disposition, there is no clear model-building strategy for low-dimensional compartment models suitable for the use in drug development. In [101], the pharmacokinetic studies of 27 commercialized mAbs are reviewed. For only half of the mAbs, the data are analyzed with a population approach. While in most of the cases, the pharmacokinetics of mAbs is described by an empirical 2-compartment disposition model, modeling of the elimination processes is quite diverse. It includes linear [103] or non-linear [104, 105] clearance from the central compartment, or parallel linear and non-linear clearances from the central and/or peripheral compartment(s) [106, 107].

The non-linearity in the pharmacokinetics is mainly attributed to the saturable binding to the target. Empirical Michaelis-Menten, target-mediated drug disposition (TMDD) [108–111], and lately, receptor-mediated endocytosis (RME) [112] models are applied to describe the non-linear clearance of mAbs. Much less is known about the physiological mechanisms supporting the linear elimination. Most of the mAbs present common structural properties and molecular mechanisms, independent of the binding to the target. For instance, the salvage by the neonatal Fc Receptor (FcRn) is the main process supposed to influence the disposition of such molecules in the absence of the target.

The saturable binding to FcRn is included into a pharmacokinetic model by [113] to describe the disposition of the anti-platelet antibody 7E3 in mice which do not express the target. The data are fitted by a 2-compartment model with the peripheral compartment representing the total endosomal space. Saturable binding to FcRn occurs in the peripheral compartment; the FcRn-bound mAb is recycled into the central compartment and the free mAb is eliminated via a linear clearance process. Later, a physiology-based pharmacokinetic (PBPK) model was developed by [114] in order to provide a better mechanistic understanding of the observed mAb data in mice. The PBPK model incorporates key features related to mAb disposition such as the presence of endogenous immunoglobulin G (IgG), convective transport from plasma into the interstitial space and via the lymph flow, as well as uptake into the endosomal cells via pinocytosis mediated by the competitive and saturable binding to FcRn.

The objective of this study is to translate the mechanistic understanding of mAb disposition, when the target is not expressed, in the form of a detailed PBPK model into the design of low-dimensional compartment models while retaining a mechanistic interpretation of the pharmacokinetic parameters. We extended the detailed PBPK model published in [114] which explicitly accounts for the non-linear and competitive binding of endogenous IgG and mAb to FcRn as well as the elimination of the unbound species in the endosomal spaces of all organs and tissues. Based on an extension of the lumping approach presented in the previous section, we reduced the dimensionality of the PBPK model and derived a low-dimensional mechanistic compartment model for the use in drug development. The results were illustrated for the mAb 7E3 in mice and are applicable to other mAbs and species.

2.4.1 A Generic PBPK Model for Monoclonal Antibody Disposition

We developed a generic PBPK model of endogenous IgG and mAb disposition in mice based on an extension of the PBPK model published by [114]. The PBPK model comprised 35 compartments representing the most relevant anatomical spaces involved in mAb disposition (see Figure 2.19): venous and arterial plasma as well as the plasma, endosomal and interstitial spaces of lung, adipose, skeleton, brain, heart, kidney, muscle, skin, gut, spleen and liver. Furthermore, the presence of endogenous IgG in addition to a mAb was considered. The model incorporated the following key processes of therapeutic and endogenous antibody disposition: i) distribution via the plasma flow; ii) transport into the interstitial space via convective transport through the paracellular pores in the vascular endothelium; iii) convective transport with the lymph fluid from the interstitial space into the plasma circulation; iv) uptake from the plasma and interstitial spaces into the endosomal compartments via fluid phase endocytosis; v) saturable binding to FcRn in the endosomal compartments; vi) return of FcRn-bound complexes to the plasma and interstitial spaces; vii) degradation of

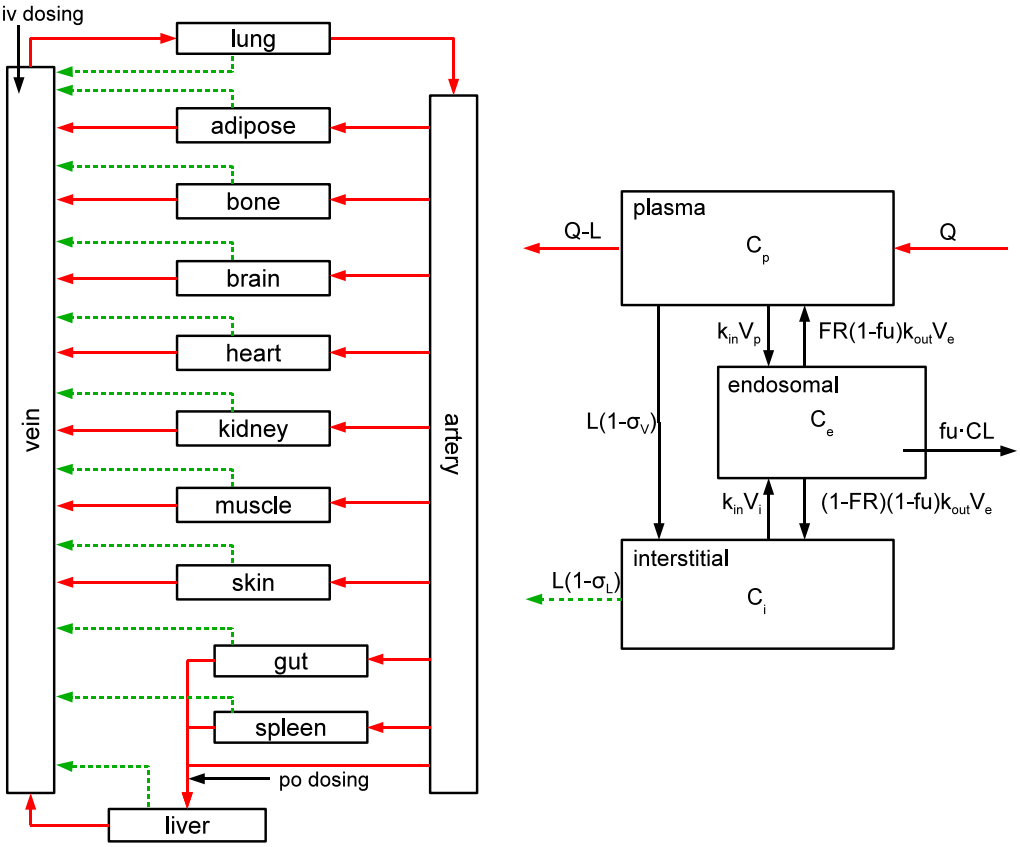

Figure 2.19: PBPK model structure. Left: Structure of the generic PBPK model for antibody pharmacokinetics. Organs, tissues and other spaces are interconnected by the plasma flow (red solid arrows) and the lymphatic system (green dashed arrows). Right: Detailed organ model comprising a plasma compartment, the endosomal and the interstitial spaces. P and L represent the plasma and lymph flow, σ_V and σ_L denote the vascular and lymphatic reflection coefficients, k_{in} is the rate of uptake of endogenous IgG or mAb from the plasma or interstitial space into the endosomal space. k_{out} describes the recycling of endogenous IgG or mAb from the endosomal space. In the endosomal space, the binding to the FcRn determines the fraction unbound fu. FR represents the fraction of FcRn-bound antibodies that is recycled to the plasma space. CL denotes the clearance of the unbound antibody in the endosomal space.

the unbound species in the endosomal spaces [114]. A detailed overview of all considered processes and the corresponding parameters can be found in Figure 2.19 (right).

Model equations

In the following, the term IgG will refer to the endogenous IgG concentration. The abbreviations of the organ/tissue names are given in Table 2.7. Based on previously developed whole-body PBPK models for mAb disposition [114–116], we derived a generic set of equations. The rates of change of the concentrations of endogenous IgG and mAb in plasma, endosomal and interstitial spaces of the different organs/tissues were given by the following system of ordinary differential equations (ODEs) with $C = \text{IgG}$ or $C = \text{mAb}$:

$$\begin{aligned} V_{\text{p,ven}} \frac{\text{d}}{\text{dt}} C_{\text{p,ven}} &= P_{\text{ven}} \cdot (C_{\text{in,ven}} - C_{\text{p,ven}}) + \sum_{\text{tis}} L_{\text{tis}} \cdot (1 - \sigma_{\text{L}}) \cdot C_{\text{i,tis}} + q_{\text{prod}} \\ &\qquad \text{tis} = \text{lun, adi, ske, bra, gut, hea, kid, liv, mus, ski, spl} \end{aligned} \tag{2.91}$$

$$V_{\text{p,art}} \frac{\text{d}}{\text{dt}} C_{\text{p,art}} = (P_{\text{lun}} - L_{\text{lun}}) \cdot C_{\text{p,lun}} - P_{\text{art}} \cdot C_{\text{p,art}} \tag{2.92}$$

$$\begin{aligned} V_{\text{p,tis}} \frac{\text{d}}{\text{dt}} C_{\text{p,tis}} = {} & P_{\text{tis}} \cdot C_{\text{in,tis}} - (P_{\text{tis}} - L_{\text{tis}}) \cdot C_{\text{p,tis}} \\ & - L_{\text{tis}} \cdot (1 - \sigma_{\text{V}}) \cdot C_{\text{p,tis}} - k_{\text{in}} \cdot V_{\text{p,tis}} \cdot C_{\text{p,tis}} \\ & + \text{FR} \cdot k_{\text{out}} \cdot V_{\text{tis,e}} \cdot (1 - \text{fu}_{\text{e,tis}}) \cdot C_{\text{tis,e}} \end{aligned} \tag{2.93}$$

$$\begin{aligned} V_{\text{e,tis}} \frac{\text{d}}{\text{dt}} C_{\text{e,tis}} = {} & + k_{\text{in}} \cdot V_{\text{p,tis}} \cdot C_{\text{p,tis}} + k_{\text{in}} \cdot V_{\text{tis,i}} \cdot C_{\text{tis,i}} \\ & - k_{\text{out}} \cdot V_{\text{e,tis}} \cdot (1 - \text{fu}_{\text{e,tis}}) \cdot C_{\text{e,tis}} - \text{CL}_{\text{e,tis}} \cdot \text{fu}_{\text{e,tis}} \cdot C_{\text{e,tis}} \end{aligned} \tag{2.94}$$

$$\begin{aligned} V_{\text{i,tis}} \frac{\text{d}}{\text{dt}} C_{\text{i,tis}} = {} & + L_{\text{tis}} \cdot (1 - \sigma_{\text{V}}) \cdot C_{\text{p,tis}} - L_{\text{tis}} \cdot (1 - \sigma_{\text{L}}) \cdot C_{\text{i,tis}} \\ & - k_{\text{in}} \cdot V_{\text{i,tis}} \cdot C_{\text{i,tis}} + (1 - \text{FR}) \cdot k_{\text{out}} \cdot V_{\text{e,tis}} \cdot (1 - \text{fu}_{\text{e,tis}}) \cdot C_{\text{e,tis}}. \end{aligned} \tag{2.95}$$

In the above equations, the subscripted concentrations $C_{\text{p,tis}}$, $C_{\text{e,tis}}$ and $C_{\text{i,tis}}$ denoted the total concentration in the plasma, endosomal, and interstitial spaces, respectively. The corresponding compartment volumes were denoted by $V_{\text{p,tis}}$, $V_{\text{e,tis}}$ and $V_{\text{i,tis}}$. The plasma and lymph flow were denoted by P_{tis} and L_{tis}, respectively. Moreover, σ_{V} and σ_{L} denoted the vascular and lymphatic reflection coefficients, respectively, and k_{in} and k_{out} denoted the endosomal uptake and the recirculation rates, respectively. The recirculation fraction of bound antibody from the endosomal space was denoted by FR. The concentration-dependent fraction unbound in endosomal space was denoted by $\text{fu}_{\text{e,tis}}$ and is defined in eq. (2.108). The unbound antibody in the endosomal space was subject to elimination with clearance $\text{CL}_{\text{e,tis}}$. For endogenous IgG, there was an additional constant rate of production q_{prod}, which was set to zero for the therapeutic mAb. For all organs/tissues except vein, artery, liver and lung, the inflowing concentration, $C_{\text{in,tis}}$, was given by

$$C_{\text{in,tis}} = C_{\text{p,art}}. \tag{2.96}$$

The inflowing liver and venous blood concentrations were defined by the blood flow weighted sum of organ/tissue concentrations supplying these compartments:

$$\begin{aligned} C_{\text{in,ven}} = {} & \sum_{\text{tis}} \left(P_{\text{tis}} - L_{\text{tis}}\right) / P_{\text{lun}} \cdot C_{\text{p,tis}} \\ & \text{tis} = \text{adi, ske, bra, hea, kid, liv, mus, ski} \end{aligned} \tag{2.97}$$

$$\begin{aligned} C_{\text{in,liv}} = {} & \sum_{\text{tis}} (P_{\text{tis}} - L_{\text{tis}}) / P_{\text{liv}} \cdot C_{\text{p,tis}} + \left(P_{\text{liv}} - \sum_{\text{tis}} (P_{\text{tis}} - L_{\text{tis}}) \right) / P_{\text{liv}} \cdot C_{\text{p,art}} \\ & \text{tis} = \text{spl, gut}. \end{aligned} \tag{2.98}$$

For artery and lung, it was

$$C_{\text{in,art}} = C_{\text{p,lun}} \tag{2.99}$$
$$C_{\text{in,lun}} = C_{\text{p,ven}}. \tag{2.100}$$

The mAb was administered via an i.v. bolus infusion. For the vein, the initial condition of the above system of ODEs was set to

$$C(t=0) = \frac{\text{dose}}{V_{\text{p,ven}}}. \tag{2.101}$$

In the endosomal space of each tissue, free endogenous IgG and free mAb competitively bind to free FcRn:

$$\text{mAb}_\text{u} + \text{FcRn}_\text{u} \overset{K_\text{D}}{\longleftrightarrow} \text{mAb} : \text{FcRn}$$
$$\text{IgG}_\text{u} + \text{FcRn}_\text{u} \overset{K_\text{D}}{\longleftrightarrow} \text{IgG} : \text{FcRn},$$

where K_D denoted the corresponding dissociation constant. In the present work, we assumed that i) the K_D values of endogenous IgG and mAb are identical, ii) FcRn is expressed in all organs/tissues, and iii) due to lack of more detailed information, that the total FcRn concentration in each endosomal space is identical. The impact of these assumptions is commented on in the Discussion. The conservation of mass then implies that

$$\text{FcRn}_\text{tot} = \text{FcRn}_\text{u} + \text{IgG}_\text{b} + \text{mAb}_\text{b}, \tag{2.102}$$

where FcRn_tot and FcRn_u denote the free and total concentrations of FcRn and where IgG_b and mAb_b denote the FcRn-bound concentrations of endogenous IgG and mAb, respectively. For endogenous IgG as well as for mAb, the concentration in the endosomal space satisfies

$$C_\text{tot} = C_\text{u} + C_\text{b}. \tag{2.103}$$

Table 2.6: Summary of the physiological parameters of the PBPK model.

Parameter			Ref.	Description
V_x	ml	Table 2.7		$x = \text{p}, \text{i}, \text{e}$; plasma, interstitial, endosomal volume (tissue-specific)
P	ml/min	Table 2.7		plasma flow (tissue-specific)
L	ml/min	Table 2.7		lymph flow (tissue-specific)
σ_V		0.95	[114, 117]	vascular reflection coefficient
σ_L		0.20	[114]	lymphatic reflection coefficient
k_in	1/day	1.75	fit	endosomal uptake rate
k_out	1/day	2.91	fit	recirculation rate of bound antibody
FR		0.72	[114]	fraction of recirculated bound antibody (see also Discussion section for comment on identifiability)
k_deg	1/day	0.06	fit	degradation rate constant of free antibody from endosomal space (tissue-specific)
FcRn	nM	1.48e5	fit	FcRn capacity
K_D	nM	4.80	[118]	dissociation constant of the antibody-FcRn binding
q_prod	nmol/day	2.09	fit	constant production of endogenous IgG

Binding processes are typically fast in comparison to the time-scale of the other pharmacokinetic processes. Assuming a quasi-steady state for FcRn binding yields

$$C_{\mathrm{u}} \cdot \mathrm{FcRn}_{\mathrm{u}} = K_{\mathrm{D}} \cdot C_{\mathrm{b}}, \tag{2.104}$$

where C_{b} denotes the FcRn-bound concentrations of endogenous IgG and mAb. Solving for the bound concentration results in

$$C_{\mathrm{b}} = \frac{\mathrm{FcRn}_{\mathrm{u}}}{K_{\mathrm{D}} + \mathrm{FcRn}_{\mathrm{u}}} \cdot C_{\mathrm{tot}}. \tag{2.105}$$

Inserting relation (2.105) for $C = \mathrm{IgG}$ and $C = \mathrm{mAb}$ into eq. (2.102), we obtain

$$\mathrm{FcRn}_{\mathrm{tot}} = \mathrm{FcRn}_{\mathrm{u}} + \frac{\mathrm{FcRn}_{\mathrm{u}}}{K_{\mathrm{D}} + \mathrm{FcRn}_{\mathrm{u}}}\mathrm{IgG}_{\mathrm{tot}} + \frac{\mathrm{FcRn}_{\mathrm{u}}}{K_{\mathrm{D}} + \mathrm{FcRn}_{\mathrm{u}}}\mathrm{mAb}_{\mathrm{tot}}. \tag{2.106}$$

Solving eq. (2.106) for $\mathrm{FcRn}_{\mathrm{u}}$ yields

$$\begin{aligned}\mathrm{FcRn}_{\mathrm{u}} = &\frac{1}{2}\Big(\mathrm{FcRn}_{\mathrm{tot}} - \mathrm{IgG}_{\mathrm{tot}} - \mathrm{mAb}_{\mathrm{tot}} - K_{\mathrm{D}} \ + \ldots \\ &\sqrt{(\mathrm{FcRn}_{\mathrm{tot}} - \mathrm{IgG}_{\mathrm{tot}} - \mathrm{mAb}_{\mathrm{tot}} - K_{\mathrm{D}})^2 + 4K_{\mathrm{D}} \cdot \mathrm{FcRn}_{\mathrm{tot}}}\Big).\end{aligned} \tag{2.107}$$

This finally allows us to determine the (concentration-dependent) fraction unbound for endogenous IgG and mAb based on $\mathrm{fu} = C_{\mathrm{u}}/C_{\mathrm{tot}}$ and eq. (2.105):

$$\mathrm{fu}_{\mathrm{IgG}} = \mathrm{fu}_{\mathrm{mAb}} = \frac{C_{\mathrm{u}}}{C_{\mathrm{tot}}} = \frac{K_{\mathrm{D}}}{K_{\mathrm{D}} + \mathrm{FcRn}_{\mathrm{u}}} \tag{2.108}$$

with $\mathrm{FcRn}_{\mathrm{u}}$ defined in eq. (2.107). For large total concentration of endogenous IgG or mAb, eq. (2.107) yields $\mathrm{FcRn}_{\mathrm{u}} \approx 0$, implying $\mathrm{fu} \approx 1$. This is in accordance with the expectation that binding to FcRn is a saturable process, resulting in increasingly larger unbound concentration of endogenous IgG or mAb with increasing total endogenous IgG or total mAb concentration, respectively.

Model parameterization

A description of all parameters of the PBPK model is given in Table 2.6. Physiological and anatomical data were taken from [114, 115, 119–121] and are summarized in Table 2.7. Note that in [114, 115], the plasma space of each organ/tissue was simplistically denoted as 'vascular space'. However, in the original work [115, p. 1518, 4th paragraph], the cited values were reported as 'vascular (plasma) space'. Hence, the plasma space in our PBPK model is equivalent to the values of the 'vascular space' in [114, 115].

We used the full PBPK model stated in eqs. (2.91)-(2.95) to estimate five of six unknown model parameters from experimental data, since not all parameters were explicitly given in the literature [114, 115, 119–121]: total FcRn capacity, $\mathrm{FcRn}_{\mathrm{tot}}$, the rate of influx into the endosomal compartments, k_{in}, the rate of efflux out of the endosomal compartments, k_{out}, the degradation rate constant, k_{deg}, and the constant production of endogenous IgG, q_{prod} (see Figure 2.19 for an overview of all model parameters). We assumed $\mathrm{FcRn}_{\mathrm{tot}}$, k_{in}, k_{out}, and k_{deg} to be tissue-independent. Tissue-specific clearances were obtained as follows:

$$\mathrm{CL}_{\mathrm{e,tis}} = k_{\mathrm{deg}} \cdot V_{\mathrm{e,tis}}, \tag{2.109}$$

where $V_{\mathrm{e,tis}}$ is the tissue-specific volume of the endosomal space. The sixth unknown parameter was the fraction of recirculated bound antibody, FR. It was set to $\mathrm{FR} = 0.715$, as published in [114]. Our own analysis showed that the PBPK model is robust to changes in FR, given only experimental data in the plasma compartment. This can also be theoretically understood from the pre-lumping step (see Appendix B.5.2 for details), since the parameter

'disappears' during the pre-lumping procedure. In other words, our analysis showed that the value of FR cannot be accurately determined given only the above plasma data. We remark that the exact choice of FR does not influence the subsequently presented PBPK modeling and lumping results.

Experimental data on FcRn-knockout and wild-type were extracted from [113, Figure 2.20] using the software DigitizeIt, version 1.5.8a, I. Bormann 2001-2006. The experimental data included measurements of 7E3 in the venous plasma. Additionally, the concentration of endogenous IgG in plasma was reported in [113, 122]. The parameters were fitted using a two step approach. In the first step, we used the FcRn-knockout data to fit k_{in}. In the knockout scenario, recirculation of mAb is prevented since no binding to FcRn takes place which is necessary for exporting mAb out of the endosomal spaces. Therefore, solely the disappearance of mAb due to its uptake from plasma and interstitial into endosomal spaces is present in the experimental data. In the second step, we fitted the full PBPK model simultaneously to the mAb concentration in the wild-type and to the endogenous IgG concentration to determine k_{out}, k_{deg}, FcRn_{tot}, and q_{prod}. The resulting model predictions are shown in Figure 2.20.

Table 2.7: Species-dependent parameters of the PBPK model for mice.

		V_{tot} mL	V_{p} mL	V_{i} mL	$V_{\text{e}}{}^{h}$ 10^{-2}mL	P^{i} mL/min	L^{j} 10^{-2}mL/min
Adipose	(adi)	1.750[b]	0.001[d]	0.236[e]	0.875	0.31[f]	0.124
Brain	(bra)	0.360[c]	0.007[d]	0.0014[e]	0.180	0.14[f]	0.056
Gut	(gut)	3.450[a]	0.100[a]	0.600[a]	1.725	0.90[a]	0.180
Heart	(hea)	0.133[a]	0.007[a]	0.019[a]	0.067	0.28[a]	0.112
Kidney	(kid)	0.298[a]	0.030[a]	0.101[a]	0.149	0.80[a]	0.320
Liver	(liv)	0.951[a]	0.095[a]	0.190[a]	0.476	1.10[a]	0.220
Lung	(lun)	0.191[a]	0.019[a]	0.057[a]	0.096	4.38[a]	1.752
Muscle	(mus)	7.924[a]	0.150[a]	1.032[a]	3.962	0.80[a]	0.320
Skeleton	(ske)	1.500[a]	0.080[a]	0.280[a]	0.750	0.17[a]	0.068
Skin	(ski)	2.940[a]	0.200[a]	0.999[a]	1.470	1.21[a]	0.484
Spleen	(spl)	0.100[a]	0.010[a]	0.020[a]	0.050	0.05[a]	0.010
Artery	(art)	0.219[g]	0.219[g]	-	-	4.38[a]	-
Vein	(ven)	0.536[g]	0.536[g]	-	-	4.38[a]	-

[a] from [114, 115]. Note that in [114, 115], the plasma space of each organ/tissue is simplistically denoted as 'vascular space'. See text for more details.
[b] 7% of total body weight [119] assuming a body weight of 25 g and a tissue density of 1 g/mL
[c] from [120]
[d] total vacular volume (V_{vas}) in adipose: 1.00 %, in brain: 3.7 % of total volume (measured in rats but assumed to be species-independent for mammals) [121]; $V_{\text{p}} = (1 - \text{hct})V_{\text{vas}}$ with hct = 0.45 [120]
[e] adipose: 1.35 %, brain: 0.4 % of total volume [121]
[f] plasma flow in adipose tissue: 7.0% and brain: 3.3% of total plasma flow [119]
[g] total plasma volume $V_{\text{plasma}} = 1.25$ ml (assuming a body weight of 25 g) [120],
$V_{\text{art}} = 0.29 \cdot (V_{\text{plasma}} - \sum V_{\text{p,tis}})$, $V_{\text{ven}} = 0.71 \cdot (V_{\text{plasma}} - \sum V_{\text{p,tis}})$ [119]
[h] assumed to be 0.5 % of tissue volume [114]
[i] The sum of individual organ plasma flows [114, 115, 119] exceeds the observed total plasma flow of vein, lung, and artery [120, for hct = 0.45]. For consistency, we set the total plasma flow to the sum of all plasma flows entering the vein.
[j] assumed to be 2 % and 4 % of plasma flow for visceral and non-visceral organs, respectively [114]

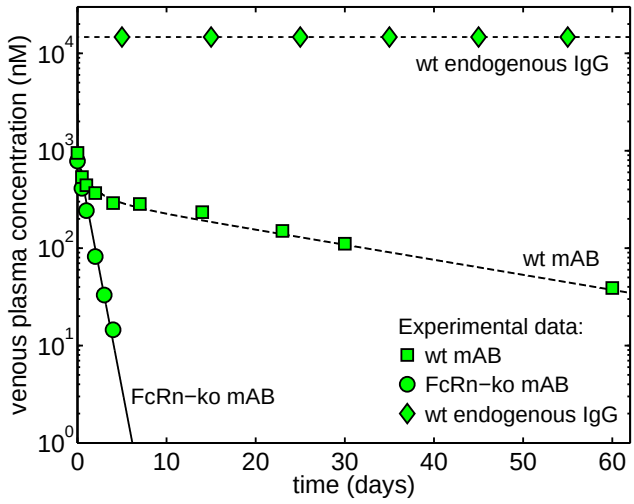

Figure 2.20: *In silico* predictions based on the full PBPK model and *in vivo* plasma data for an i.v. bolus administration of 8 mg/kg 7E3 in wild-type (wt) and FcRn-knockout (FcRn-ko) mice (experimental data extracted from [113, Figure 1]). In addition, the endogenous IgG level reported in wt mice is shown.

PBPK model predictions and fraction unbound in the endosomal spaces

The predictions of the generic PBPK model applied to 7E3 following an i.v. bolus administration of 8 mg/kg 7E3 (as in [114]) are shown in Figure 2.21, exemplified for six organs/tissues.

Simulations that included both, 7E3 and endogenous IgG, were performed as follows: Endogenous IgG levels prior to 7E3 administration were determined by simulating the PBPK model with initial concentrations of 7E3 set to zero in all compartments. The resulting steady state levels of endogenous IgG served as initial conditions for the simulations including 7E3 administration.

The PBPK modeling results revealed that the level of free FcRn, $\mathrm{FcRn_u}$, is not influenced by the presence of mAb, but is solely determined by the concentration of endogenous IgG, if i) both, endogenous IgG and mAb, possess a similar affinity to FcRn, and ii) the concentration of endogenous IgG is much higher than the concentration of the mAb. In our model, endogenous IgG and mAb are assumed to possess the same K_{D}. Moreover, the total concentration of endogenous IgG (in mice) has been reported to be in the nM range [113, 122], thus being 1-2 orders of magnitude larger than the mAb concentration immediately after drug administration in plasma (see Figure 2.20) as well as in the endosomal spaces (data not shown). Additionally, the concentration of endogenous IgG is in steady state in the absence of mAb and the steady state level is hardly influenced by the mAb administration, i.e, endogenous IgG levels are approximately constant over time. Thus, the fraction unbound of endogenous IgG and mAb as given in eq. (2.108) is also approximately constant over time. We will make use of this observation in the subsequent lumping step. Parameter values of the fraction unbound are found in Table 2.8. A detailed discussion on these results is beyond the scope of the present study, however, for details see our recent publication [123].

2.4.2 Mechanistic Lumping of the PBPK Model

In the sequel, we reduce the dimensionality of the detailed PBPK model for mAb disposition and relate the resulting lumped models to existing empirical ones based on the novel lumping approach presented in section 2.2.1. The different structure of the PBPK model for mAb disposition requires an extension of the approach. In a first step, we determine a partially

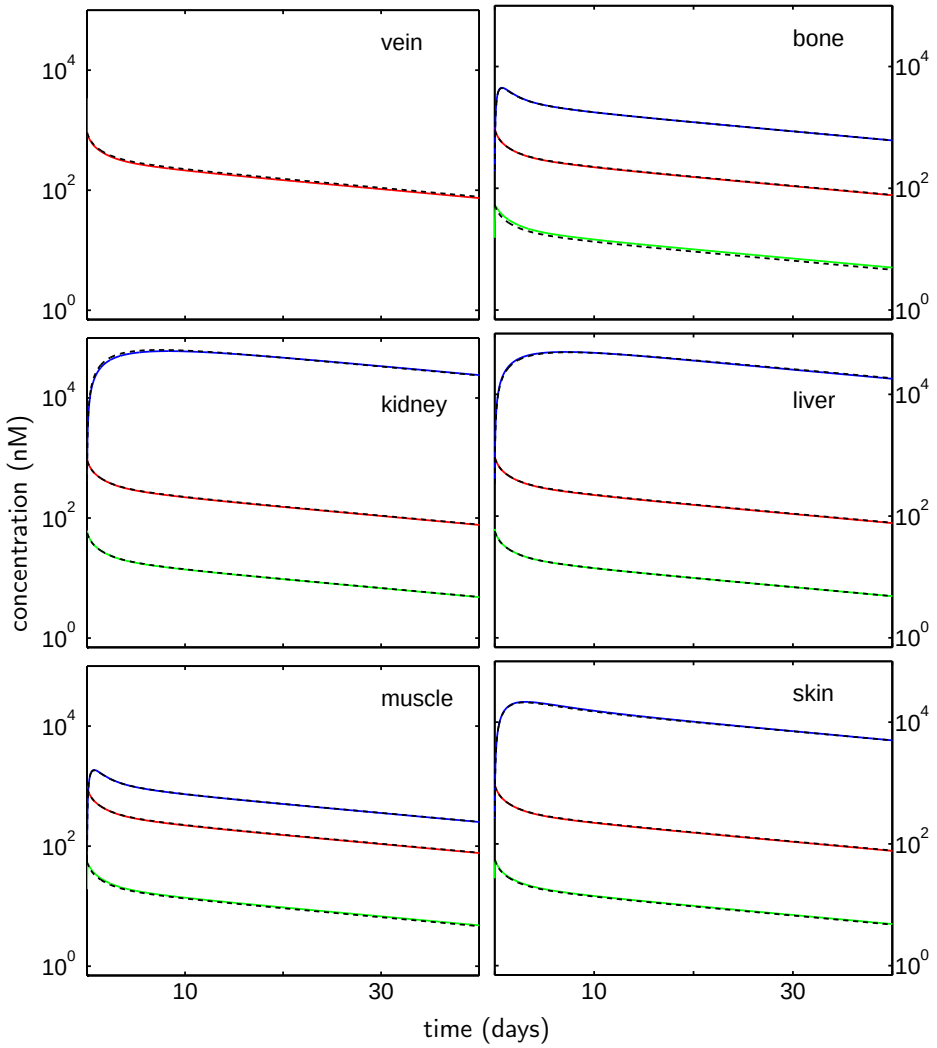

Figure 2.21: Predicted concentration-time profiles in the plasma (red), interstitial (green), and endosomal (blue) compartments for different organs/tissues following an i.v. bolus administration of 8 mg/kg 7E3 in mice. Solid line: PBPK model comprising 35 compartments. Dashed line: Mechanistically lumped 4-compartment model comprising a central compartment (all plasma and interstitial spaces), and three endosomal compartments (see Figure 2.23 and Results section for more details). The choice of the tissues and organs is illustrative; the approximation quality in the compartments not shown is identical to those shown.

lumped model that subsequently allows us to determine partition coefficients required to apply the lumping approach.

Identification of lumped compartments

Figure 2.22 (left) depicts the concentration-time profiles of all (sub-)compartments of the detailed PBPK model scaled according to

$$\text{Normalized concentration} = \frac{C_{\mathrm{x,tis}}(t)}{C_{\mathrm{x,tis}}(t_{\mathrm{el}})}, \tag{2.110}$$

where $C_{\mathrm{x,tis}}(t)$ with $\mathrm{x} = \mathrm{p}, \mathrm{e}, \mathrm{i}$ denotes the total mAb concentration in plasma, endosomal or interstitial space of an organ/tissue considered in the PBPK model. The time t_{el} had to lie safely in the quasi-steady state elimination phase; we chose 40 days for the mAb 7E3. This

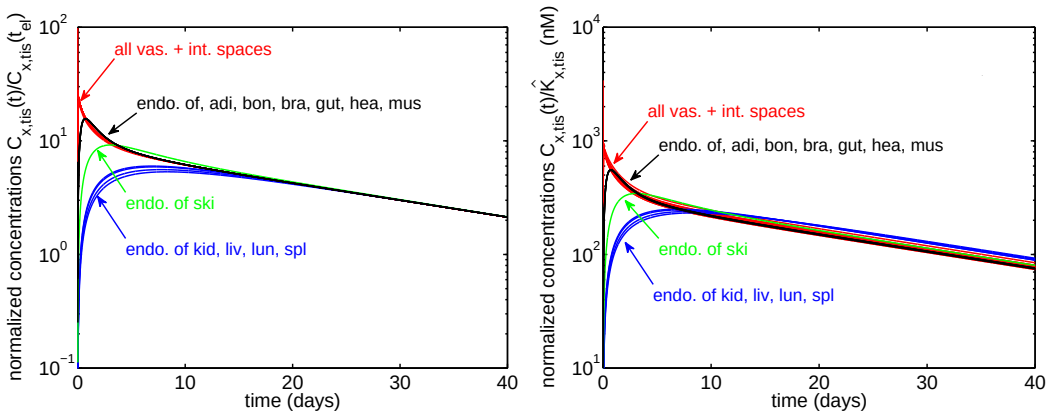

Figure 2.22: Identification of groups of compartments for the lumping approach. Normalized concentrations of the plasma, interstitial and endosomal spaces of the different compartments based on predictions of the full PBPK model after an i.v. bolus administration of 8 mg/kg 7E3 to wild-type mice. Left: Normalized concentrations $C_{\mathrm{x,tis}}(t)/C_{\mathrm{x,tis}}(t_{\mathrm{el}})$ based on concentration $C_{\mathrm{x,tis}}(t_{\mathrm{el}})$ that lies in the elimination phase; see eq. (2.110). We choose $t_{\mathrm{el}} = 40$ days. Right: Normalized concentrations $C_{\mathrm{x,tis}}(t)/\widehat{K}_{\mathrm{x,tis}}$ based on the elimination-corrected partition coefficient $\widehat{K}_{\mathrm{x,tis}}$; see eqs. (2.111) and (2.112). Similar concentration-time profiles are indicated by the same color/annotation.

scaling clearly showed four groups of compartments with similar kinetics that differ in the initial distributional phase.

While the scaling in eq. (2.110) is generally applicable to any predictions, a slightly different normalization exploiting partition coefficients is required for the lumping approach, see section 2.2.1. Here, each concentration-time profile was normalized by its elimination-corrected plasma partition coefficient

$$\widehat{K}_{\mathrm{x,tis}} \quad = \quad K_{\mathrm{x,tis}} \cdot (1 - \mathrm{E}_{\mathrm{x,tis}}) \tag{2.111}$$

resulting in

$$\text{Normalized concentration} \quad = \quad \frac{C_{\mathrm{x,tis}}}{\widehat{K}_{\mathrm{x,tis}}}. \tag{2.112}$$

The endosomal-to-plasma partition coefficients, $K_{\mathrm{e,tis}}$, and the interstitial-to-plasma partition coefficients, $K_{\mathrm{i,tis}}$, were derived from the original parameters of the detailed PBPK model involving, e.g., the lymph flow, the reflection coefficients, and the uptake and recirculation rates. For details see Appendix B.5 in particular eqs. (B.47) and (B.59). The resulting numerical values are given in Table 2.8. For all plasma concentrations, we formally set $\widehat{K}_{\mathrm{p,tis}} = 1$. Metabolism occured only in the endosomal space of the organs/tissues so that, for plasma and interstitial spaces, the extraction ratios were $\mathrm{E}_{\mathrm{p,tis}} = \mathrm{E}_{\mathrm{i,tis}} = 0$. For the endosomal spaces, $\mathrm{E}_{\mathrm{e,tis}}$ was defined as

$$\mathrm{E}_{\mathrm{e,tis}} = \frac{\mathrm{CL}_{\mathrm{e,tis}} \cdot \mathrm{fu}_{\mathrm{e,tis}} \cdot K_{\mathrm{e,tis}}}{D_{\mathrm{tis}} + \mathrm{CL}_{\mathrm{e,tis}} \cdot \mathrm{fu}_{\mathrm{e,tis}} \cdot K_{\mathrm{e,tis}}}, \tag{2.113}$$

where $\mathrm{CL}_{\mathrm{e,tis}}$ and $\mathrm{fu}_{\mathrm{e,tis}}$ are the endosomal clearances and the fraction unbound in the endosomal spaces, respectively. The term D_{tis} takes the role of a permeability constant in [volume/time] and was given by

$$D_{\mathrm{tis}} = \frac{Q_{\mathrm{tis}} \cdot k_{\mathrm{out}} V_{\mathrm{e,tis}} (1 - \mathrm{fu}_{\mathrm{e,tis}}) \cdot K_{\mathrm{e,tis}}}{Q_{\mathrm{tis}} + k_{\mathrm{out}} V_{\mathrm{e,tis}} (1 - \mathrm{fu}_{\mathrm{e,tis}}) \cdot K_{\mathrm{e,tis}}} \tag{2.114}$$

where k_{out} was the recirculation rate of bound antibody, and $V_{\mathrm{e,tis}}$ was the volume of the

endosomal compartment of the corresponding tissue.

Figure 2.22 (right) shows the concentration-time profiles of all compartments (i.e., plasma, endosomal, interstitial spaces) of the full PBPK model normalized by their respective elimination-corrected plasma partition coefficient according to eq. (2.112) for the mAb 7E3. Based on Figure 2.22, we identified four groups of similar concentration-time profiles: {all plasma and interstitial spaces}, {endosomal spaces of adipose, skeleton, brain, gut, heart, muscle}, {endosomal space of skin}, {endosomal spaces of kidney, liver, lung, spleen}. These four groups defined the lumped compartments of the reduced 4-compartment model for 7E3.

Table 2.8: Endosomal-to-plasma and interstitial-to-plasma partition coefficients, $K_{\mathrm{e,tis}}$ and $K_{\mathrm{i,tis}}$, respectively, based on eqs. (B.47) and (B.59) and the parameter values given in Tables 2.6 and 2.7.

	$K_{\mathrm{e,tis}}$	$K_{\mathrm{i,tis}}$	$\mathrm{fu}_{\mathrm{e,tis}}$
Adipose	1.10	0.0607	0.36e-4
Brain	2.46	0.0625	0.43e-4
Gut	4.82	0.0595	0.63e-4
Heart	7.64	0.0623	1.34e-4
Kidney	393.62	0.0622	0.96
Liver	281.43	0.0621	0.95
Lung	338.57	0.0625	0.97
Muscle	3.34	0.0596	0.49e-4
Skeleton	8.04	0.0588	1.72e-4
Skin	69.43	0.0606	0.84
Spleen	262.54	0.0607	0.95

Parameters and equations of the mechanistically lumped model

The reduced PBPK model is schematically depicted in Figure 2.23 (top). The central compartment 'cen' contained the venous plasma and all other plasma and interstitial spaces. Following eq. (2.29), the volumes of the central and the lumped endosomal compartments were defined as

$$V_{\mathrm{cen}} = V_{\mathrm{p,ven}} + V_{\mathrm{p,art}} + \sum_{\mathrm{tis}} (V_{\mathrm{p,tis}} + V_{\mathrm{i,tis}}) \tag{2.115}$$

$$V_{\mathrm{L}} = \sum_{\mathrm{tis}} V_{\mathrm{e,tis}}, \tag{2.116}$$

where the first sum was taken over all organs/tissues of the PBPK model and the second sum was taken over all organs/tissues whose endosomal spaces were lumped together. The lumped central and endosomal partition coefficients were defined as

$$K_{\mathrm{cen}} = \frac{1}{V_{\mathrm{cen}}} \sum_{\mathrm{tis}} (V_{\mathrm{p,tis}} + V_{\mathrm{i,tis}} \cdot \widehat{K}_{\mathrm{i,tis}}) \tag{2.117}$$

$$K_{\mathrm{L}} = \frac{1}{V_{\mathrm{L}}} \sum_{\mathrm{tis}} V_{\mathrm{e,tis}} \cdot \widehat{K}_{\mathrm{e,tis}}, \tag{2.118}$$

where the first sum is taken over all organs/tissues of the PBPK model and the second sum is taken over all organs/tissues whose endosomal spaces were lumped together. The

exchange flows into and out of the lumped endosomal compartments were given by

$$q_{\text{in,L}} = k_{\text{in}} \sum_{\text{tis}} (V_{\text{p,tis}} + V_{\text{i,tis}}) \tag{2.119}$$

$$q_{\text{out,L}} = k_{\text{out}} V_{\text{L}}, \tag{2.120}$$

where the sum is taken over all organs/tissues whose endosomal spaces were lumped together. The fraction unbound in a lumped endosomal compartment was defined as

$$\text{fu}_{\text{L}} = \frac{1}{V_{\text{L}} K_{\text{L}}} \sum_{\text{tis}} V_{\text{e,tis}} \widehat{K}_{\text{e,tis}} \cdot \text{fu}_{\text{e,tis}}, \tag{2.121}$$

where the sum is taken over all organs/tissues whose endosomal spaces were lumped together. The above expression can be interpreted as the volume of distribution-weighted sum of $\text{fu}_{\text{e,tis}}$ values. Hence, the more antibody distributes into the endosomal space of a certain tissue, the higher is the impact of the corresponding $\text{fu}_{\text{e,tis}}$ to the lumped fu_{L}. The clearance of a lumped compartment was the sum of individual endosomal clearances

$$\text{CL}_{\text{L}} = \sum_{\text{tis}} \text{CL}_{\text{e,tis}} \tag{2.122}$$

of the organs/tissues whose endosomal spaces were lumped together. For the rate of change of the central concentration, C_{cen}, and the 3 lumped endosomal concentrations, $C_{\text{L}i}$ with $i = 1, 2, 3$, we obtained the following system of ODEs:

$$V_{\text{cen}} \frac{\text{d}}{\text{dt}} C_{\text{cen}} = \sum_{i} q_{\text{out,L}i} (1 - \text{fu}_{\text{L}i}) \cdot C_{\text{L}i} - \sum_{i} q_{\text{in,L}i} \cdot C_{\text{cen}} \tag{2.123}$$

$$V_{\text{L}i} \frac{\text{d}}{\text{dt}} C_{\text{L}i} = q_{\text{in,L}i} \cdot C_{\text{cen}} - q_{\text{out,L}i} (1 - \text{fu}_{\text{L}i}) \cdot C_{\text{L}i} - \text{CL}_{\text{L}i} \text{fu}_{\text{L}i} \cdot C_{\text{L}i}. \tag{2.124}$$

As outlined in section 2.2.1, the concentrations of the compartments of the detailed PBPK model can be regained from the lumped concentrations based on the following scaling conditions

$$C_{\text{p,tis}} = \frac{C_{\text{cen}}}{K_{\text{cen}}} \tag{2.125}$$

$$C_{\text{e,tis}} = \widehat{K}_{\text{e,tis}} \frac{C_{\text{L}}}{K_{\text{L}}} \tag{2.126}$$

$$C_{\text{i,tis}} = \widehat{K}_{\text{i,tis}} \frac{C_{\text{cen}}}{K_{\text{cen}}}. \tag{2.127}$$

Figure 2.21 shows the predicted concentration-time profiles in the plasma, interstitial and endosomal spaces of different organs/tissues based on the lumped 4-compartment model and the detailed 35-compartment PBPK model. As can be inferred from Figure 2.21, the predictions of both models were almost identical, despite the much lower dimensionality of the lumped model.

2.4.3 A Mechanistic Two-Compartment Model for Monoclonal Antibody Disposition

If we are only interested in predicting plasma concentration-time profiles, the mechanistically lumped 4-compartment model can be further reduced, as shown in section 2.2.3. The resulting so-called minimal lumped model comprised the central compartment 'cen' and a lumped endosomal compartment 'endo' comprising all endosomal spaces. The model is schematically depicted in Figure 2.24 (top). The rate of change of the 7E3 concentration in the central compartment, C_{cen}, and the lumped endosomal compartment, C_{endo}, was given

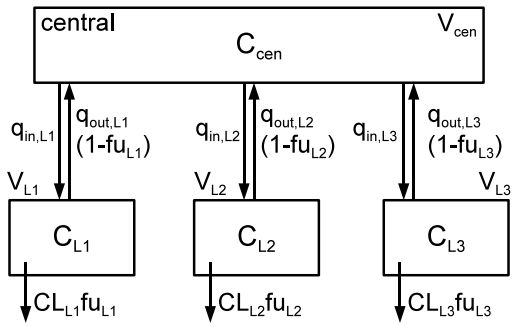

Figure 2.23: Mechanistically lumped 4-compartment model consistent with the whole-body PBPK model. Top: Model structure. The central compartment comprised the venous and arterial plasma and plasma and interstitial spaces of all organs/tissues of the whole-body PBPK model. The derivation of the lumped parameters, V_{cen}, $V_{\text{L}i}$, $q_{\text{in,L}i}$, $q_{\text{out,L}i}$, $\text{fu}_{\text{L}i}$, $\text{CL}_{\text{L}i}$ with $i = 1, 2, 3$ is given in eqs. (2.115), (2.116) and (2.119)-(2.122). Bottom: Parameters values of the lumped model.

	V mL	q_{in} mL/d	q_{out} mL/d	fu	CL mL/d
cen	4.785				
L1	0.075	2.72	0.22	≈ 0	4.54e-3
L2	0.015	1.50	0.04	0.84	0.88e-3
L3	0.008	1.01	0.02	0.95	0.46e-3

by

$$V_{\text{cen}} \frac{\text{d}}{\text{dt}} C_{\text{cen}} = q_{\text{out}} \cdot (1 - \text{fu}_{\text{endo}}) \cdot C_{\text{endo}} - q_{\text{in}} \cdot C_{\text{cen}} \tag{2.128}$$

$$V_{\text{endo}} \frac{\text{d}}{\text{dt}} C_{\text{endo}} = q_{\text{in}} \cdot C_{\text{cen}} - q_{\text{out}} \cdot (1 - \text{fu}_{\text{endo}}) \cdot C_{\text{endo}} - \text{CL}_{\text{tot}} \cdot \text{fu}_{\text{endo}} \cdot C_{\text{endo}}, \tag{2.129}$$

where V_{cen} and V_{endo} denote the lumped volumes of the central and the endosomal compartment, respectively, and q_{in} and q_{out} describe the volume flow into and out of the lumped endosomal compartment, respectively. The fraction unbound in the lumped endosomal compartment is denoted by fu_{endo}, and the total endosomal clearance is denoted by CL_{tot}. All parameters were derived according to eqs. (2.116)-(2.122). The resulting numerical values of all parameters are given in Figure 2.24 (bottom).

In [113], an empirical model (with some mechanistic elements) accounting for 7E3 and endogenous IgG disposition in mice is presented. For each molecular species, 7E3 and endogenous IgG, the model comprised two compartments, the central compartment and a peripheral compartment that represents the total endosomal space in the body. It was assumed that 7E3 and endogenous IgG are internalized from the central into the peripheral compartment where they competitively bind to FcRn. The unbound 7E3 and endogenous IgG species were subject to degradation whereas the bound species was recycled into the central compartment [113]. The ODEs describing the model and the corresponding parameter values are reported in [113, eqs.(1)-(2),(5)-(7), Table 1]; the simulations of the mAb data required to simulate the endogenous IgG concentrations. Consequently, the number of ODEs is increased to four.

The experimental data and the predicted plasma concentration-time profile for wild-type and FcRn-knockout mice after administration of an i.v. bolus dose of 8 mg/kg 7E3 are shown in Figure 2.25. The simulation were based on i) our generic 35-compartment PBPK model, ii) our minimal lumped 2-compartment model based on eqs. (2.128)-(2.129), and iii) the empirical 2-compartment model given in [113]. As it can be seen, all three models predicted the experimental data very well.

2.4.4 Discussion and Conclusions

In this study, we derived a mechanistic, low-dimensional compartment model of mAb pharmacokinetics for the use in drug development. While the analysis was based on the mAb

7E3 in mice, the conclusions drawn and the reduction technique presented hold under more general conditions.

For the analysis of pre-clinical or clinical data of mAb studies, empirical 1- or 2-compartment models are used as opposed to detailed PBPK models [101]. While there is a long history on compartmental modeling for small molecule drugs, there is no standard for the development of low-dimensional compartment models for biologics such as mAbs. Consequently, currently used empirical compartment models are diverse in structure and interpretation. We used the lumping approach developed in section 2.2.1 to reduce the detailed PBPK model to show which type of low-dimensional compartment model is consistent with the knowledge of physiological and molecular processes present in the mechanistic PBPK model.

Based on our lumping approach, we reduced the 35-compartment PBPK model to a two-compartment minimal lumped model and successfully applied it to describe the experimental plasma concentrations of the mAb 7E3 in mice. The structure and the parameters of the low-dimensional compartment model retain a physiological and mechanistic interpretation. Interestingly, except for the empirical model presented in [113], none of the other low-dimensional compartment models explicitly considers a compartment that can easily be identified with the endosomal space [105, 107]. If a linear clearance is present, it is exclusively considered in the central compartment. In contrast to the mice model considered herein, however, most models explicitly consider target-mediated binding processes, most often in a peripheral compartment. We expect that the presence of a target receptor, e.g., in the interstitial space has some impact on whether or not to lump the plasma and the interstitial space, but that this has negligible impact on whether or not to lump the endosomal space. The presented lumping approach can be used to illuminate this problem and to analyze whether low-dimensional compartment models explicitly considering plasma, endosomal and interstitial space are more appropriate to study the pharmacokinetics of mAb in the presence of its target. Research in this direction is currently ongoing.

The derivation of the mechanistically lumped and minimal lumped compartment models gives also further insight on the feasibility of parameter identification for the detailed PBPK model. In Appendix B.5.1, we derive the interstitial-to-plasma partition coefficient $K_{\mathrm{i,tis}}$ under the assumption B.44. This assumption states (see also Figure 2.19(right)) that the amount of mAb entering the interstitial space per unit time from the plasma space, $L_{\mathrm{tis}}(1-\sigma_{\mathrm{V}})\cdot C_{\mathrm{p,tis}}$, is larger than the amount of mAb entering from the endosomal space,

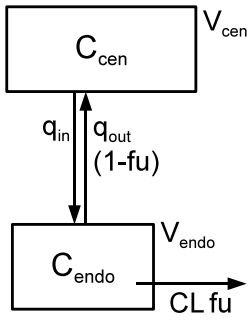

	V mL	q_{in} mL/d	q_{out} mL/d	fu	$\mathrm{CL}_{\mathrm{tot}}$ mL/d
cen	4.785				
endo	0.098	5.22	0.285	0.82	0.006

Figure 2.24: Mechanistically lumped 2-compartment model consistent with the whole-body PBPK model. Top: Model structure: The central compartment comprises all plasma and interstitial spaces of the PBPK model, whereas the peripheral (endosomal) compartment represents the total endosomal space in the body. C_{cen} and C_{endo} denote the central and lumped endosomal concentration, respectively. Bottom: Parameters values corresponding to the minimal lumped model.

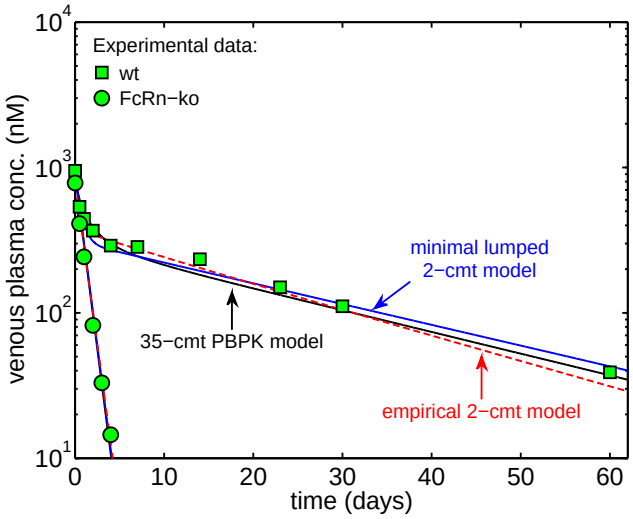

Figure 2.25: *In silico* predictions in comparison to the *in vivo* plasma data for an i.v. bolus administration of 8 mg/kg 7E3 in FcRn-knockout (FcRn-ko) and wild-type (wt) mice (experimental data extracted from [113, Figure 1]). Predictions are based on the detailed 35-compartment PBPK ('35-cmt PBPK model'), the minimal lumped 2-compartment model ('minimal lumped 2-cmt model') and the empirical compartment model ('empirical 2-cmt model'), as published in [113].

$(1-\mathrm{FR})\cdot k_{\mathrm{out}}V_{\mathrm{e,tis}}\cdot(1-\mathrm{fu}_{\mathrm{tis}})C_{\mathrm{e,tis}}$. For the mice PBPK model, the difference is between 3-8 orders of magnitude. Under this plausible assumption, the fraction of recirculated bound antibody FR cannot be reliably determined, since it does not enter at all the parameterization of the mechanistically lumped compartment model. This model, however, is by definition capable of predicting all concentration-time profiles of the detailed PBPK model (in all tissues, including the plasma, endosomal and interstitial subspaces); see Figure 2.21.

This has also implications for the identifiability of other parameters. For example, in view of recent attempts to identify physiological parameters using PBPK models, our analysis showed that we would only be able to identify the lumped parameters of the mechanistically lumped 4-compartment rather than the many parameters of the detailed PBPK model. In other words, given eqs. (2.115)-(2.122) only sums and quotients of tissue volumes, blood and lymph flows can be determined rather than the individual tissue volumes, blood and lymph flows. If only plasma data were given, we would be able to identify only the parameters of the minimal lumped model, which are even fewer.

In summary, the results presented herein contribute to a better understanding of mAb disposition. Updating the PBPK model to account for a tumor compartment and target-mediated drug disposition will provide further insight.

CHAPTER 3

Towards Mechanistic Pharmacokinetic/Pharmacodynamic Modeling: Drug Interference with the IKK-NFκB Signaling Pathway

Drug discovery and development is a challenging accomplishment that is accompanied by a high financial risk as many drug candidates that appear promising in early developmental stages prove to be ineffective or even toxic in late clinical phases [124]. Hence, it is desirable to estimate the *in vivo* efficacy and toxicity of a drug as early as possible.

Motivating example. In this chapter, we employ the systems biology approach to predict the drug exposure-response relationship for a given drug *in vivo*. We exemplify our strategy for the inflammatory biomarker NFκB that is a key regulator of the innate and adaptive immune system. An increased activity of NFκB has been observed in inflammatory diseases, neurodegenerative disorders, viral diseases, as well as cancer. Most NFκB inhibitors under development aim at decreasing the activity of IKK, the convergence point of all NFκB activating stimuli. The potency to inhibit IKK activity has been proven *in vitro* for these drugs. However, the observed *in vitro* effect has not been confirmed *in vivo* in humans since to date most of the IKK inhibitors under development are still in the pre-clinical stage.

We developed a new mathematical model to describe the regulation of IKK activity in the presence of a drug. Linking our model to a previously published model of NFκB activation [45–50] allowed us to predict the *in vivo* effect of a given drug on IKK as well as on downstream NFκB activation/inactivation (see right). We found that the desired effect of a decrease in IKK and NFκB activity is only achieved for high drug concentrations, while for low drug concentrations, we predict the opposite effect of an increase in IKK and NFκB activity.

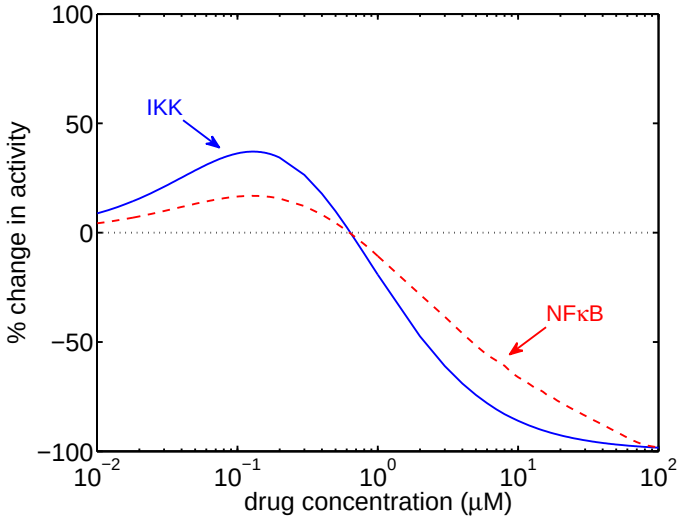

The chapter is organized as follows: In the first section, we introduce the general concepts in pharmacodynamic modeling. In the second section, we present the biological background of the IKK-NFκB signaling module and we derive our new mathematical model of the IKK activation cycle. The third section focusses on the combined PBPK-systems biology modeling approach to *a priori* predict the effect of a given drug on the IKK-NFκB signaling module.

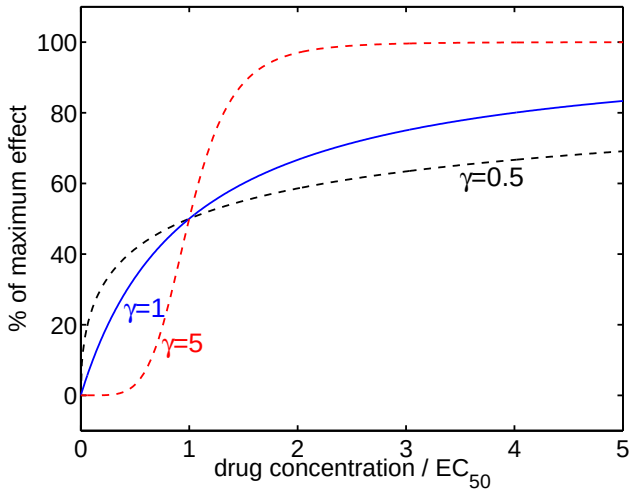

Figure 3.1: The 'Emax' model relates the drug concentration to drug effect based on the Hill equation, see eq. 3.1. EC_{50} denotes the drug concentration when the half-maximal effect is reached and the Hill coeffcient γ describes the steepness of the effect-concentration curve.

3.1 Pharmacodynamic Modeling Approaches

Pharmacodynamics (PD) aims at defining a relation between drug concentration and effect [9, 11]. In classical, i.e., empirical, PD modeling, the type of the model and model parameters are derived from experimental measurements or observations, and parameter estimation forms an integral part of model development [7, 51]. In mechanism-based PD modeling, our understanding of biochemical, physiological, physical processes involved in drug response defines the structure of the model [7, 15, 22, 24]. Model parameters may be determined by *in vitro* assays, e.g. the half maximal inhibitory drug concentration, IC_{50}, or obtained by fitting the model to an observed effect (as in the empirical approach).

Direct Response Models

The simplest PD models relate the drug effect to the drug concentration or to the dose in a linear or log-linear manner [25, 26]. However, these models are only valid when the effect is either less than 20 % (linear) or within 20-80 % (log-linear) of the maximum effect, E_{max} [22]. Moreover, with increasing drug concentrations, the effect increases unrealistically to infinity.

To deal with these drawbacks, the use of the Hill equation was introduced by Wagner in 1968 [125] with

$$\text{effect} = \frac{E_{max} \cdot C^{\gamma}}{EC_{50} + C^{\gamma}}, \tag{3.1}$$

where EC_{50} denotes the drug concentration when the half-maximal effect is reached. The Hill coefficient γ describes the steepness of the effect-concentration curve (see Figure 3.1 for illustration). To date, the 'Emax' model is commonly used for drugs that rapidly equilibrate from plasma to the site of action (i.e., the peak effect is observed simultaneously with the peak plasma concentration, C_{max}) [9]. However, a slow distribution to the target site may occur, e.g., as a result from slow tissue perfusion, permeability-rate limited distribution through membranes, etc. In order to relate the drug concentration at the target site to the drug concentration in plasma, an effect compartment can be included in the PD model [7, 10, 22, 126]. A schematic overview is given in Figure 3.2. The rate of change of drug

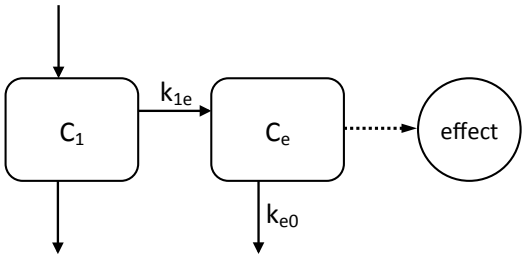

Figure 3.2: Effect compartment modeling. If drug distribution to the site of action is delayed, an effect compartment represents the mathematical link between the drug concentration in plasma, C_1, and the concentration at the target site, C_e. k_{1e} and k_{e0} denote the distribution rate constants into and out of the effect compartment. Then, the drug effect is set in relation to C_e, e.g., via the 'Emax' model.

concentration in the effect compartment, C_e, is given by

$$\frac{d}{dt}C_e = k_{1e} \cdot C_1 - k_{e0} \cdot C_e \tag{3.2}$$

with k_{1e} and k_{e0} denoting the distribution rate constants into and out of the effect compartment, and C_1 is the plasma concentration [15].

Indirect Response Models

A delay between measured drug concentration and response may not only be due to rate-limited distribution to the target site but due to the drug acting via indirect mechanisms [8, 9]. For example, the drug may inhibit or stimulate the production or degradation of an endogenous mediator of the response, or the drug may inhibit or stimulate a signaling cascade that finally mediates the observed effect [23].

The basic indirect response model describes the change of the response, R, over time by

$$\frac{d}{dt}R = k_{in}(1 \pm f(C)) - k_{out}(1 \pm f(C)) \cdot R, \tag{3.3}$$

where k_{in} and k_{out} denote the rate constants of appearance and disappearance of drug effect, respectively [22, 23]. Depending on the mechanism of action, either k_{in} or k_{out} is reduced or increased in the presence of drug. The change in drug concentration is typically given by a Hill equation of the form (cmp. eq. (3.1))

$$f(C) = \frac{E_{max} \cdot C^{\gamma}}{EC_{50} + C\gamma} \tag{3.4}$$

Here, E_{max} corresponds to the maximal inhibitory or stimulative effect of drug on R. EC_{50} retains its definition but is often replaced by IC_{50} or SC_{50} for inhibition and stimulation, respectively. Several modifications and extensions of this basic model exists, for an overview, see e.g., [15, 22, 23].

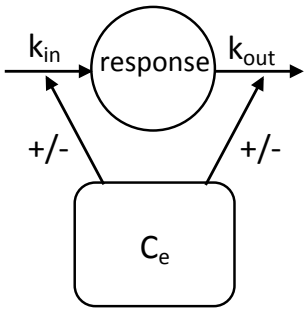

Figure 3.3: Basic indirect response model. The presence of drug may inhibit (-) or stimulate (+) the appearance (with rate constant k_{in}) or disappearance (with rate constant k_{out}) of a response.

Systems Biology Models

With ongoing progress in the elucidation of biochemical processes underlying the mechanism of action of drug effects, more detailed and complex model structures are developed [18, 27, 28]. To date, a growing number of mathematical models of large metabolic and genetic reaction networks and signaling cascades exist [127, 128]. Improved experimental or *in silico* methods enhance the determination of rate constant governing the reactions represented in these models [129–131]. This progress in the field of systems biology moves the empirical and/or mechanism-based PD modeling forward into the direction of purely mechanistic modeling.

3.2 Systems Biology Modeling of the IKK-NFκB Signaling Pathway

The transcription factor NFκB is a key regulator of the innate and adaptive immune system (reviewed in e.g., [34–36]). It promotes the expression of more than 200 genes; and the gene products are involved in the regulation of cell differentiation, proliferation, apoptosis, inflammatory reactions and the control of immunity [34, 37]. It exists in an inactive form in the cytoplasm of virtually all cell types. Upon signal onset, NFκB is translocated into the nucleus where it regulates the expression of specific genes [41, 43]. Inducible NFκB activation does not require new protein synthesis allowing for fast signal transduction. Additionally, its presence in both, the cytoplasm and the nucleus, allows for carrying messages directly to their nuclear targets.

Due to its unique role in the immune system, NFκB dysregulation is associated with inflammatory diseases, neurodegenerative disorders, viral diseases, as well as cancer [34, 38, 39]. An increased transcriptional activity of NFκB is observed in e.g., tumorigenesis, AIDS, diabetes, muscular dystrophy, rheumatoid arthritis, Alzheimer's disease and multiple sclerosis [34, 38].

In the sequel, we briefly describe the biological background of NFκB activation and inactivation with an emphasis on IKK, the key regulator of NFκB. Based on the biological model, we derive a new mathematical model of the IKK activation cycle and integrate it into a previously developed mathematical model of NFκB regulation.

3.2.1 Biology of the IKK-NFκB Signaling Module

The signaling cascade leading to the activation of NFκB is stimulated by a variety of external signals [36, 132]. Depending on the signal, the stimulation results in the activation of either the classical (canonical) or the alternative (non-canonical) pathway (reviewed in [34, 36, 42, 44]). Pro-inflammatory cytokines (e.g., IL-1 and TNF), viral or bacterial antigens and stress (e.g., reactive oxygen intermediates and UV light) activate the classical pathway [43, 44] whereas certain receptor signals (e.g., Lymphotoxin B (LTβ), B cell activating factor (BAFF) and CD40) activate the alternative one [36, 44].

The fast-acting classical pathway is largely responsible for regulating inflammation, proliferation and apoptosis, while the more slowly responding alternative one is associated with the development of lymphoid organs that ensures the mounting of an effective immune response [133]. In the following, we will focus on the classical pathway.

In resting cells, NFκB is sequestered in the cytoplasm by the interaction with its inhibitory proteins, the IκBs. The receipt of an appropriate signal leads to the phosphorylation and degradation of IκB followed by the translocation of NFκB into the nucleus (see Figure 3.4). The phosphorylation of IκB is mediated by the IκB kinase, IKK. It represents the point of convergence of most NFκB activating stimuli (reviewed in [35, 41–44]). IKK activity itself is controlled by complex processes involving multiple association and dissociation as well as several phosphorylation and dephosphorylation steps [134].

The IκBs are a family of several inhibitory proteins. The most important members involved in the classical pathway are IκBα, IκBβ and IκBϵ. All IκB proteins possess several ankyrin repeats, a structural motif that enables protein-protein interactions [39, 41]. These motifs interact with the Rel-homology domain (RHD) of NFκB which results in the masking of one or two of the nuclear localization sequences (NLS) as well as in the inhibition of DNA binding activity [39, 42, 44]. The IκB isoforms differ regarding their inhibitory functionality. IκBα can only mask one out of two NLS in the NFκB dimer. Therefore NFκB-IκBα complexes are constitutively transported into the nucleus [42, 135]. However, a nuclear export signal (NES) in IκBα precludes the accumulation of NFκB-IκBα complexes in the nucleus so

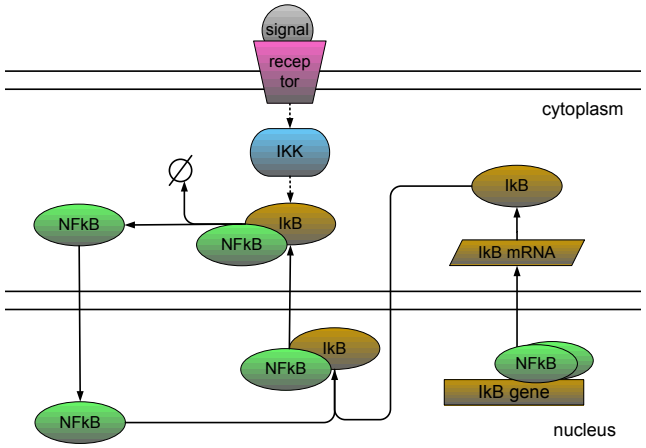

Figure 3.4: Key reactions of the NFκB pathway. In resting cells, NFκB is predominantly sequestered in the cytoplasm by the interaction with its inhibitors, IκB. Stimulation leads to phosphorylation, followed by degradation of IκB and the translocation of NFκB into the nucleus. The phosphorylation of IκB is mediated by the IκB-kinase complex, IKK. In the nucleus, NFκB triggers the expression of its inhibitors, and newly synthesized IκB exports active NFκB out of the nucleus.

that the NFκB-IκBα complex persistently shuttles between cytoplasm and nucleus [42, 136]. In contrast, IκBβ is able to mask both NLS of the NFκB dimer [42, 135]. Therefore, IκBβ sequesters NFκB in the cytoplasm. For IκBϵ, it is still not clear whether it masks one or both NLS.

IκB which is responsible for NFκB localization is regulated by the IκB kinase, IKK. It consists of two catalytic subunits (IKKα and IKKβ) as well as a regulatory subunit termed IKKγ or NEMO (NFκB essential modulator) [34, 39]. Of the two catalytic subunits, IKKβ is essential for the activation of the classical pathway [39, 137]. Each catalytic subunit possesses a kinase domain that is responsible for the phosphorylation activities by exhibiting an ATP binding site [39]. Bound ATP in turn acts as a phosphate donor for the phosphorylation of IκBs as well as its (trans-)autophosphorylation. Even if the two catalytic subunits have very similar primary structures (52 % overall identity [138]), IKKβ but not IKKα is required for the stimulation of IKK activity [139]. The regulatory subunit NEMO is a major coordinator of IKKα/β assembly [134]. The IKKα/β complex is found to be associated to a dimer or trimer of NEMO subunits [138, 140].

There exist different pathways leading to IKK activation depending on the external stimulus [41, 42]. The best known stimuli involve IL-1 and TNF. The binding of a stimulus to the IL-1 receptor causes the recrution of the adapter proteins MyD88 and Tollip [42, 141]. This is followed by the association of MyD88 with IRAK-1. Subsequently, IRAK-1 is autophosphorylated or phosphorylated by other kinases, probably IRAK-4. Phosphorylated IRAK-1 associates with TRAF6. This complex formation leads to the activation of TAK1. Active TAK1 in turn triggers the phosphorylation and therefore activation of IKK [42, 141, 142]. TNF signaling is mediated by the recruitment of a death domain containing protein TRADD to the TNF receptor. TRADD then associates with TRAF2 and RIP. TRAF2 subsequently recruits the IKK complex to the TNF receptor, where RIP activates IKK via MEKK3 [42, 142, 143].

The active IKK complex phosphorylates free and NFκB-bound IκB [49]. The phosphorylated IκB is polyubitiqinitated and degraded via the 26S proteasome (reviewed in [35, 42–44]). Free cytoplasmic NFκB is able to enter the nucleus where it accomplishes its transcriptional activity (see Figure 3.4). Nuclear NFκB promotes the transcription of several genes including the IκBα and IκBϵ gene [35, 37, 42–44, 48, 144] resulting in a negative feedback control mechanism. Newly synthesized IκBα is able to translocate into the nucleus where it binds to NFκB and transports the molecule out of the nucleus [145, 146]. This feedback provides a mechanism for achieving transient NFκB activity. However, instead of terminating its activity, NFκB remains transcriptionally active in most cell types

indicating the presence of a second mechanism responsible for persistent NFκB activation [144, 147]. It has been shown that IκBβ also reappears after its initial degradation caused by IKK activation. However, newly synthesized IκBβ occurs in an unphosphorylated state that forms stable complexes with NFκB but fails to mask the nuclear localization sequence as well as the DNA binding domain on NFκB. On the one hand, unphosphorylated IκBβ protects NFκB from association with IκBα and, on the other hand, the unphosphorylated NFκB-IκBβ complex enters the nucleus where NFκB can accomplish its transcriptional activity [147]. In human glial cells and murine embryonic fibroblasts, the reapperance of IκBβ cannot be observed [48, 144]. Therefore, IκBβ resynthesis seems to be a cell type specific mechanism. The role of IκBϵ in the termination of NFκB is less understood. It is shown that IκBϵ reappears after its initial degradation [144]. However, the induction of IκBϵ transcription in response to NFκB activation occurs with a 45 min delay in comparison to NFκB-induced IκBα transcription [48].

3.2.2 A New Systems Biology Model of the IKK Activation Cycle

A new biological model of the regulation of the IKK-NEMO complex has been recently proposed by Hayden & Ghosh [134]. In this work (jointly with A. Hoffmann and W. Huisinga), based on the biochemical findings, a new mathematical model of IKK activation and inactivation is developed taking into account the most important IKK-NEMO states.

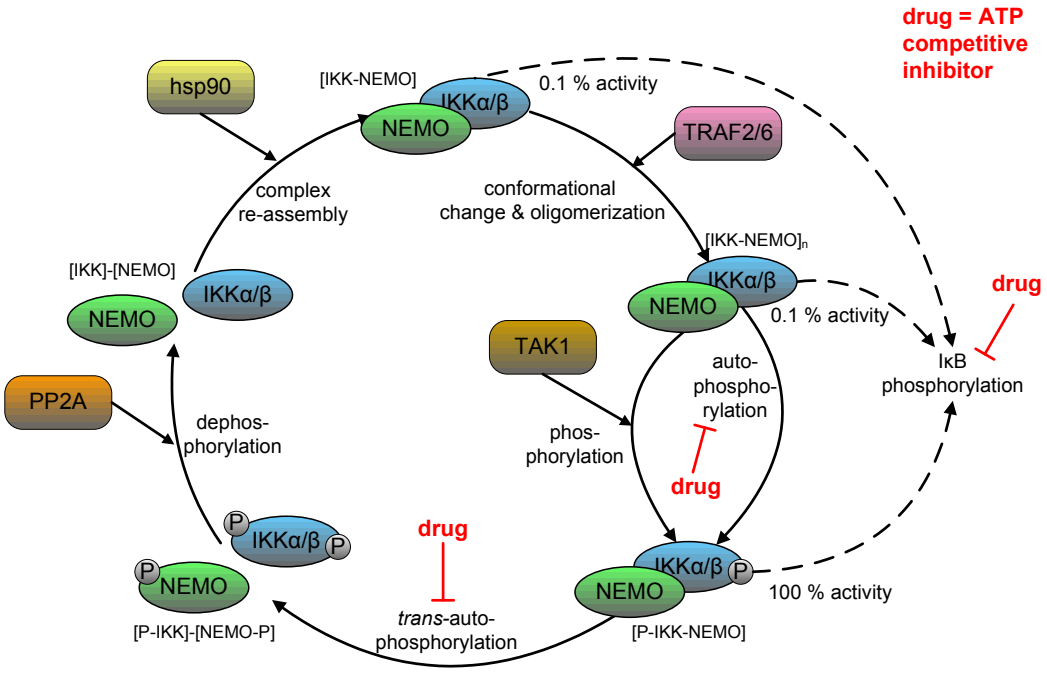

Figure 3.5: Model of the IKK activation and inactivation cycle. The IKK-NEMO complex is existent in five states. The transition from one state into the next one is activated by the modulators TRAF2/6, TAK1, PP2A and hsp90 [134]. For details, see text. In diseased cells, due to the continuous stimulation by external signals, the activity of the modulators TRAF2/6, TAK1, PP2A and hsp90 is assumed to be constantly high over time. In the model, it is assumed that a drug that competitively binds to the ATP-binding site of the catalytic subunit of IKK-NEMO, interferes with the IKK module at the level of IKK auto- and trans-autophosphorylation as well as IκB phosphorylation.

Biological model

Figure 3.5 depicts the model of IKK activation and inactivation based on the biochemical findings in [134]. As outlined in the previous section, the IKK-NEMO complex consists of two catalytic, IKKα and IKKβ, and two regulatory subunits, NEMO. In the following, we do not distinguish between the two catalytic isoforms. In resting cells, IKK-NEMO exists in a loose conformation that prevents the full activation of the complex [134]. It is proposed that this state possesses a very low kinase activity [41]. Following signal onset, NEMO binds to a RIP protein, most probably in an ubiquitin-dependent manner that is regulated by a TRAF protein (TRAF2 is activated by TNFα, and TRAF6 by IL-1 [42]). This process induces a conformational change within the complex and oligomerization of multiple IKK-NEMO units. As a consequence, the complex becomes accessible for IKK kinases (e.g., TAK1) in addition to undergoing autophosphorylation of the T loop domain [134]. In this state, the IKK-NEMO complex is fully activated and phosphorylates the IκB proteins as well as IKK's NBD (NEMO binding domain) and NEMO within the complex. The latter trans-autophosphorylation step leads to the breakup of the IKK-NEMO complex as well as dissociation of NEMO dimers. Subsequently, IKK and NEMO become accessible to phosphatases (e.g., PP2A). The dephosphorylation of IKK's T loop domain terminates its kinase activity whereas the phosphorylated NBD of IKK and NEMO prevents a reactivation of the kinase. Further dephosphorylation steps mediated by PP2A cause the complete removal of all phosphates at IKK and NEMO. Then, hsp90-mediated chaperone activity triggers the reassembly of the IKK-NEMO complex [134].

Mathematical model

Based on the biological model, there are five states of the IKK-NEMO complex to be distinguished according to their phosphorylation state as well as the assembled or separated occurrence (depicted in Figure 3.5). All of the five different states are included in the proposed mathematical model. The reaction velocities are assumed to follow mass action kinetics and the reaction rate is assumed to be proportional to the activity of the influencing signals, i.e., TRAF, TAK1, PP2A, hsp90. The corresponding system of differential equations is given by:

$$\frac{\mathrm{d}}{\mathrm{dt}}[\text{IKK-NEMO}] = v_{\text{ass}} - v_{\text{ol}} \tag{3.5}$$

$$\frac{\mathrm{d}}{\mathrm{dt}}[\text{IKK-NEMO}]_n = v_{\text{ol}} - v_{\text{TAKp}} - v_{\text{autop}} \tag{3.6}$$

$$\frac{\mathrm{d}}{\mathrm{dt}}[\text{P-IKK-NEMO}]_n = v_{\text{TAKp}} + v_{\text{autop}} - v_{\text{trp}} \tag{3.7}$$

$$\frac{\mathrm{d}}{\mathrm{dt}}[\text{P-IKK}]\text{-}[\text{NEMO-P}] = v_{\text{trp}} - v_{\text{dep}} \tag{3.8}$$

$$\frac{\mathrm{d}}{\mathrm{dt}}[\text{IKK}]\text{-}[\text{NEMO}] = v_{\text{dep}} - v_{\text{ass}} \tag{3.9}$$

with reaction velocities:

$$v_{\text{ol}} = k_{\text{ol}} \cdot \text{TRAF}(t) \cdot [\text{IKK-NEMO}] \tag{3.10}$$

$$v_{\text{TAKp}} = k_{\text{Tp}} \cdot \text{TAK}(t) \cdot [\text{IKK-NEMO}]_n \tag{3.11}$$

$$v_{\text{autop}} = k_{\text{ap}} \cdot [\text{IKK-NEMO}]_n \tag{3.12}$$

$$v_{\text{trp}} = k_{\text{tp}} \cdot [\text{P-IKK-NEMO}]_n \tag{3.13}$$

$$v_{\text{dep}} = k_{\text{dep}} \cdot \text{PP2A} \cdot [\text{P-IKK}]\text{-}[\text{NEMO-P}] \tag{3.14}$$

$$v_{\text{ass}} = k_{\text{ass}} \cdot \text{hsp90} \cdot [\text{IKK}]\text{-}[\text{NEMO}]. \tag{3.15}$$

The term v_{ol} denotes the rate of the conformational change and oligomerization of multiple IKK-NEMO complexes; v_{TAKp}, v_{autop} and v_{trp} denote the rates of the TAK1-mediated as

Table 3.1: Reaction rate constants of the IKK activation cycle. The rates have not been determined experimentally but rely on a reasonable choice (personal communication with A. Hoffmann [150]). The parameter α denotes the ratio of the autophosphorylation rate to the rate of TAK1-mediated phosphorylation. We chose $\alpha = k_{\mathrm{ap}}/k_{\mathrm{Tp}} = 1/6$.

reaction	rate (min^{-1})	ratio k_*/k_{tp}
trans-autophoshorylation	$k_{\mathrm{tp}} = \frac{\ln(2)}{5}$	1
conformational change & oligomerization (influenced by TRAF2/6)	$k_{\mathrm{ol}} = \frac{\ln(2)}{2}$	$r_{\mathrm{ol}} = 2.5$
phosphorylation of IKK bound to NEMO by TAK1	$k_{\mathrm{Tp}} = \frac{\ln(2)}{2}$	$r_{\mathrm{Tp}} = 2.5$
autophosphorylation of IKK bound to NEMO	$k_{\mathrm{ap}} = \frac{\ln(2)}{2} \cdot \alpha$	$r_{\mathrm{ap}} = 2.5 \cdot \alpha$
dephosphorylation by PP2A	$k_{\mathrm{dep}} = \frac{\ln(2)}{1}$	$r_{\mathrm{dep}} = 5.0$
complex re-assembly (influenced by hsp90)	$k_{\mathrm{ass}} = \frac{\ln(2)}{10}$	$r_{\mathrm{ass}} = 0.5$

well as auto- and trans-autophosphorylation steps, respectively, and v_{ass} denotes the IKK-NEMO reassembly (see Table 3.1 for parameter values). TRAF(t), TAK(t), PP2A, hsp90 denote the activity of the input signals.

The activity of the input signals may very depending on the state of the cell. In healthy cells, TRAF and TAK1 signals are assumed to increase after stimulation to a certain level and remain constant until they decrease again. In diseased cells, when constant cell stimulation by external signals occurs [40, 148, 149], we assume that TRAF and TAK1 are constantly active. The activity of PP2A and hsp90 is also assumed to be constant over time. The total concentration of the IKK-NEMO complex is assumed to be constant at 0.1 nM. Initially, the IKK complex is assumed to occur solely in the dephosphorylated assembled state, i.e., [IKK-NEMO]. The total concentration of NFκB is set to 0.1 nM and is assumed to remain constant [45, 50].

Combined IKK-NFκB Model

For NFκB regulation, the model previously published by Hoffmann *et al.* [45] with subsequent modifications [46–50] is adopted. The NFκB model comprises i) the synthesis of the three IκB isoforms, IκBα, IκBβ, IκBϵ, i.e., transcription (NFκB induced in case of IκBα and IκBϵ), mRNA stability, translation, and degradation, ii) the stability of free and NFκB-bound IκB, iii) the formation and breakdown of binary and tertiary NFκB-IκB complexes, iv) the phosphorylytic rate constants of IKK-NEMO containing complexes, v) the transport rates modeling nuclear import and export of free and NFκB bound IκBα and free NFκB, respectively. Figure 3.6 schematically represents all processes included in the mathematical model.

The IKK-NEMO states possess different maximal catalytic activities [41]. The rate constants of IκB phosphorylation have been determined experimentally [151, 152] (listed in Table 3.2). We assume that these rate constants correspond to the highly active $[\text{P-IKK-NEMO}]_n$ state. Low activity of the IKK-NEMO complex is represented by lowered catalytic rate constants, i.e., the catalytic rate constants of the weakly active IKK-NEMO states are assumed to be a fraction of the experimentally observed ones. In the model, this fraction is set to 0.1 %.

All active IKK-NEMO states are assumed to possess the same binding affinity to IκB and NFκB-IκB complexes. IKK-NEMO that is bound to IκB or NFκB-IκB is assumed to also undergo oligomerization ([IKK-NEMO] $\rightarrow$ $[\text{IKK-NEMO}]_n$) as well as TAK1-mediated phosphorylation or auto-phosphorylation ($[\text{IKK-NEMO}]_n \rightarrow [\text{P-IKK-NEMO}]_n$) and trans-autophosphorylation ($[\text{P-IKK-NEMO}]_n \rightarrow$ [P-IKK]-[NEMO-P]). Inactive IKK-NEMO states are assumed to be unable to associate with IκB or NFκB-IκB complexes.

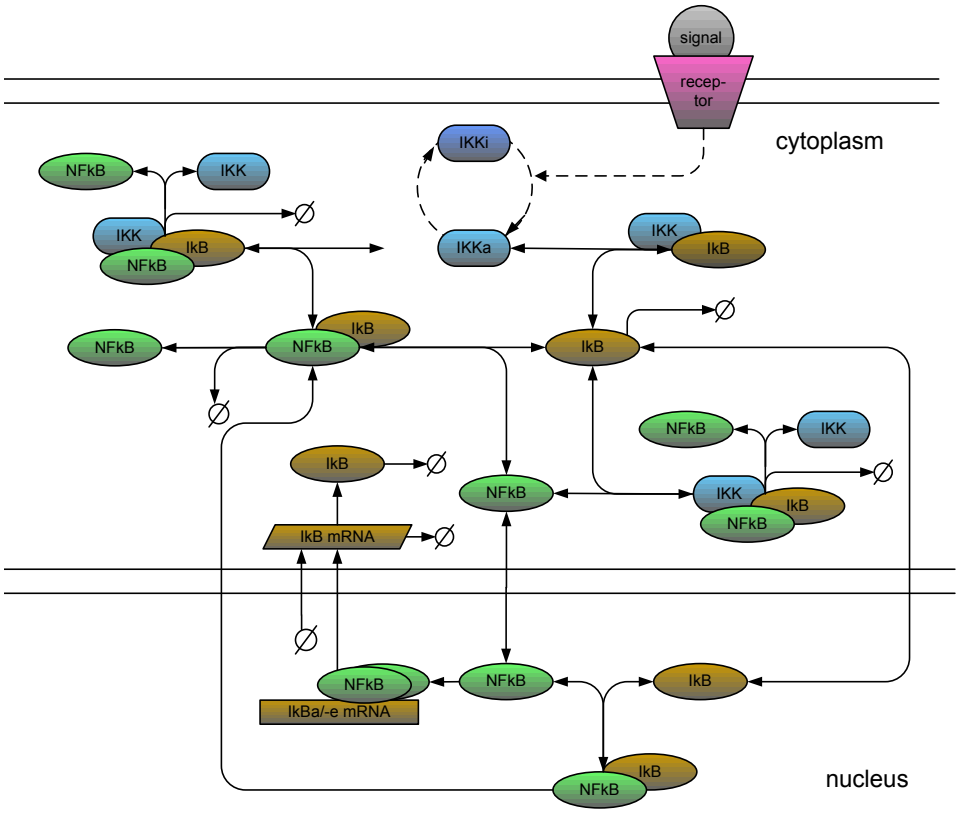

Figure 3.6: Detailed description of the NFκB pathway. In the scheme, IκB represents one of the three isoforms, i.e., IκBα, IκBβ, IκBϵ. For each isoform, the depicted reactions take place (except for the NFκB-induced expression of IκBβ). The symbol $\emptyset$ denotes the degraded IκB isoforms. All shown reactions are included in the mathematical model of the pathway. In the scheme, we simplistically denote the IKK-NEMO complex as IKK. For simplicity, the activation cycle of the IKK-NEMO complex is not shown in detail. For the detailed model, see Figure 3.5.

Total IKK activity

Analogously to enzymatic activity [153], we define the total activity of the IKK-NEMO complex as the number of IκB molecules that are phosphorylated per unit time. The IKK-NEMO complex possesses its phosphorylytic activity on the unbound as well as NFκB-bound IκB isoforms according to

$$\text{IKK} + \text{I}\kappa\text{B}* \leftrightarrow \text{IKK-I}\kappa\text{B}* \overset{k_{\text{cat},*}}{\longrightarrow} \text{IKK}, \tag{3.16}$$

Table 3.2: Catalytic rates of IKK-mediated IκB phosphorylation determined *in vitro*.

Substrate	Phosphorylatic rate (min^{-1})	Reference
IκBα	2.2	[151]
IκBβ	0.9	[151]
IκBϵ	1.32	[151]
NFκB-IκBα	11.1	[151, 152]
NFκB-IκBβ	4.5	[151, 152]
NFκB-IκBϵ	6.6	[151, 152]

where IKK denotes the IKK-NEMO complex and IκB$*$ is either an unbound or a NFκB-bound isoform of IκB, i.e., one of the following: IκBα, IκBβ, IκBϵ, NFκB-IκBα, NFκB-IκBβ, NFκB-IκBϵ. The association and dissociation of IKK-IκB$*$ complexes is assumed to follow mass action kinetics [45]. The number of IκB$*$ that are phosphorylated per unit time is given by

$$v_{\mathrm{cat},*} = k_{\mathrm{cat},*} \cdot \text{IKK-I}\kappa\text{B} * \cdot V_{\mathrm{cyto}}, \tag{3.17}$$

where $k_{\mathrm{cat},*}$ is the phosphorylytic rate constant associated with one of the unbound or NFκB-bound IκB isoforms as given in Table 3.2, and IKK-IκB$*$ denotes the concentration of the IKK-IκB$*$ complex. V_{cyto} describes the total cytoplasmic volume of the cellular space in a tissue.

We define the total activity of the IKK-NEMO complex as the number of all IκB entities that are phosphorylated per unit time, i.e.,

$$\text{total IKK activity} = \sum_{*} v_{\mathrm{cat},*}, \tag{3.18}$$

where the sum is taken over all unbound and NFκB-bound IκB isoforms.

3.3 Integrated PBPK-Systems Biology Modeling for Drugs Targeting the IKK Activation Cycle

In this section, we apply a combined PBPK-systems biology modeling approach to predict the time course of the *in vivo* effect of a given drug on IKK and downstream NFκB activation/inactivation.

3.3.1 IKK Inhibitors Known to Date and under Development

In diseased cells, the nuclear activity of NFκB is constantly elevated [34, 38, 132, 154–156]. Consequently, inhibitors of NFκB try to interfere with its nuclear activation. The most promising drug target within the NFκB activation cascade is IKK as inhibiting IKK [38–40] is thought to prevent the translocation of NFκB into the nucleus, see section 3.2.1 for a detailed description of the biological background.

Even though the mechanism of action was not known at the time of development, for a number of anti-inflammatory and immunomodulatory drugs on the market, the interference with NFκB activation at the level of IKK was proven *in vitro* later. For example, Aspirin and its metabolite sodium salicylate were identified to be competitive inhibitors of the ATP-binding site of the catalytic IKK-β subunit [157, 158]. For Ibuprofen, it was shown that the compound reduces IKK-α activity by inhibiting an activator upstream of IKK [159] and Sulindac binds to the IKK-β subunit thereby inhibiting its catalytic activity [160]. For both, Sulfasalazine and Thalidomide, the prevention of IκB phosphorylation by IKK-β and subsequent degradation was observed [161, 162]. Also, naturally occurring compounds, herbs, and vitamins possess anti-IKK activity [38, 39].

Currently, the development of selective IKK inhibitors attains a lot of attention by the pharmaceutical industry [38, 39]. Most of the drugs under development are small molecules that reversibly bind to the ATP-binding site of the kinase domain of the IKK-NEMO complex [38–40]. The *in vitro* IC_{50} of selective IKK inhibitors is in the nM-μM range [39]. An occupied ATP-binding site most likely inhibits *any* phosphorylytic activity of IKK, i.e., it may effect both, the IκB phosphorylation as well as the trans-auto- and autophosphorylation (cmp. Figure 3.5). Both autophosphorylation rates contrarily influence the level of the highly active IKK-NEMO state: While trans-autophosphorylation decreases the concentration of the highly active IKK-NEMO state, autophosphorylation facilitates the transformation of the weakly active into highly active IKK-NEMO. For this reason, it is not obvious from the *in vitro* observations, if the drugs under development produce the desired effect *in vivo*.

3.3.2 Our Integrated PBPK-Systems Biology Model

Consistent with the current efforts in the development of NFκB inhibitors, we assume that our reference compound is an ATP-competitive inhibitor of IKK. For modeling purposes, we assume that the compound is a potent inhibitor of the catalytic subunits with an IC_{50} of 30 nM. The general conclusions drawn in this study will not depend on the actual value of the IC_{50}.

The generic PBPK model for small molecule drugs depicted in Figure 2.2 is used to predict the drug concentration in each organ/tissue. Based on the unbound, intra-cellular tissue concentration, the drug concentration at the target site, i.e., the cytoplasmic space in the cells of each organ/tissue of the body, is predicted. Then, the level of cytoplasmic drug concentration determines the magnitude of drug interference at the different levels within the IKK activation cycle as well as with IκB phosphorylation (see Figure 3.5). Total IKK activity and nuclear NFκB concentrations are determined by simulating the combined IKK-NFκB model derived in the previous section, that finally allows us to predict the change in total IKK activity as well as nuclear NFκB concentration following drug administration.

Table 3.3: Summary of all data relevant for the PBPK modeling as well as the to link the PBPK and the systems biology model.

Drug-specific data		
molecular weight (g/mol)	MW	200
hepatic blood clearance (L/min)	CL_{blood}	0.7
absorption rate constant (min^{-1})	k_a	0.01
fraction absorbed	F_F	1
tissue-to-blood partition coefficients	K	predicted according to [59, 61]
fraction unbound in plasma	fu^p	0.5
blood-to-plasma ratio	B:P	1.1
drug classification		acid
pK_a		7
octanol-water partitioning	$\log P_{ow}$	3
IC_{50} (μM)		0.03
neutral fraction in plasma	fn^p	eq. (3.20)
neutral fraction in cells	fn^{cell}	eq. (3.20)
Species-specific data		
tissue volumes (L)	V	listed in Table 2.1
blood flows (L/min)	Q	listed in Table 2.1
cytoplasmic volumes (L)	V_{cyto}	70 % of cellular volume [163]
nuclear volumes (L)		14 % of V_{cyto} [164]

All parameters that are relevant for the combined PBPK-systems biology modeling are summarized in Table 3.3.

The cytoplasmic tissue concentration of the pharmacologically active, free drug, $C_{u,cyto}$, was identified with the unbound cellular tissue concentration, $C_{u,cell}$. We determined $C_{u,cell}$ from the total tissue concentration, C_{tis}, under the assumption that only the neutral unbound drug passively diffuses through the membrane [85]:

$$C_{u,cell} = \frac{fn^p}{fn^{cell}} \cdot \frac{C_{tis}}{K_{tis}^{t:up}}, \tag{3.19}$$

where $K_{tis}^{t:up}$ is the tissue-to-unbound plasma partition coefficient predicted according to [59–62] and introduced in section 2.1.2. fn^p and fn^{cell} denote the fraction of unionized drug in plasma and cellular space, respectively, and are given by the Henderson-Hasselbalch equations [165]

$$fn = \begin{cases} \frac{1}{1+10^{(pH-pK_a)}} & \text{mono-protonic acids} \\ \frac{1}{1+10^{-(pH-pK_a)}} & \text{mono-protonic bases} \\ 1 & \text{neutrals.} \end{cases} \tag{3.20}$$

The plasma pH is 7.4, and for the cellular spaces, it is 7.0 [59]. Note that the parameters for the determination of $C_{u,cell}$ are available if our generic PBPK model can be parameterized, i.e., no additional data is necessary to integrate the PBPK and the systems biology models.

The presence of an ATP-competitive inhibitor is assumed to reduce the phosphorylytic activity of the IKK-NEMO complex. In the IKK-NFκB model, there are eight rate constants describing either IKK-mediated IκB phosphorylation or trans-auto- and autophosphorylation. Since we assume that the drug blocks the ATP-binding site of the catalytic subunits of

the IKK-NEMO complex and that it binds to all ATP-binding sites with the same affinity, all eight reactions are influenced likewise. The catalytic rate constants in the presence of drug are given by

$$k_*^{\mathrm{di}}(C_{\mathrm{u,cyto}}) = \frac{k_*}{1 + C_{\mathrm{u,cyto}}/\mathrm{IC}_{50}} \tag{3.21}$$

where it is assumed that only the unbound drug in the cytoplasm, $C_{\mathrm{u,cyto}}$, is biologically active. The IC_{50} denotes the half maximal inhibitory drug concentration and k_* are the catalytic rate constants in the absence of drug with $* = \{\mathrm{ap}, \mathrm{tp}, \mathrm{I}\kappa\mathrm{B}\alpha, \mathrm{I}\kappa\mathrm{B}\beta, \mathrm{I}\kappa\mathrm{B}\epsilon, \mathrm{NF}\kappa\mathrm{B\text{-}I}\kappa\mathrm{B}\alpha, \mathrm{NF}\kappa\mathrm{B\text{-}I}\kappa\mathrm{B}\beta, \mathrm{NF}\kappa\mathrm{B\text{-}I}\kappa\mathrm{B}\epsilon\}$.

3.3.3 *In Vivo* Drug Effect on IKK and Downstream NFκB Activation

In the following, we analyze the effect of our reference drug on i) the concentration of the IKK-NEMO complex and ii) the total activity of IKK as well as downstream nuclear NFκB.

Drug interference results in an increase in highly active IKK concentration

Since the catalytic rates of the weakly active IKK states ([IKK-NEMO], $[\text{IKK-NEMO}]_n$) are assumed to be 0.1 % of the catalytic rates of the highly active $[\text{P-IKK-NEMO}]_n$, the total activity of the IKK-NEMO complex is nearly solely determined by $[\text{P-IKK-NEMO}]_n$. Thus, studying the activation of $[\text{P-IKK-NEMO}]_n$ amounts to studying the total activation of the IKK-NEMO complex.

Figure 3.7 shows the concentration of $[\text{P-IKK-NEMO}]_n$ in dependence of the drug concentration in the cytoplasm in steady state. As can be inferred from Figure 3.7, the higher the drug concentration, the higher is the concentration of highly active $[\text{P-IKK-NEMO}]_n$. The model predictions can be understood from the following equations: In steady state, the reaction rates balance each other and the overall turnover rate of the highly active $[\text{P-IKK-NEMO}]_n$ is given by

$$k_{\circlearrowleft}(C_{\mathrm{u,cyto}}) = \frac{1}{\frac{1}{k_{\mathrm{ol}}\cdot\mathrm{TRAF}} + \frac{1}{k_{\mathrm{Tp}}\cdot\mathrm{TAK}+k_{\mathrm{ap}}(C_{\mathrm{u,cyto}})} + \frac{1}{k_{\mathrm{dep}}\cdot\mathrm{PP2A}} + \frac{1}{k_{\mathrm{ass}}\cdot\mathrm{hsp90}} + \frac{1}{k_{\mathrm{tp}}(C_{\mathrm{u,cyto}})}}, \tag{3.22}$$

where the reaction rate k_{ol} refers to the conformational change and oligomerization of multiple IKK-NEMO complexes. k_{Tp} is the TAK1-mediated phosphorylation rate, and k_{dep} and k_{ass} denote the reaction rates of dephosphorylation and complex reassembly. $k_{\mathrm{ap}}(C_{\mathrm{u,cyto}})$, $k_{\mathrm{tp}}(C_{\mathrm{u,cyto}})$ are the auto- and trans-autophosphorylation rates, respectively, that depend on the free drug concentration in the cytoplasm as defined in eq. (3.21), compare Figure 3.5. Note that, in diseased cells, the signals TRAF, TAK1, PP2A, hsp90, were assumed to be constantly and highly active and, thus, are set to 1. Solving for $[\text{P-IKK-NEMO}]_n$ yields

$$[\text{P-IKK-NEMO}]_n = \frac{k_{\circlearrowleft}(C_{\mathrm{u,cyto}})}{k_{\mathrm{tp}}(C_{\mathrm{u,cyto}})}\mathrm{IKK}_{\mathrm{tot}}, \tag{3.23}$$

where $\mathrm{IKK}_{\mathrm{tot}}$ denotes the total concentration of the IKK-NEMO complex. From eq. (3.23) it follows that the ratio of $k_{\circlearrowleft}(C_{\mathrm{u,cyto}})$ to $k_{\mathrm{tp}}(C_{\mathrm{u,cyto}})$ defines the fraction of the total IKK-NEMO concentration that is present in the highly active $[\text{P-IKK-NEMO}]_n$ state. The turnover rate of $[\text{P-IKK-NEMO}]_n$, $k_{\circlearrowleft}$, is determined by both, the auto- as well as trans-autophosphorylation rates (see eq. (3.22)). While, a decreased autophosphorylation rate due to the presence of drug is counterbalanced by the TAK1-mediated phosphorylation, the decreased trans-autophosphorylation rate results in the accumulation of $[\text{P-IKK-NEMO}]_n$. This effect is the more pronounced, the lower the ratio $k_{\mathrm{ap}}/k_{\mathrm{Tp}}$. As apparent from eq. (3.22), for low ratios of $k_{\mathrm{ap}}k_{\mathrm{Tp}}$, the influence of k_{ap} is negligible and only drug interference with

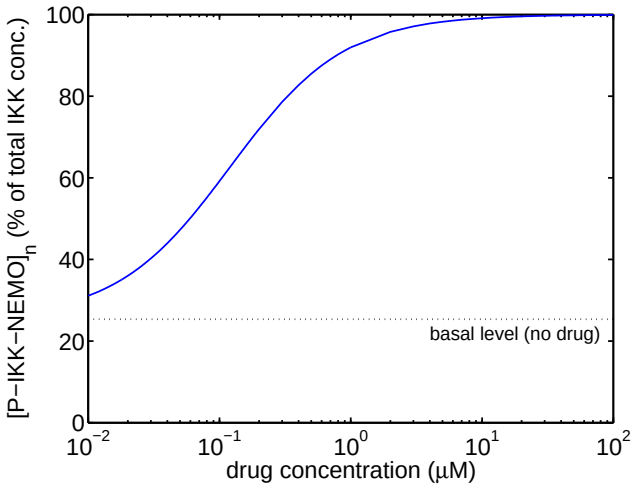

Figure 3.7: Steady state concentration of active IKK (in percent of total IKK concentration) as a function of cytoplasmic drug concentration. Inhibition of autophosphorylation is balanced by phosphorylation by TAK1. Thus, inhibition of trans-autophosphorylation results in transforming the highly active [P-IKK-NEMO]$_n$ complexes into inactive [P-IKK]-[NEMO-P]; and the [P-IKK-NEMO]$_n$ with high phosphorylytic capability accumulates.

the trans-autophosphorylation rate changes the overall turnover rate of the IKK cycle and thereby the concentration of [P-IKK-NEMO]$_n$.

Low drug concentrations result in IKK and NFκB activity increase while high drug concentrations lead to a decrease in IKK and NFκB activity

Figure 3.8 (blue solid line) shows the change of total IKK activity in dependency of cytoplasmic drug concentration compared to the level prior to drug administration in steady state. Interestingly, for low drug concentrations, IKK activity increases reaching a maximal value of 37 % change in IKK activity at a drug concentration of 0.13 μM. With further increasing drug concentrations, IKK activity continuously decreases until almost no activity is observed whereat at $C_{\mathrm{u,cyto}} \approx 0.6$ μM total IKK activity equals the activity in the absence of drug.

The total activity of the IKK-NEMO complex is defined as the number of IκB molecules that are phosphorylated per unit time, see eq. (3.18). Therefore, the total IKK activity is determined by both, the speed of IκB phosphorylation (given by the catalytic rate constants) and the concentration of IκB that is subject to phosphorylation. In the model, there are three IκB isoforms, and the free as well as the NFκB-bound IκB isoforms bind to IKK. In total, six reactions contribute to the overall IKK activity. IKK-IκB complex formation is assumed to follow mass action kinetics and an increase in [P-IKK-NEMO]$_n$ consequently results in an increase in all IKK-bound IκB isoforms. At the same time, the presence of drug inhibits IKK's catalytic activity thereby reducing the speed of phosphorylation. Thus, the total IKK activity is the sum of two opposing effects, an increased number of IκB molecules that might be phosphorylated and the reduced catalytic rate constants.

The effects of drug interference on nuclear NFκB follow the observations described for total IKK activity (see Figure 3.8, red dashed line). However, the effects are less pronounced, e.g., the maximal increase in nuclear NFκB for low drug concentrations is only half of the value observed for total IKK activity, and for high drug concentrations, nuclear NFκB decreases to a lesser extent than IKK activity.

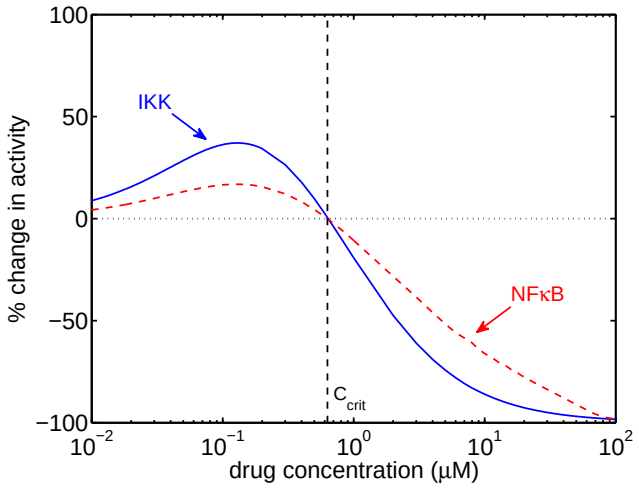

Figure 3.8: Change in total IKK activity (blue solid line) and nuclear NFκB concentration (red dashed line) in comparison to no drug interference as a function of cytoplasmic drug concentration in steady state. For low drug concentrations $< C_{\text{crit}}$, IKK activity is increased whereas for higher drug concentrations $> C_{\text{crit}}$, IKK activity decreases. Plotted values correspond to steady state.

3.3.4 Tissue-Specific Time Course of Drug Effect

The generic PBPK model for small molecule drugs introduced in section 2.1.2 was used to predict the cytoplasmic drug concentration in each organ/tissue of the PBPK model. The time course of drug effect on IKK and NFκB activation/inactivation is exemplary studied in bone cells and gut cells that possess different kinetics. While distribution into bone cells is slow ($t_{\max} \approx 5$ h), we observe a fast initial increase in drug concentration in gut cells ($t_{\max} \approx 1$ h) accompanied with a higher $C_{\max}$. Figure 3.9(upper panel) shows the PBPK modeling results following a p.o. administration of a low (100 mg) and a high dose (1 g) of the reference drug.

Figure 3.9 (middle panel) depicts the percentaged change in total IKK activity following drug administration. For the low dose (blue lines), the concentration in bone as well as in gut cells do not exceed $C_{\text{crit}} = 0.6$ μM that marks the threshold of turning the IKK activity increase into a decrease (compare Figure 3.8). As a consequence, total IKK activity is permanently increased above the basal level (no drug treatment). The same holds true for nuclear NFκB (Figure 3.9, lower panel).

For the high dose, cytoplasmic drug concentrations exceed $C_{\text{crit}} = 0.6$ μM so that an inhibition of IKK activity is to be expected. In bone cells, the drug concentration increases slowly to $C_{\max} = 1.1$ μM. Due to the initially low drug concentration, total IKK activity increases initially. see Figure 3.9. However, with further increasing drug concentrations, total IKK activity decreases under the basal level. A maximal inhibition of total IKK activity is observed when the drug reaches $C_{\max}$. For the gut cells, the initial increase in IKK activity due to initially low drug concentrations is not seen. Here, drug concentration increases rapidly to $C_{\max} = 2.1$ μM $> C_{\text{crit}}$, and the IKK-NFκB system does not adapt to the changed drug concentration in time. As pointed out previously, total IKK activity is the sum of the decreased catalytic rate constants and the increased number of IκB molecules that are available for phosphorylation. While the presence of drug immediately inhibits the catalytic rates, the pool of phosphorylatable IκB molecules builds up more slowly since it is preceded by i) the increase in $[\text{P-IKK-NEMO}]_n$ and ii) the binding of IκBs to $[\text{P-IKK-NEMO}]_n$. The sudden inhibition of IκB phosphorylation and thus degradation also explains the appearing oscillations in nuclear NFκB concentration. On the one hand, NFκB is kept in the cytoplasm by its binding to IκB and, on the other hand, NFκB is exported out of the nucleus leading to a dramatically decreasing concentration of nuclear NFκB. However, since NFκB induces the expression of two out of three IκB isoforms, i.e., IκBα and IκBϵ, low nuclear NFκB results

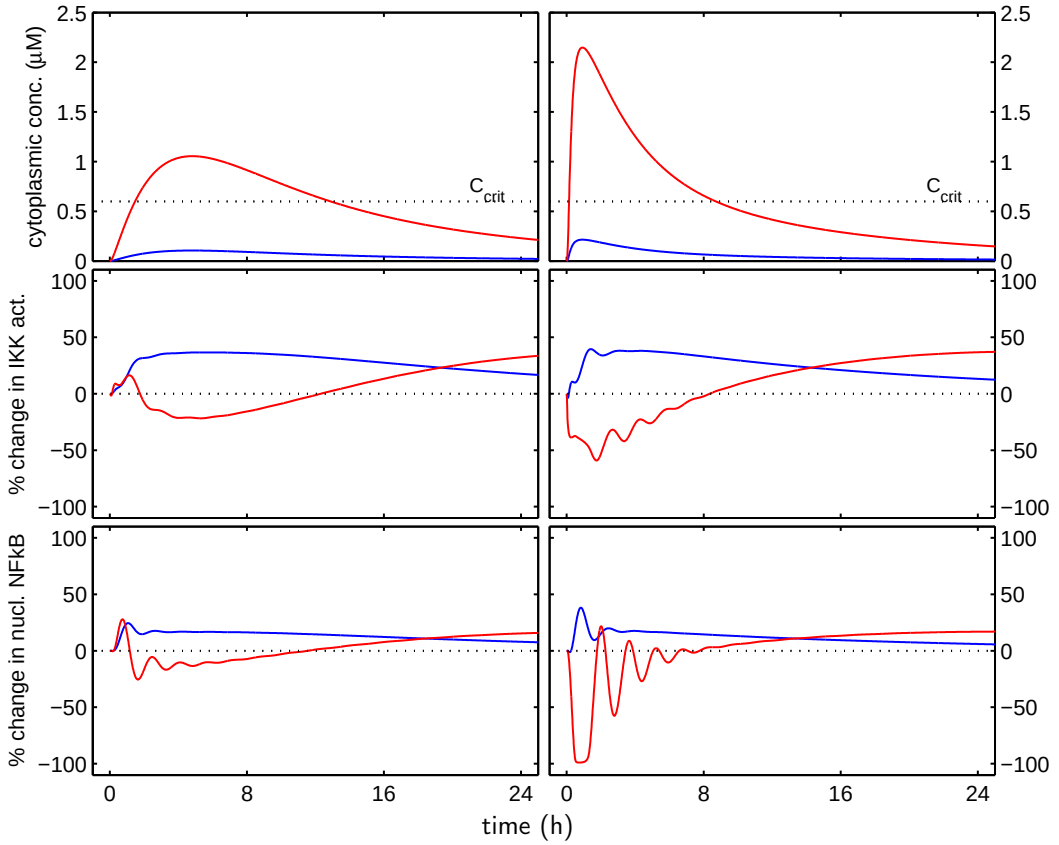

Figure 3.9: Cytoplasmic drug concentration (top panel) and its effect on IKK and downstream NFκB activation/inactivation (middle and bottom panel) exemplary for skeleton (left) and gut (right). Different colors indicate different doses; low dose (100 mg): blue, high dose (1000 mg): red.

in a reduced synthesis of new IκB. Consequently, two effects appear: First, less IκB will be available for phosphorylation by IKK, i.e., total IKK activity will decrease, and second, less IκB will be available to keep NFκB in the cytoplasm, i.e., NFκB will accumulate again in the nucleus.

At time points greater than $t_{\max}$, the decline in drug concentration results in an increasing total IKK activity. As soon as the drug concentration reaches $C_{\text{crit}} = 0.6\ \mu$M, total IKK activity and nuclear NFκB are equal to their basal levels. Here, drug decrease is as slow as the IKK-NFκB system needs time to adapt to the changed drug concentration.

3.3.5 Discussion and Conclusions

Exemplified for the IKK-NFκB pathway, the present study illustrated the utility of combining PBPK modeling and systems biology modeling to predict the effect of a drug at its target site(s) *in vivo*. While the current analysis was based on a fictive ATP-competitive inhibitor (due to the unavailability of all relevant PK data of selective IKK inhibitors under development), the conclusions drawn in this study are applicable to the compounds under development.

IKK inhibitors aim at reducing the activity of the transcription factor NFκB by inhibiting the phosphorylytic ability of IKK. However, the modeling results have shown that the effect of an ATP-competitive drug may be opposed to the expected response of the IKK-NFκB system, i.e., inhibiting IKK's phosphorylytic ability may increase the overall IKK

activity instead of decreasing it (cmp. Figure 3.8 and 3.9). For low drug concentrations, the number of phosphorylatable IκB molecules superimposes the decrease of the phosphorylytic rate constants; and IKK activation rather than inactivation is observed. Also, transient effects appear, as the response of the IKK-NFκB system is delayed if drug concentration changes rapidly. Consequently, IKK-NFκB response is depending on both, the level and the shape of the time course of drug concentration, and knowledge of this for all organs/tissues is indispensable to minimize adverse events. Here, PBPK modeling helps predicting unmeasurable drug concentrations.

The model of IKK activation and inactivation relies on two kinds of parameter sets, to wit the reaction rate constants and the activity levels of the signals TRAF, TAK1, PP2A and hsp90 (see Figure 3.5). The reaction rate constants were set to reasonable values [150]. A lower ratio of the TAK1-mediated IKK phosphorylation to the autophosphorylation rate, $k_{\mathrm{Tp}}/k_{\mathrm{ap}}$, would result in a less pronounced accumulation of highly active IKK so that less IκB molecules would be available for phosphorylation and degradation. Consequently, total IKK activity would be lowered. Besides this effect, different choices of parameter values could influence the speed of turnover of the highly active IKK (cmp. eq. (3.22)), but are not expected to compromise the general conclusions drawn in this study. For diseased cells, the signals TRAF, TAK1, PP2A, and hsp90 are assumed to be constantly active due to the permanent excitation of the cell by external stimuli (e.g., interleukins, tumor necrosis factors). The model can easily be adapted to account for healthy cells, e.g., by including an activation/inactivation profile for the input signals following appearance of an external stimuli.

In the pre-clinical or clinical phases of drug development, time series measurements of drug concentration in plasma are collected [8–10, 12]. Opposed to detailed PBPK models, empirical, low-dimensional compartment models are commonly used to describe the *in vivo* data [14]. The empirical PK model is then combined with a PD model to describe and predict the effect of the drug over time [7]. In the empirical approach, the drug concentration in plasma is often used as a surrogate for the drug concentration at the target site [7, 22, 23]. However, depending on the location of the target, distribution to the site of action might be delayed, e.g., due to perfusion-limited tissue distribution, permeability-limited distribution into cellular spaces etc. To account for the different kinetics at the target compared to in plasma, including an effect compartment allows for predicting the drug concentration at the site of action. In the present example of NFκB regulation, the response strongly depended on the drug kinetics in the cytoplasm which may vary tremendously between different cell types for a given drug. Consequently, to correctly describe the PD of the drug, one would need as many effect compartments as the number of organs/tissues exhibiting a different kinetic behavior. An approach to detect the 'kinetic diversity' was proposed in section 2.2.1 by normalizing the concentration-time profiles at the target site (analogously to eq. (2.27) and exploiting eq. (3.19)) according to

$$\text{Normalized concentration} = \frac{K_{\mathrm{tis}}^{\mathrm{t:up}}(\mathrm{fn}^{\mathrm{cell}}/\mathrm{fn}^{\mathrm{p}}) \cdot C_{\mathrm{u,cyto}}}{K_{\mathrm{tis}}(1-\mathrm{E}_{\mathrm{tis}})}. \tag{3.24}$$

As can be seen in Figure 3.10, there are five tissues possessing kinetics different from the one observed in blood: adipose, skeleton, muscle, skin due to perfusion rate-limited distribution and liver due to the p.o. dosing. For these organs/tissues, an effect compartment would have to be included in the combined PK/PD model to correctly predict the effect of the drug. In section 2.2.6, we analyzed the kinetic diversity of concentration-time profiles for a set of 25 drugs grouped according to their alkalinity/acidity. We found that for acids with a low fraction unbound in plasma the normalized concentration-time profiles in all tissues of the PBPK model were similar. Thus, for an ATP-competitive inhibitor of IKK activity that is an acidic drug with a low fraction unbound in plasma, we expect that it is not necessary to include an effect compartment to link the PK and the PD model.

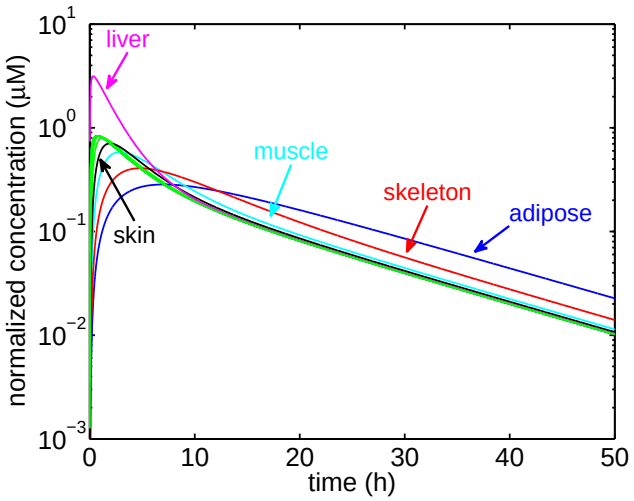

Figure 3.10: Normalized cytoplasmic concentration of each organ/tissue considered in the PBPK model. The concentration time profiles were normalized according to eq. (3.24). We identify five groups of organs/tissues with kinetics at the target site different from the one in the venous blood. In a classical modeling approach, the five groups could define the additional effect compartments in order to correctly predict the drug effect in each organ/tissue.

The importance and prospects of the systems biology approach in drug discovery and development have been highlighted in the past years. Applications comprise the identification of new drug targets, definition of reliable biomarkers, prediction of the efficacy as well as toxicity of a drug, prediction of drug-drug interactions, etc., e.g., see [18, 28, 166–168]. Also regulatory authorities, in particular the U.S. Food and Drug Administration (FDA), approves systems biology modeling as a promising tool to support drug development with an emphasis on drug safety [169, 170]. Altogether, combining PBPK and systems biology modeling allows for predicting the *in vivo* effect of a drug at developmental stages as early as the lead optimization stage. Efforts in this direction go as far as the development of automated methods to combine PBPK models and complex models of biological systems [171]. The presented study on drug interference with the IKK-NFκB signaling module demonstrates this approach towards mechanistic PK/PD modeling.

CHAPTER 4

Summary and Conclusions

Pharmacokinetic and pharmacodynamic modeling forms an integral part of various stages in drug discovery, preclinical as well as clinical drug development [8, 10]. Empirical compartment models as well as mechanistic, physiology-based pharmacokinetic (PBPK) models are frequently employed to asses the pharmacokinetics of new compounds [6, 8–10, 14]. PBPK modeling is prevalently used in drug discovery and preclinical development, e.g., to support the selection of promising drug candidates and for extrapolation from animal to human [14]. In later stage clinical development, empirical modeling is routinely used to analyze clinical trial data, e.g, as part of a population analysis to identify covariates that explain potentially observed variability in drug concentration-time profiles [8, 10]. Even though PBPK models would be applicable in late clinical development, empirical models are favored over PBPK models due to their lower complexity and for historical reasons. However, the mechanistic knowledge present in a PBPK model developed in earlier stages is likely to support a more rational model selection in the empirical approach and, thus, a methodology to link empirical compartment and mechanistic PBPK modeling is desirable. Current attempts in this direction by lumping of PBPK models exist [29–32], but do not provide a rational justification for reducing the dimensionality of PBPK models to as few as one or two compartments, as typically used in classical compartmental modeling.

In this thesis, we address this problem by developing a new lumping approach to mechanistically derive low-dimensional compartment models. The new approach, for the first time, justifies a lumping of whole-body PBPK models to one- or two-compartment models that are comparable to empirical compartment models while retaining a physiological interpretation.

The new lumping approach is likely to support empirical pharmacokinetic modeling in various ways. For example, it provides a rationale to extrapolate between species as well as from adults to children, male to female, etc. This is made possible, since the parameters of the mechanistically lumped model can now be related to organ volumes, blood flow rates and drug specific *in silico* or *in vitro* characteristics. Moreover, the lumped model may serve as a structural model within a population analysis of clinical trials. The lumped parameters may provide initial estimates for the mean population parameters in the classical parameter estimation process, thereby addressing the problem of finding appropriate initial values [99]. We demonstrate the applicability of our new lumping approach in the analysis of pre-clinical data on monoclonal antibody disposition as well as to derive a mechanistic approach to covariate modeling in population analysis.

While there is a long history on compartmental modeling for small molecule drugs, there is no standard for the development of low-dimensional compartment models for biologics such as monoclonal antibodies (mAbs). Consequently, currently used empirical compartment models are diverse in structure and interpretation. By extending our lumping approach to reduce a detailed PBPK model for mAb disposition, when the target is not expressed, we were able to reveal which type of low-dimensional compartment model is consistent with the knowledge of physiological and molecular processes present in the mechanistic PBPK model. Hence, we were able to provide a rational framework to guide empirical model development

for the analysis of mAb data.

A major challenge in population pharmacokinetics is the identification of covariates that explain the observed variability in drug concentration-time profiles in a population [99]. Empirically identified covariates are a descriptive explanation of the observed variability in a studied population with no clear physiological interpretation [172]. Thus, it is difficult to predict the variability in populations for which no direct measurements are available, e.g., in children, and it remains a major drawback of this method. In order to provide a physiology-based rationale towards predictive population pharmacokinetics it is necessary to define mechanistic covariates. In contrast to empirical covariates, they describe variability as a function of known physiological or biochemical phenomen(s) [172].

In this thesis, we provide a framework that allows to derive low-dimensional compartment models with mechanistic covariates. Our approach is based on lumping of PBPK models that incorporate mechanistic knowledge about the variability present in physiological characteristics, i.e., organ volumes and blood flow rates. The individual physiological data is derived from a reference set of physiological data via scaling factors that account for additional patient characteristics, e.g., body weight, body height, etc. The lumping of the PBPK model transforms the physiological scaling factors into mechanistic covariates in the low-dimensional compartment models. These mechanistic covariates can easily be integrated into any population analysis to explain and predict the variability due to differences in tissue volumes and blood flow rates.

In addition to contributions in pharmacokinetic modeling, this thesis also addresses the field of mechanistic pharmacodynamic modeling. In pharmacodynamics, model development is, so far, almost always empirical even though many models contain mechanistic elements [15, 22]. An emerging discipline that aims at describing the complexity of molecular processes as part of metabolic or genetic reaction networks and signaling pathways at the cell level is systems biology. The level of detail present in system biology models facilitates the integration of the mechanism of action of a drug, and hence, to predict the drug effect on the *in vivo* system.

The integration of PBPK and systems biology modeling allows for i) predicting the time course of drug concentration at the target site(s), and ii) relating the target site drug concentration to the drug effect. This finally allows for predicting the time course of drug effect that is the major prerequisite in order to determine the optimal dose for achieving a desired effect. Even though theoretical methods to couple PBPK and systems biology models exist [171], the integrated PBPK-systems biology approach is only rarely employed in the context of pharmacokinetic/pharmacodynamic modeling.

In this thesis, we illustrated the combined PBPK-systems biology modeling approach for drugs targeting the inflammatory biomarker NFκB. Currently, the development of inhibitors of IKK, the key regulator of NFκB, attains a lot of attention by the pharmaceutical industry. However, most of the IKK inhibitors under development are still in the pre-clinical stage and, thus, no data on the drug effect in humans is available. In order to predict the *in vivo* potency, we developed a new systems biology model to capture the dynamics of activation and inactivation of IKK and linked it to a previously developed systems biology model of NFκB activation. For a given drug, integrating the PBPK and systems biology models makes it possible to predict the tissue-specific time course of drug response *in vivo*.

In conclusion, the work presented in this thesis contributes to the wide and arising field of mechanistic pharmacokinetic and pharmacodynamic modeling, on the one hand, by providing a new methodology to link classical compartmental pharmacokinetic and physiology-based pharmacokinetic modeling, and, on the other hand, by illustrating the utilization of the systems biology approach in the context of mechanistic pharmacodynamic modeling.

APPENDIX A

Modeling and Simulation

A.1 Software

We used MATLAB R2009a for modeling and simulation (ode15s solver with default options). Model fitting was performed using the MATLAB optimization toolbox, version 4.2, and the predefined function 'lsqcurvefit' with default options.

A.2 Residual Error Measurements

To compare the predicted concentration for venous plasma based on the whole-body PBPK model (C_{PBPK}) and based on a lumped compartment model (C_{Lumped}), we used the following measure of the residual error:

$$\|\mathrm{C}_{\mathrm{PBPK}} - \mathrm{C}_{\mathrm{Lumped}}\|_{\mathrm{PBPK}} = \frac{\int_0^T |C_{\mathrm{PBPK}}(t) - C_{\mathrm{Lumped}}(t)| \, \mathrm{d}t}{\int_0^T C_{\mathrm{PBPK}}(t) \, \mathrm{d}t}, \tag{A.1}$$

where T denotes the simulation end time. The denominator of the above measure is identical to the well-known area under the concentration-time curve AUC_{0-T}, so we measured the deviation between predictions relative to the AUC_{0-T} as predicted by the PBPK model.

A.3 Algorithm for Creating a Virtual Population

We generated a virtual population based on the anthropometric data body height and body mass index. Since these two parameters are strongly correlated, we propose the following approach to generate a realistic sampling:

1. Sample a value for the body height from a normal distribution

$$\mathrm{BH} \sim \mathcal{N}(\mu_{\mathrm{BH}}, \sigma^2_{\mathrm{BH}}), \tag{A.2}$$

   with mean μ_{BH} and standard deviation σ_{BH}.

2. Sample a value for the body mass index from a lognormal distribution

$$\mathrm{BMI} \sim \log \mathcal{N}(\mu_{\mathrm{BMI}}, \sigma^2_{\mathrm{BMI}}), \tag{A.3}$$

   The parameters μ_{BMI} and σ^2_{BMI} are the parameters of the underlying normal distribution: $\mathrm{BMI} = \exp(\mathrm{BMI}_{\mathcal{N}})$ with $\mathrm{BMI}_{\mathcal{N}} \sim \mathcal{N}(\mu_{\mathrm{BMI}}, \sigma^2_{\mathrm{BMI}})$; The mean μ_{BMI} and standard deviation σ_{BMI} are given by

$$\mu_{\mathrm{BMI}} = \log\left(\frac{\mu^2_{\mathrm{BMI}}}{\sqrt{\mu^2_{\mathrm{BMI}} + \sigma^2_{\mathrm{BMI}}}}\right) \tag{A.4}$$

and

$$\sigma^2_{\mathrm{BMI}} = \sqrt{\log\left(\frac{\sigma^2_{\mathrm{BMI}}}{\mu^2_{\mathrm{BMI}}} + 1\right)}. \tag{A.5}$$

3. Finally, determine body weight by

$$\mathrm{BW} = \mathrm{BH}^2 \cdot \mathrm{BMI}. \tag{A.6}$$

The above procedure implies that the variance in the body weight regarding a fixed body height is increasing with the body height, which is what we would expect intuitively.

A.4 Determination of Pharmacokinetic Parameters

Pharmacokinetic characteristics were determined by analyzing the venous blood or plasma concentration using a non-compartmental analysis approach [8, 9]. The area under the concentration time curve from zero to the simulation end time, AUC(0-t_{end}), was calculated according to the trapezoidal rule. The area under the concentration time curve from zero to infinity, AUC(0- inf), was given by

$$\mathrm{AUC}(0\text{- inf}) = \mathrm{AUC}(0\text{-}t_{\mathrm{end}}) + \frac{C(t_{\mathrm{end}})}{\lambda_z}, \tag{A.7}$$

where $C(t_{\mathrm{end}})$ is the drug concentration at the simulation end time, t_{end}, and λ_z denotes the elimination rate constant that was determined by fitting a mono-exponential decay to all time points greater than $t_{\mathrm{end}}/2$. The half-life, $t_{1/2}$, was defined as

$$t_{1/2} = \frac{\ln(2)}{\lambda_z}. \tag{A.8}$$

The volume of distribution, V_{ss}, was given by

$$V_{\mathrm{ss}} = \frac{\mathrm{CL}_s}{\lambda_z}, \tag{A.9}$$

where CL_s denotes the total systemic clearance with

$$\mathrm{CL}_s = \frac{\mathrm{dose}}{\mathrm{AUC}(0\text{- inf})}. \tag{A.10}$$

APPENDIX B

Mathematical Derivations

B.1 Relation between Lumped and Original Compartment Concentrations

The relation between the concentrations of the lumped compartment and the comprised original compartments is given by eq. (2.30):

$$C_{\mathrm{L}} = \frac{1}{V_{\mathrm{L}}} \sum_{\mathrm{tis}} V_{\mathrm{tis}} C_{\mathrm{tis}}. \tag{B.1}$$

The idea is to establish a link between the concentration C_{tis} of one of the original organs/tissues and the concentration C_{L} of the associated lumped compartment. Let us arbitrarily choose one organ (named 'ref'). Using the lumping criteria, it is $C_{\mathrm{tis}}/K_{\mathrm{tis}} = C_{\mathrm{ref}}/\widehat{K}_{\mathrm{ref}}$ and, thus, $C_{\mathrm{tis}} = C_{\mathrm{ref}} K_{\mathrm{tis}}/\widehat{K}_{\mathrm{ref}}$ for all organs/tissues lumped into 'L'. In combination with the above equation for C_{L}, this yields

$$C_{\mathrm{L}} = \frac{1}{V_{\mathrm{L}}} \sum_{\mathrm{tis}} V_{\mathrm{tis}} \frac{K_{\mathrm{tis}}}{\widehat{K}_{\mathrm{ref}}} C_{\mathrm{ref}}, \tag{B.2}$$

or equivalently

$$C_{\mathrm{L}} = \frac{1}{V_{\mathrm{L}}} \sum_{\mathrm{tis}} V_{\mathrm{tis}} K_{\mathrm{tis}} \cdot \frac{C_{\mathrm{ref}}}{\widehat{K}_{\mathrm{ref}}}. \tag{B.3}$$

Using the definition of K_{L} in eq. (2.31), we obtain the desired relation:

$$\frac{C_{\mathrm{L}}}{K_{\mathrm{L}}} = \frac{C_{\mathrm{ref}}}{\widehat{K}_{\mathrm{ref}}}. \tag{B.4}$$

Since the tissue/organ 'ref' was arbitrarily chosen, the above relation holds for every original compartment 'tis' that is part of the lumped compartment 'L', being eliminating (in which case $\widehat{K}_{\mathrm{ref}} = K_{\mathrm{ref}}(1 - E_{\mathrm{ref}})$) or non-eliminating (in which case $\widehat{K}_{\mathrm{ref}} = K_{\mathrm{ref}}$).

B.2 Differential Equations of the Lumped Models

In the following, the subscript 'tis' refers to all organs of the PBPK model excluding the liver, i.e., adipose, brain, gut, heart, kidney, lung, muscle, skeleton, skin, spleen.

To derive general equations for the rate of change of the lumped concentrations, C_{L}, it is advantageous to bring the original ODEs of the generic PBPK in a different but equivalent form, where elimination is associated with the venous compartment and all other compartments have the same structural form. In the generic PBPK model (see section 2.1.2), the

liver is assumed to be the only eliminating organ with (see eq. (2.10))

$$V_{\text{liv}} \frac{\mathrm{d}}{\mathrm{dt}} C_{\text{liv}} = Q_{\text{liv}} \cdot \left(C_{\text{in,liv}} - \frac{C_{\text{liv}}}{K_{\text{liv}}} \right) - \mathrm{CL}_{\text{int}} C_{\text{liv}}. \tag{B.5}$$

Defining $\mathrm{R}_{\text{hep}} = \mathrm{CL}_{\text{int}} K_{\text{liv}} / Q_{\text{liv}}$ and noting that $1 + \mathrm{R}_{\text{hep}} = 1/(1 - \mathrm{E}_{\text{hep}})$, where E_{hep} is the hepatic extraction ratio defined in eq. (2.24), we obtain

$$V_{\text{liv}} \frac{\mathrm{d}}{\mathrm{dt}} C_{\text{liv}} = Q_{\text{liv}} \cdot \left(C_{\text{in}} - \frac{C_{\text{liv}}}{K_{\text{liv}}} \right) - Q_{\text{liv}} \mathrm{R}_{\text{hep}} \frac{C_{\text{liv}}}{K_{\text{liv}}} \tag{B.6}$$

$$= Q_{\text{liv}} \cdot \left(C_{\text{in}} - (1 + \mathrm{R}_{\text{hep}}) \frac{C_{\text{liv}}}{K_{\text{liv}}} \right) \tag{B.7}$$

$$= Q_{\text{liv}} \cdot \left(C_{\text{in}} - \frac{C_{\text{liv}}}{K_{\text{liv}}(1 - \mathrm{E}_{\text{hep}})} \right). \tag{B.8}$$

The inflowing concentration of the vein is given by (see eq. (2.17))

$$C_{\text{in}} = \frac{1}{Q_{\text{co}}} \sum_{\text{tis}} Q_{\text{tis}} \frac{C_{\text{tis}}}{K_{\text{tis}}}, \tag{B.9}$$

which can be rewritten as

$$C_{\text{in}} = \frac{1}{Q_{\text{co}}} \left(\sum_{\text{tis} \neq \text{liv}} Q_{\text{tis}} \frac{C_{\text{tis}}}{K_{\text{tis}}} + Q_{\text{liv}} (1 - \mathrm{E}_{\text{hep}}) \frac{C_{\text{liv}}}{K_{\text{liv}}(1 - \mathrm{E}_{\text{hep}})} \right) \tag{B.10}$$

$$= \frac{1}{Q_{\text{co}}} \left(\sum_{\text{tis} \neq \text{liv}} Q_{\text{tis}} \frac{C_{\text{tis}}}{K_{\text{tis}}} + Q_{\text{liv}} \frac{C_{\text{liv}}}{K_{\text{liv}}(1 - \mathrm{E}_{\text{hep}})} \right) - \frac{1}{Q_{\text{co}}} Q_{\text{liv}} \mathrm{E}_{\text{hep}} \frac{C_{\text{liv}}}{K_{\text{liv}}(1 - \mathrm{E}_{\text{hep}})}. \tag{B.11}$$

We define (see eq. 2.26)

$$\widehat{K}_{\text{tis}} = K_{\text{tis}}(1 - \mathrm{E}_{\text{tis}}), \tag{B.12}$$

where E_{tis} denotes the tissue extraction ratio. In our case, it is $\mathrm{E}_{\text{liv}} = \mathrm{E}_{\text{hep}}$ and $\mathrm{E}_{\text{tis}} = 0$ otherwise. Moreover, we formally define $\widehat{K}_{\text{ven}} = \widehat{K}_{\text{art}} = 1$. Then, we finally obtain an equivalent formulation of the whole-body PBPK model. For all organs/tissues and the arterial compartment, it is

$$V_{\text{tis}} \frac{\mathrm{d}}{\mathrm{dt}} C_{\text{tis}} = Q_{\text{tis}} \cdot \left(C_{\text{in}} - \frac{C_{\text{tis}}}{\widehat{K}_{\text{tis}}} \right), \tag{B.13}$$

while for the vein, it is

$$V_{\text{ven}} \frac{\mathrm{d}}{\mathrm{dt}} C_{\text{ven}} = Q_{\text{co}} \cdot \left(C_{\text{in}} - \frac{C_{\text{ven}}}{\widehat{K}_{\text{ven}}} \right) - \mathrm{CL}_{\text{blood}} \frac{C_{\text{liv}}}{\widehat{K}_{\text{liv}}}, \tag{B.14}$$

where we exploit $\mathrm{CL}_{\text{blood}} = Q_{\text{liv}} \mathrm{E}_{\text{hep}}$ based on eq. (2.23).

We determine the equation for the rate of change of the lumped concentration, C_{L}, by differentiating eq. (2.30), yielding:

$$V_{\mathrm{L}} \frac{\mathrm{d}}{\mathrm{dt}} C_{\mathrm{L}} = \sum_{\text{tis}} V_{\text{tis}} \frac{\mathrm{d}}{\mathrm{dt}} C_{\text{tis}}. \tag{B.15}$$

The right hand side $V_{\text{tis}} \mathrm{d}/\mathrm{dt} C_{\text{tis}}$ is defined in eqs. (B.13) and (B.14). The right hand sides contain the concentrations of the original PBPK model, C_{tis}, which can be determined using

eq. (B.4).

We obtained a very simple form of equations for the mechanistically lumped model, when spleen and gut were lumped together into the same compartment as the liver (hence they were part of the lumped 'Liv' compartment), and when lung and artery were lumped together into the same compartment as the vein (hence, they were part of the lumped 'cen' compartment). In this case, the influent concentrations will be identical for all compartments different from the central compartment. The rate of change for the concentration of the pre-lumped compartments spl-gut-liv ('sgl') and ven-lun-art ('vla') are

$$V_{\mathrm{sgl}}\frac{\mathrm{d}}{\mathrm{dt}}C_{\mathrm{sgl}} = Q_{\mathrm{liv}}\left(C_{\mathrm{art}} - \frac{C_{\mathrm{liv}}}{\widehat{K}_{\mathrm{liv}}}\right) \tag{B.16}$$

$$= Q_{\mathrm{liv}}\left(C_{\mathrm{art}} - \frac{C_{\mathrm{sgl}}}{\widehat{K}_{\mathrm{sgl}}}\right), \tag{B.17}$$

and

$$V_{\mathrm{vla}}\frac{\mathrm{d}}{\mathrm{dt}}C_{\mathrm{vla}} = Q_{\mathrm{co}}\left(C_{\mathrm{in}} - \frac{C_{\mathrm{art}}}{\widehat{K}_{\mathrm{art}}}\right) - \mathrm{CL}_{\mathrm{blood}}\frac{C_{\mathrm{liv}}}{\widehat{K}_{\mathrm{liv}}} \tag{B.18}$$

$$= Q_{\mathrm{co}}\left(C_{\mathrm{in}} - \frac{C_{\mathrm{vla}}}{\widehat{K}_{\mathrm{vla}}}\right) - \mathrm{CL}_{\mathrm{blood}}\frac{C_{\mathrm{liv}}}{\widehat{K}_{\mathrm{liv}}} \tag{B.19}$$

where C_{in} is the concentration flowing into the vein.
Now, for any lumped compartment excluding the central compartment, it is

$$V_{\mathrm{L}}\frac{\mathrm{d}}{\mathrm{dt}}C_{\mathrm{L}} = \sum_{\mathrm{tis}} V_{\mathrm{tis}}\frac{\mathrm{d}}{\mathrm{dt}}C_{\mathrm{tis}} \tag{B.20}$$

$$= \sum_{\mathrm{tis}} Q_{\mathrm{tis}}C_{\mathrm{art}} - \sum_{\mathrm{tis}} Q_{\mathrm{tis}}\frac{C_{\mathrm{tis}}}{\widehat{K}_{\mathrm{tis}}}, \tag{B.21}$$

where the sum is taken over all tissues that are lumped into 'L'. Our above assumption ensures that the inflowing concentration is the same and identical to C_{art} for all tissue/organs. Exploiting the lumping condition $C_{\mathrm{tis}}/\widehat{K}_{\mathrm{tis}} = C_{\mathrm{L}}/K_{\mathrm{L}}$ yields

$$V_{\mathrm{L}}\frac{\mathrm{d}}{\mathrm{dt}}C_{\mathrm{L}} = \left(\sum_{\mathrm{tis}} Q_{\mathrm{tis}}\right)C_{\mathrm{in}} - \left(\sum_{\mathrm{tis}} Q_{\mathrm{tis}}\right)\frac{C_{\mathrm{L}}}{K_{\mathrm{L}}}. \tag{B.22}$$

Finally, using $Q_{\mathrm{L}} = \sum_{\mathrm{tis}} Q_{\mathrm{tis}}$ and $C_{\mathrm{art}} = C_{\mathrm{cen}}/K_{\mathrm{cen}}$ results in

$$V_{\mathrm{L}}\frac{\mathrm{d}}{\mathrm{dt}}C_{\mathrm{L}} = Q_{\mathrm{L}}\left(\frac{C_{\mathrm{cen}}}{K_{\mathrm{cen}}} - \frac{C_{\mathrm{L}}}{K_{\mathrm{L}}}\right). \tag{B.23}$$

For the central compartment, we obtain analogously

$$V_{\mathrm{cen}}\frac{\mathrm{d}}{\mathrm{dt}}C_{\mathrm{cen}} = Q_{\mathrm{cen}}\left(C_{\mathrm{in}} - \frac{C_{\mathrm{cen}}}{\widehat{K}_{\mathrm{cen}}}\right) - \mathrm{CL}_{\mathrm{blood}}\frac{C_{\mathrm{Liv}}}{K_{\mathrm{Liv}}}, \tag{B.24}$$

where we exploit the fact that $C_{\mathrm{liv}}/\widehat{K}_{\mathrm{liv}} = C_{\mathrm{Liv}}/K_{\mathrm{Liv}}$.

The above equations do not take into account any dosing. Again, as in the whole-body PBPK case, the corresponding ODEs of the lumped compartments comprising vein and liver have to be amended correspondingly. For an i.v. infusion, r_{iv}, (see eq. (2.4) for the

definition), it is

$$V_{\text{cen}}\frac{\text{d}}{\text{dt}}C_{\text{cen}} = Q_{\text{cen}}\left(C_{\text{in}} - \frac{C_{\text{cen}}}{\widehat{K}_{\text{cen}}}\right) - \text{CL}_{\text{blood}}\frac{C_{\text{Liv}}}{K_{\text{Liv}}} + r_{\text{iv}}, \tag{B.25}$$

while for a p.o. administration, $r_{\text{po}(\text{F}_{\text{F}\cdot\text{G}})}$, (see eq. (2.20) for the definition), it is

$$V_{\text{Liv}}\frac{\text{d}}{\text{dt}}C_{\text{Liv}} = Q_{\text{Liv}}\left(\frac{C_{\text{cen}}}{K_{\text{cen}}} - \frac{C_{\text{Liv}}}{K_{\text{Liv}}}\right) + r_{\text{po}(\text{F}_{\text{F}\cdot\text{G}})}. \tag{B.26}$$

If 'cen' and 'Liv' are identical, i.e., if the liver is lumped into the central compartment, it is $C_{\text{cen}}/K_{\text{cen}} = C_{\text{Liv}}/K_{\text{Liv}}$ and, thus,

$$V_{\text{cen}}\frac{\text{d}}{\text{dt}}C_{\text{cen}} = Q_{\text{cen}}\left(C_{\text{in}} - \frac{C_{\text{cen}}}{\widehat{K}_{\text{cen}}}\right) - \text{CL}_{\text{blood}}\frac{C_{\text{cen}}}{K_{\text{cen}}} + r_{\text{iv,po}(\text{F})}. \tag{B.27}$$

Note that in this case, the p.o. administration model has to account for the hepatic extraction, i.e., the absorption model with $F_{\text{bio}} = (1-\text{E}_{\text{hep}})F_{\text{F}\cdot\text{G}}$ (see eq. (2.5)) is used rather then the model with $F_{\text{F}\cdot\text{G}}$ (see eq. (2.19)).

B.3 Lumping of the Permeability Rate-Limited Tissue Model

The rate of change of the vascular concentration, C_{vas}, and the tissue concentration, C_{tis}, in a permeability-rate limited tissue model are given by:

$$V_{\text{vas}}\frac{\text{d}}{\text{dt}}C_{\text{vas}} = Q_{\text{tis}}\cdot(C_{\text{in}} - C_{\text{vas}}) - \text{PS}_{\text{tis}}\left(C_{\text{vas}} - \frac{C_{\text{tis}}}{K_{\text{tis}}}\right) \tag{B.28}$$

$$V_{\text{tis}}\frac{\text{d}}{\text{dt}}C_{\text{tis}} = \text{PS}_{\text{tis}}\cdot\left(C_{\text{vas}} - \frac{C_{\text{tis}}}{K_{\text{tis}}}\right). \tag{B.29}$$

The amount of drug that can transfer from the vascular to the tissue part is limited by the maximal amount of drug, entering the tissue, i.e, $Q_{\text{tis}}C_{\text{in}}$. This has to be taken into account, when lumping the tissue space together with other compartments. The following idea is similar to the approach to determine the blood clearance from the intrinsic clearance. It is based on a quasi-steady state assumption on C_{vas} (eq.(B.28)) yielding

$$0 = Q_{\text{tis}}\cdot(C_{\text{in}} - C_{\text{vas}}) - \text{PS}_{\text{tis}}\left(C_{\text{vas}} - \frac{C_{\text{tis}}}{K_{\text{tis}}}\right) \tag{B.30}$$

or

$$C_{\text{vas}} = \frac{Q_{\text{tis}}}{\text{PS}_{\text{tis}} + Q_{\text{tis}}}C_{\text{in}} + \frac{\text{PS}_{\text{tis}}}{\text{PS}_{\text{tis}} + Q_{\text{tis}}}\cdot\frac{C_{\text{tis}}}{K_{\text{tis}}}. \tag{B.31}$$

Thus, in steady state, the vascular concentration is a weighted sum of the influent concentration, C_{in}, and the concentration leaving the tissue compartment, $C_{\text{tis}}/K_{\text{tis}}$. For permeability-rate limited organs/tissues, we would usually expect

$$\frac{Q_{\text{tis}}}{\text{PS}_{\text{tis}} + Q_{\text{tis}}} > \frac{\text{PS}_{\text{tis}}}{\text{PS}_{\text{tis}} + Q_{\text{tis}}}, \tag{B.32}$$

and as a consequence, we lump the vascular sub-compartment together with the blood compartment and approximate $C_{\text{vas}} = C_{\text{blood}}$.

Inserting eq. (B.31) into eq. (B.29) yields for the tissue concentration

$$V_{\text{tis}}\frac{\mathrm{d}}{\mathrm{dt}}C_{\text{tis}} = \text{PS}_{\text{tis}} \cdot \left(\frac{Q_{\text{tis}}C_{\text{in}} + \text{PS}_{\text{tis}}\frac{C_{\text{tis}}}{K_{\text{tis}}}}{\text{PS}_{\text{tis}} + Q_{\text{tis}}} - \frac{C_{\text{tis}}}{K_{\text{tis}}} \right) \tag{B.33}$$

and finally

$$V_{\text{tis}}\frac{\mathrm{d}}{\mathrm{dt}}C_{\text{tis}} = \frac{\text{PS}_{\text{tis}} \cdot Q_{\text{tis}}}{\text{PS}_{\text{tis}} + Q_{\text{tis}}} \cdot \left(C_{\text{in}} - \frac{C_{\text{tis}}}{K_{\text{tis}}} \right) \tag{B.34}$$

Hence, when lumping the tissue part of a permeability-rate limited tissue model, the term

$$\frac{\text{PS}_{\text{tis}} \cdot Q_{\text{tis}}}{\text{PS}_{\text{tis}} + Q_{\text{tis}}} \tag{B.35}$$

should take the role of the tissue blood flow, Q_{tis}. It is bounded by both, Q_{tis} and PS.

B.4 Automated Determination of the Number and Composition of Mechanistically Lumped Compartments

To compare the mechanistically lumped compartment models for a different drugs, we used an automated detection algorithm to determine the number of lumped compartment and its composition. The input were the normalized concentration-time profiles as predicted by the detailed whole-body PBPK model (cf. (2.27)):

$$c_{\text{tis}}(t) = \frac{C_{\text{tis}}(t)}{\widehat{K}_{\text{tis}}}. \tag{B.36}$$

We determined the similarity matrix $M = (M_{ij})$ with

$$M_{i,j} = \frac{\langle c_{\text{tis}(i)}, c_{\text{tis}(j)} \rangle}{\langle c_{\text{tis}(i)}, c_{\text{tis}(i)} \rangle}, \tag{B.37}$$

where $\langle \cdot, \cdot \rangle$ denotes the Euclidian scalar product. In our setting, if C_{tis} is given as a vector at different time points $c_{\text{tis}}(t_1), \ldots, c_{\text{tis}}(t_M)$ for some $M > 0$, then

$$\langle c_{\text{tis}(i)}, c_{\text{tis}(j)} \rangle \approx \sum_{k=1}^{M} c_{\text{tis}(i)}(t_k) \cdot c_{\text{tis}(j)}(t_k)\Delta t, \tag{B.38}$$

where we for simplicity assumed that the time points are equally spaced with distance Δt.

Next we determined the eigenvector, v, corresponding to the maximal eigenvalue of M. This eigenvector has an entry corresponding to each organ, tissue or other space of the whole-body PBPK model. We normalized the eigenvector

$$w(\text{tis}) = \frac{v(\text{tis})}{v(\text{ven})} \tag{B.39}$$

such that the normalized eigenvector satisfied $w(\text{ven}) = 1$. See Figure B.1 for the eigenvector corresponding to our reference compound Lidocaine (for sake of illustration, we ordered the entries in increasing order).

We then considered the smallest entry of w (in the example corresponding to the adipose tissue) and lumped all organs that satisfied:

$$w(\text{tis}) < w(\text{adi}) + \Delta w, \tag{B.40}$$

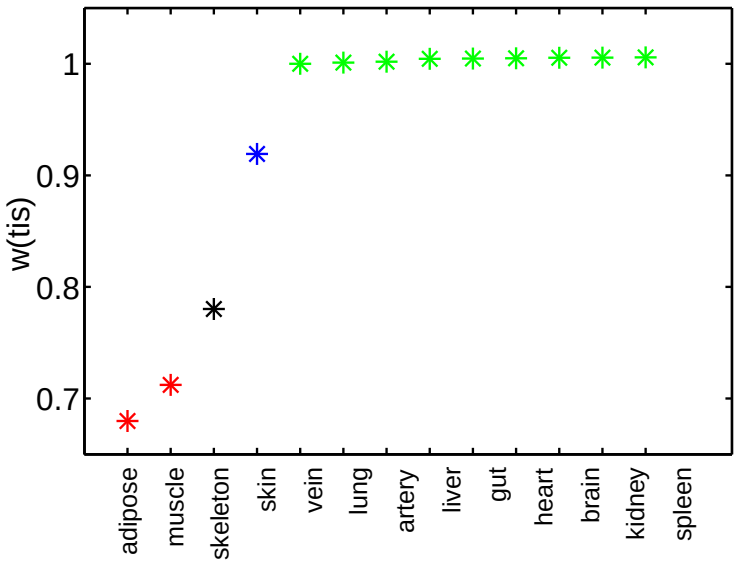

Figure B.1: Normalized eigenvector w corresponding to the maximal eigenvalue of the similarity matrix M based on the PBPK predictions of an 60 min i.v. infusion of 400 mg Lidocaine.

with $\Delta w = 0.045$. For our reference compound Lidocaine, was the muscle was the only organ/tissue to satisfy the above inequality. Hence, the muscle was lumped with the adipose tissue. We proceeded with the next tissue (skeleton in our example):

$$w(\text{tis}) < w(\text{ske}) + \Delta w. \tag{B.41}$$

In this case, there was no organ/tissue to satisfy the above inequality so that skeleton defined a single lumped compartment. We then proceeded with skin etc. The value of Δw was chosen so that the automated lumping procedure gave the same results as the manually chosen lumping for Lidocaine. The smaller the value of Δw the more similar the concentration-time profiles have to be for two organs/tissues to be lumped together.

For Theophylline, Diazepam, Flunitrazepam, Amobarbital the predicted mechanistically lumped model was not sufficient to predict all concentration-time profiles of the 13-compartment whole-body PBPK model. In this case, we manually added a lumped compartment, which resolved the problem and increased the number of compartments by 1.

B.5 Partition Coefficients and Tissue Extraction Ratios of the PBPK Model for Monoclonal Antibody Disposition

The partition coefficient, $K_{x:y}$, is defined as the steady state ratio of the concentration of x to the concentration of y:

$$K = \frac{C_{\text{x}}^{\text{ss}}}{C_{\text{y}}^{\text{ss}}}. \tag{B.42}$$

Based on this relation, we derive explicit formulas for the interstitial-to-plasma partition coefficient, $K_{\text{i,tis}}$, and the endosomal-to-plasma partition coefficient, $K_{\text{p,tis}}$.

B.5.1 Interstitial-to-Plasma Partition Coefficients

For each tissue, the rate of change of the drug concentration in the interstitial space is given by (see eq. (2.95)):

$$V_{\mathrm{i,tis}}\frac{\mathrm{d}}{\mathrm{dt}}C_{\mathrm{i,tis}} = L_{\mathrm{tis}}(1-\sigma_{\mathrm{V}})\cdot C_{\mathrm{p,tis}} - L_{\mathrm{tis}}(1-\sigma_{\mathrm{L}})\cdot C_{\mathrm{i,tis}} \\ - k_{\mathrm{in}}V_{\mathrm{i,tis}}\cdot C_{\mathrm{i,tis}} + (1-\mathrm{FR})\cdot k_{\mathrm{out}}V_{\mathrm{e,tis}}\cdot(1-\mathrm{fu}_{\mathrm{e,tis}})\cdot C_{\mathrm{e,tis}}.$$

Assuming a quasi-steady state for the interstitial concentration, we obtain

$$C_{\mathrm{i,tis}} = \frac{L_{\mathrm{tis}}(1-\sigma_{\mathrm{V}})}{L_{\mathrm{tis}}(1-\sigma_{\mathrm{L}})+k_{\mathrm{in}}V_{\mathrm{i,tis}}}\cdot C_{\mathrm{p,tis}} + \frac{(1-\mathrm{FR})\cdot k_{\mathrm{out}}V_{\mathrm{e,tis}}\cdot(1-\mathrm{fu}_{\mathrm{e,tis}})}{L_{\mathrm{tis}}(1-\sigma_{\mathrm{L}})+k_{\mathrm{in}}V_{\mathrm{i,tis}}}\cdot C_{\mathrm{e,tis}}. \quad \text{(B.43)}$$

In our PBPK model, the flux from the endosomal to interstitial space is much smaller than the flux from the plasma to interstitial space in each tissue, i.e.,

$$(1-\mathrm{FR})\cdot k_{\mathrm{out}}V_{\mathrm{e,tis}}\cdot(1-\mathrm{fu}_{\mathrm{e,tis}})\cdot C_{\mathrm{e,tis}} \ll L_{\mathrm{tis}}(1-\sigma_{\mathrm{V}})\cdot C_{\mathrm{p,tis}}. \quad \text{(B.44)}$$

For our parameterization, it is

$$\frac{(1-\mathrm{FR})\cdot k_{\mathrm{out}}V_{\mathrm{e,tis}}\cdot(1-\mathrm{fu}_{\mathrm{e,tis}})C_{\mathrm{e,tis}}}{L_{\mathrm{tis}}(1-\sigma_{\mathrm{V}})\cdot C_{\mathrm{p,tis}}} \approx [10^{-8}-10^{-3}] \quad \text{(B.45)}$$

Exploiting this observation, eq. (B.43) simplifies to

$$C_{\mathrm{i,tis}} = \frac{L_{\mathrm{tis}}(1-\sigma_{\mathrm{V}})}{L_{\mathrm{tis}}(1-\sigma_{\mathrm{L}})+k_{\mathrm{in}}V_{\mathrm{i,tis}}}\cdot C_{\mathrm{p,tis}}, \quad \text{(B.46)}$$

yielding for the interstitial-to-plasma partition coefficient:

$$K_{\mathrm{i,tis}} = \frac{L_{\mathrm{tis}}(1-\sigma_{\mathrm{V}})}{L_{\mathrm{tis}}(1-\sigma_{\mathrm{L}})+k_{\mathrm{in}}V_{\mathrm{i,tis}}}. \quad \text{(B.47)}$$

Numerical parameter values of $K_{\mathrm{i,tis}}$ based on Tables 2.6-2.7 are listed in Table 2.8.

B.5.2 Endosomal-to-Plasma Partition Coefficients

The derivation of the endosomal-to-plasma partition coefficient is based on a simplified 2-compartment organ model that consists of a pre-lumped plasma/interstitial space and the endosomal space for each tissue of the PBPK model, see Figure B.2. The pre-lumping step was motivated by the observations in Figure 2.22(left), indicating that, in each tissue, plasma and interstitial space behave kinetically similar.

Analogously to eq. (2.116), the volume of the pre-lumped plasma+interstitial space is defined as the sum of the plasma and interstitial volumes:

$$V_{\mathrm{pi,tis}} = V_{\mathrm{p,tis}} + V_{\mathrm{i,tis}}. \quad \text{(B.48)}$$

Based on the conservation of mass, the concentration in the lumped compartment $C_{\mathrm{pi,tis}}$ is defined as the volume weighted sum of the concentrations in plasma and interstitial spaces:

$$C_{\mathrm{pi,tis}} = \frac{V_{\mathrm{p,tis}}C_{\mathrm{p,tis}} + V_{\mathrm{i,tis}}C_{\mathrm{i,tis}}}{V_{\mathrm{pi,tis}}} \quad \text{(B.49)}$$

with $V_{\mathrm{pi,tis}}$ given in eq. (B.48).

Exploiting eqs. (B.47) and (B.49), we obtain the pre-lumped (plasma+interstitial)-to-plasma partition coefficient, $K_{\mathrm{pi,tis}}$, that relates the steady state concentration in the lumped

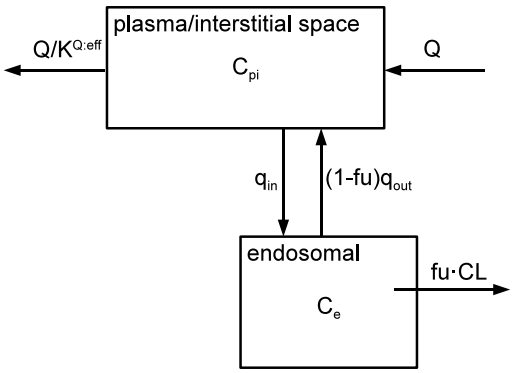

Figure B.2: Partially lumped organ model comprising a lumped plasma+interstitial (pi) compartment and an endosomal space (e). Here, $q_{\mathrm{in}} = k_{\mathrm{in}}(V_{\mathrm{p}} + V_{\mathrm{i}})$ (see eq. (B.54)) denotes the volume flow of endogenous IgG or mAb from the plasma+interstitial space into the endosomal space. $K^{\mathrm{Q:eff}} = P/((P-L)K_{\mathrm{pi}} + L(1-\sigma_{\mathrm{L}})K_{\mathrm{pi}}/K_{\mathrm{i}})$ (eq. (B.56)) relates the concentration in the lumped plasma+interstitial space to the concentration leaving the compartment via plasma and lymph flow, and K_{pi} and K_{i} are the (plasma+interstitial)-to-plasma and interstitial-to-plasma partition coefficients, respectively.

plasma+interstitial compartment to the steady state plasma concentration:

$$K_{\mathrm{pi,tis}} = \frac{C^{\mathrm{ss}}_{\mathrm{pi,tis}}}{C^{\mathrm{ss}}_{\mathrm{p,tis}}} = \frac{V_{\mathrm{p,tis}} + V_{\mathrm{i,tis}}K_{\mathrm{i,tis}}}{V_{\mathrm{pi,tis}}}. \tag{B.50}$$

The ODE describing the rate of change of the concentration in the pre-lumped plasma+interstitial space is obtained by adding the original ODEs of plasma and interstitial spaces (eqs. (2.93) and (2.95)):

$$V_{\mathrm{pi,tis}}\frac{\mathrm{d}}{\mathrm{dt}}C_{\mathrm{pi,tis}} = V_{\mathrm{p,tis}}\frac{\mathrm{d}}{\mathrm{dt}}C_{\mathrm{p,tis}} + V_{\mathrm{i,tis}}\frac{\mathrm{d}}{\mathrm{dt}}C_{\mathrm{i,tis}}. \tag{B.51}$$

Exploiting the defining equations for $C_{\mathrm{pi,tis}}$ and $K_{\mathrm{i,tis}}$ (eqs. (B.49) and (B.47)), yields

$$V_{\mathrm{pi,tis}}\frac{\mathrm{d}}{\mathrm{dt}}C_{\mathrm{pi,tis}} = P_{\mathrm{tis}} \cdot \left(C_{\mathrm{in,tis}} - \frac{C_{\mathrm{pi,tis}}}{K^{\mathrm{Q:eff}}_{\mathrm{tis}}}\right) - q_{\mathrm{in,tis}} \cdot C_{\mathrm{pi,tis}} + q_{\mathrm{out,tis}} \cdot (1 - \mathrm{fu}_{\mathrm{e,tis}}) \cdot C_{\mathrm{e,tis}} \tag{B.52}$$

$$V_{\mathrm{e,tis}}\frac{\mathrm{d}}{\mathrm{dt}}C_{\mathrm{e,tis}} = q_{\mathrm{in,tis}} \cdot C_{\mathrm{pi,tis}} - q_{\mathrm{out,tis}} \cdot (1 - \mathrm{fu}_{\mathrm{e,tis}}) \cdot C_{\mathrm{e,tis}} - \mathrm{CL}_{\mathrm{e,tis}} \cdot \mathrm{fu}_{\mathrm{e,tis}} \cdot C_{\mathrm{e,tis}}, \tag{B.53}$$

where $C_{\mathrm{in,tis}}$ denotes the inflowing tissue concentration, see eqs. (2.96), (2.100), and (2.98). The volume flows into and out of the endosomal space, $q_{\mathrm{in,tis}}$ and $q_{\mathrm{out,tis}}$, respectively, (compare Figure B.2) are defined as

$$q_{\mathrm{in,tis}} = k_{\mathrm{in}}\,(V_{\mathrm{p,tis}} + V_{\mathrm{i,tis}}) \tag{B.54}$$

$$q_{\mathrm{out,tis}} = k_{\mathrm{out}}V_{\mathrm{e,tis}}. \tag{B.55}$$

The partition coefficient $K^{\mathrm{Q:eff}}_{\mathrm{tis}}$ relates the concentration in the lumped plasma+interstitial space to the concentration leaving the compartment via plasma and lymph flow. It is defined as

$$K^{\mathrm{Q:eff}}_{\mathrm{tis}} = \frac{P_{\mathrm{tis}} \cdot K_{\mathrm{pi,tis}}}{(P_{\mathrm{tis}} - L_{\mathrm{tis}}) + L_{\mathrm{tis}}(1-\sigma_{\mathrm{L}})K_{\mathrm{i,tis}}}. \tag{B.56}$$

Assuming a quasi-steady state for $C_{\mathrm{pi,tis}}$ yields

$$C_{\mathrm{pi,tis}} = \frac{P_{\mathrm{tis}} \cdot K_{\mathrm{tis}}^{\mathrm{Q:eff}}}{P_{\mathrm{tis}} + q_{\mathrm{in,tis}} \cdot K_{\mathrm{tis}}^{\mathrm{Q:eff}}} \cdot C_{\mathrm{in,tis}} + \frac{q_{\mathrm{out,tis}}(1 - \mathrm{fu_{e,tis}}) \cdot K_{\mathrm{tis}}^{\mathrm{Q:eff}}}{P_{\mathrm{tis}} + q_{\mathrm{in,tis}} \cdot K_{\mathrm{tis}}^{\mathrm{Q:eff}}} \cdot C_{\mathrm{e,tis}}. \tag{B.57}$$

Inserting Eq. (B.57) into Eq. (B.53), we obtain

$$V_{\mathrm{e,tis}} \frac{\mathrm{d}}{\mathrm{dt}} C_{\mathrm{e,tis}} = \frac{P_{\mathrm{tis}} \cdot q_{\mathrm{in,tis}} \cdot K_{\mathrm{tis}}^{\mathrm{Q:eff}}}{P_{\mathrm{tis}} + q_{\mathrm{in,tis}} \cdot K_{\mathrm{tis}}^{\mathrm{Q:eff}}} \left(C_{\mathrm{in,tis}} - \frac{C_{\mathrm{e,tis}}}{K_{\mathrm{e,tis}}} \right) - \mathrm{CL_{e,tis}} \cdot \mathrm{fu_{e,tis}} \cdot C_{\mathrm{e,tis}} \tag{B.58}$$

where the endosomal-to-plasma partition coefficient $K_{\mathrm{e,tis}}$ is defined as

$$K_{\mathrm{e,tis}} = \frac{q_{\mathrm{in,tis}}}{q_{\mathrm{out,tis}}(1 - \mathrm{fu_{e,tis}})} \cdot K_{\mathrm{tis}}^{\mathrm{Q:eff}}. \tag{B.59}$$

Exploiting eqs. (B.50), (B.54) and (B.56) finally yields

$$K_{\mathrm{e,tis}} = \frac{P_{\mathrm{tis}} \cdot k_{\mathrm{in,tis}} \cdot (V_{\mathrm{p,tis}} + V_{\mathrm{i,tis}} \cdot K_{\mathrm{i,tis}})}{q_{\mathrm{out,tis}}(1 - \mathrm{fu_{e,tis}}) \cdot (P_{\mathrm{tis}} - L_{\mathrm{tis}} + L_{\mathrm{tis}}(1 - \sigma_{\mathrm{L}}) K_{\mathrm{i,tis}})}. \tag{B.60}$$

B.5.3 Tissue Extraction Ratios

The overall tissue clearance is defined as the product of the tissue extraction ratio, $\mathrm{E_{tis}}$, and the volume flow perfusing the compartment. In the detailed PBPK model, elimination takes place in the endosomal compartment of each tissue. Denoting the permeability rate given in eq. (B.58) as D_{tis}, i.e.,

$$D_{\mathrm{tis}} = \frac{P_{\mathrm{tis}} \cdot q_{\mathrm{in,tis}} \cdot K_{\mathrm{tis}}^{\mathrm{Q:eff}}}{P_{\mathrm{tis}} + q_{\mathrm{in,tis}} \cdot K_{\mathrm{tis}}^{\mathrm{Q:eff}}} = \frac{P_{\mathrm{tis}} \cdot k_{\mathrm{in,tis}} (V_{\mathrm{p,tis}} + V_{\mathrm{i,tis}} \cdot K_{\mathrm{i,tis}})}{P_{\mathrm{tis}} + k_{\mathrm{in,tis}} (V_{\mathrm{p,tis}} + V_{\mathrm{i,tis}} \cdot K_{\mathrm{i,tis}})}. \tag{B.61}$$

We remark that D_{tis} given in eq. (2.114) is a rearranged version of D_{tis} stated above. Assuming a quasi-steady state for the endosomal concentration $C_{\mathrm{e,tis}}$ yields

$$\mathrm{fu_{e,tis}} \cdot \mathrm{CL_{e,tis}} \cdot C_{\mathrm{e,tis}} = D_{\mathrm{tis}} \frac{K_{\mathrm{e,tis}} \cdot \mathrm{fu_{e,tis}} \cdot \mathrm{CL_{e,tis}}}{D_{\mathrm{tis}} + K_{\mathrm{e,tis}} \cdot \mathrm{fu_{e,tis}} \cdot \mathrm{CL_{e,tis}}} \cdot C_{\mathrm{in,tis}} \tag{B.62}$$

and finally

$$\text{Overall tissue clearance} = D_{\mathrm{tis}} \cdot \mathrm{E_{tis}} = D_{\mathrm{tis}} \cdot \frac{K_{\mathrm{e,tis}} \cdot \mathrm{fu_{e,tis}} \cdot \mathrm{CL_{e,tis}}}{D_{\mathrm{tis}} + K_{\mathrm{e,tis}} \cdot \mathrm{fu_{e,tis}} \cdot \mathrm{CL_{e,tis}}}. \tag{B.63}$$

Bibliography

[1] Sheiner L.B., Steimer J.L. (2000) Pharmacokinetic/pharmacodynamic modeling in drug development. *Annual Review of Pharmacology and Toxicology*, 40:67–95.

[2] Meibohm B., Derendorf H. (2002) Pharmacokinetic/pharmacodynamic studies in drug product development. *Journal of Pharmaceutical Sciences*, 91:18–31.

[3] Hood L., Perlmutter R.M. (2004) The impact of systems approaches on biological problems in drug discovery. *Nature Biotechnology*, 22:1215–1217.

[4] Burman C.F., Hamrén B., Olsson P. (2005) Modelling and simulation to improve decision-making in clinical development. *Pharmaceutical Statistics*, 4:47–58.

[5] Lalonde R.L., Kowalski K.G., Hutmacher M.M., Ewy W., Nichols D.J., Milligan P.A., Corrigan B.W., Lockwood P.A., Marshall S.A., Benincosa L.J., Tensfeldt T.G., Parivar K., Amantea M., Glue P., Koide H., Miller R. (2007) Model-based drug development. *Clinical Pharmacology and Therapeutics*, 82:21–32.

[6] Jones H.M., Gardner I.B., Watson K.J. (2009) Modelling and PBPK simulation in drug discovery. *The AAPS Journal*, 11:155–166.

[7] Derendorf H., Lesko L.J., Chaikin P., Colburn W.A., Lee P., Miller R., Powell R., Rhodes G., Stanski D., Venitz J. (2000) Pharmacokinetic/pharmacodynamic modeling in drug research and development. *Journal of Clinical Pharmacology*, 40:1399–1418.

[8] Schoenwald R.D. (2002) *Pharmacokinetics in Drug Discovery and Development*. CRC Press.

[9] Tozer T.N., Rowland M. (2006) *Introduction to Pharmacokinetics and Pharmacodynamics*. Lippincott Williams & Wilkins.

[10] Gabrielsson J., Weiner D. (2000) *Pharmacokinetic and Pharmacodynamic Data Analysis: Concepts and Applications*. Swedish Pharmaceutical Press.

[11] Benet L.Z. (1984) Pharmacokinetics: Basic principles and its use as a tool in drug metabolism. Mitchell J.R., Horning M.G. (eds.), *Drug Metabolism and Drug Toxicity*, Raven Press New York.

[12] Bonate P.L. (2005) *Pharmacokinetic-Pharmacodynamic Modeling and Simulation*. Springer Verlag.

[13] Kwon Y. (2001) *Handbook of Essential Pharmacokinetics, Pharmacodynamics, and Drug Metabolism for Industrial Scientists*. Kluwer Academic/Plemun Publishers.

[14] Lavé T., Parrott N., Grimm H.P., Fleury A., Reddy M. (2007) Challenges and opportunities with modelling and simulation in drug discovery and drug development. *Xenobiotica*, 37:1295–1310.

[15] Danhof M., De Jongh J., De Lange E., Della Pasqua O., Ploeger B.A., Voskuyl R.A. (2007) Mechanism-based pharmacokinetic-pharmacodynamic modeling: Biophase distribution, receptor theory, and dynamical systems analysis. *Annual Review of Pharmacology and Toxicology*, 47:357–400.

[16] Lüpfert C., Reichel A. (2005) Development and application of physiologically based pharmacokinetic modeling tools to support drug discovery. *Chemistry and Biodiversity*, 2:1462–1486.

[17] Nestorov I.A. (2003) Whole body pharmacokinetic models. *Clinical Pharmacokinetics*, 42:883–908.

[18] Cho C.R., Labow M., Reinhardt M., Van Oostrum J., Peitsch M.C. (2006) The application of systems biology to drug discovery. *Current Opinion in Chemical Biology*, 10:294–302.

[19] Schmitt W., Willmann S. (2005) Physiology-based pharmacokinetic modeling: Ready to be used. *Drug Discovery Today: Technologies*, 2:125–132.

[20] Theil F.P., Guentert T.W., Haddad S., Poulin P. (2003) Utility of physiologically based pharmacokinetic models to drug development and rational drug discovery candidate selection. *Toxicology Letters*, 138:29–49.

[21] Jones H.M., Parrott N., Jorga K., Lavé T. (2006) A novel strategy for physiologically based predictions of human pharmacokinetics. *Clinical Pharmacokinetics*, 45:511–542.

[22] Mager D.E., Wyska E., Jusko W.J. (2003) Diversity of mechanism-based pharmacodynamic models. *Drug Metabolism and Disposition*, 31:510–518.

[23] Csajka C., Verotta D. (2006) Pharmacokinetic-pharmacodynamic modelling: History and perspectives. *Journal of Pharmacokinetics and Pharmacodynamics*, 33:227–279.

[24] Danhof M., Alvan G., Dahl S.G., Kuhlmann J., Paintaud G. (2005) Mechanism-based pharmacokinetic–pharmacodynamic modeling - a new classification of biomarkers. *Pharmaceutical Research*, 22:1432–1437.

[25] Levy G. (1964) Relationship between elimination rate of drugs and rate of decline of their pharmacological effect. *Journal of Pharmaceutical Sciences*, 53:342–343.

[26] Levy G. (1966) Kinetics of pharmacologic effects. *Clinical Pharmacology and Therapeutics*, 7:362–372.

[27] Butcher E.C., Berg E.L., Kunkel E.J. (2004) Systems biology in drug discovery. *Nature Biotechnology*, 22:1253–1259.

[28] Kell D.B. (2006) Systems biology, metabolic modelling and metabolomics in drug discovery and development. *Drug Discovery Today*, 11:1085–1092.

[29] Nestorov I.A., Aarons L.J., Arundel P.A:, Rowland M. (1998) Lumping of whole-body physiologcally based pharmacokinetic models. *Journal of Pharmacokinetics and Pharmacodynamics*, 26:21–46.

[30] Brochot C., Toth J., Bois F.Y. (2005) Lumping in pharmacokinetics. *Journal of Pharmacokinetics and Pharmacodynamics*, 32:719–736.

[31] Gueorguieva I., Nestorov I.A., Rowland M. (2006) Reducing whole body physiologically based pharmacokinetic models using global sensitivity analysis: Diazepam case study. *Journal of Pharmacokinetics and Pharmacodynamics*, 33:1–27.

[32] Björkman S. (2003) Reduction and lumping of physiologically based pharmacokinetic models: Prediction of the disposition of fentanyl and pethidine in human by successively simplified models. *Journal of Pharmacokinetics and Pharmacodynamics*, 30:285–307.

[33] Bourne D.W.A. (1995) *Mathematical Modeling of Pharmacokinetic Data*. Technomic Publishing Company, Inc.

[34] Kumar A., Takada Y., Boriek A.M., Aggarwal B.B. (2004) Nuclear factor κB: Its role in health and disease. *Journal of Molecular Medicine*, 82:434–448.

[35] Hoffmann A., Natoli G., Ghosh G. (2006) Transcriptional regulation via the NFκB signaling module. *Oncogene*, 25:6706–6716.

[36] Gilmore T.D. (2006) Introduction to NF-κB: Players, pathways, perspectives. *Oncogene*, 25:6680–6684.

[37] Blackwell T.S., Christman J.W. (1997) The role of nuclear factor κB in cytokine gene regulation. *American Journal of Respiratory Cell and Molecular Biology*, 17:3–9.

[38] Pande J., Ramos M.J. (2005) NF-κB in human disease: Current inhibitors and prospects for de novo structure based design of inhibitors. *Current Medicinal Chemistry*, 12:357–374.

[39] Karin M., Yamamoto Y., Wang Q.M. (2004) The IKK NF-κB system: A treasure trove for drug development. *Nature Reviews Drug Discovery*, 3:17–26.

[40] Bamborough P., Callahan J.F., Christopher J.A., Kerns J.K., Liddle J., Miller D.D., Morse M.A., Rumsey W.L., Williamson R. (2009) Progress towards the development of anti-inflammatory inhibitors of IKKβ. *Current Topics in Medicinal Chemistry*, 9:623–639.

[41] Karin M., Ben-Neriah Y. (2000) Phosphorylation meets ubiquitination: The control of NF-κB activity. *Annual Review of Immunology*, 18:621–663.

[42] Moynagh P. (2005) The NFκB pathway. *Journal of Cell Science*, 118:4389–4392.

[43] Ghosh S., May M.J., Kopp E.B. (1998) NFκB and rel proteins: Evolutionarily conserved mediators of immune responses. *Annual Review of Immunology*, 16:225–260.

[44] Xiao W. (2004) Advances in NFκB signaling transduction and transcription. *Cellular & Molecular Immunology*, 1:425–435.

[45] Hoffmann A., Levchenko A., Scott M.L., Baltimore D. (2002) The IκB-NF-κB signaling module: Temporal control and selective gene activation. *Science*, 298:1241–1245.

[46] Cheong R., Bergmann A., Werner S.L., Regal J., Hoffmann A., Levchenko A. (2005) Transient IκB kinase activity mediates temporal NF-κB dynamics in response to a wide range of tumor necrosis factor-α doses. *Journal of Biological Chemistry*, 281:2945–2950.

[47] Werner S.L., Barken D., Hoffmann A. (2005) Stimulus specificity of gene expression programs determined by temporal control of IKK activity. *Science*, 309:1857–1861.

[48] Kearns J.D., Basak S., Werner S.H., Huang C.S., Hoffmann A. (2006) IκBϵ provides negative feedback to control NF-κB oscillations, signaling dynamics, and inflammatory gene expression. *Journal of Cell Biology*, 173:659–664.

[49] O'Dea E.L., Barken D., Peralta R.Q., Tran K.T., Werner S.L., Kearns J.D., Levchenko A., Hoffmann A. (2007) A homeostatic model of IκB metabolism to control constitutive NF-κB activity. *Molecular Systems Biology*, 3:1–7.

[50] Pilari S. (2008) *Influence of the Dynamics of IKK Activation and Inactivation on the NFκB Signaling Pathway.* Master's thesis, Freie Universität Berlin.

[51] Dahl S.G., Aarons L.J., Gundert-Remy U., Karlsson M., Schneider Y.J., Steimer J.L., Troconiz I.F. (2009) Incorporating physiological and biochemical mechanisms into pharmacokinetic–pharmacodynamic models: A conceptual framework. *Basic and Clinical Pharmacology and Toxicology*, 106:2–12.

[52] Weiss M. (1996) A novel extravascular input function for the assessment of drug absorption in bioavailability studies. *Pharmaceutical Research*, 13:1547–1553.

[53] Yu L.X., Amidon G.L. (1999) A compartmental absorption and transit model for estimating oral drug absorption. *International Journal of Pharmaceutics*, 186:119–125.

[54] Sawamoto T., Haruta S., Kurosaki Y., Higaki K., Kimura T. (1997) Prediction of the plasma concentration profiles of orally administered drugs in rats on the basis of gastrointestinal transit kinetics and absorbability. *Journal of Pharmacokinetics and Pharmacodynamics*, 49:450–457.

[55] Kimura T., Higaki K. (2002) Gastrointestinal transit and drug absorption. *Biological and Pharmaceutical Bulletin*, 25:149–164.

[56] International Commission on Radiological Protection (ICRP) (2002) Basic anatomical and physiological data for use in radiological protection: Reference values. *ICRP Publication 89.*

[57] National Center for Health Statistics Hyattsville, USA (1997), Third national health and nutrition examination survey (NHANES III). http://www.cdc.gov/nchs/nhanes.htm.

[58] Brown R.P., Delp M.D., Lindstedt S.L., Rhomberg L.R., Beliles R.P. (1997) Physiological parameter values for physiologically based pharmacokinetic models. *Toxicology and Industrial Health*, 13:407–484.

[59] Rodgers T., Leahy D., Rowland M. (2005) Physiologically based pharmacokinetic modeling 1: Predicting the tissue distribution of moderate-to-strong bases. *Journal of Pharmaceutical Sciences*, 94:1259–1276.

[60] Rodgers T., Leahy D., Rowland M. (2007) Errata: Physiologically based pharmacokinetic modeling 1: Predicting the tissue distribution of moderate-to-strong bases. *Journal of Pharmaceutical Sciences*, 96:3151–3152.

[61] Rodgers T., Rowland M. (2006) Physiologically based pharmacokinetic modelling 2: Predicting the tissue distribution of acids, very weak bases, neutrals and zwitterions. *Journal of Pharmaceutical Sciences*, 95:1238–1257.

[62] Rodgers T., Rowland M. (2007) Errata: Physiologically based pharmacokinetic modelling 2: Predicting the tissue distribution of acids, very weak bases, neutrals and zwitterions. *Journal of Pharmaceutical Sciences*, 96:3153–3154.

[63] Poulin P., Theil F.P. (2009) Development of a novel method for predicting human volume of distribution at steady-state of basic drugs and comparative assessment with existing methods. *Journal of Pharmaceutical Sciences*, 9999:1–29.

[64] Obach R.S. (1999) Prediction of human clearance of twenty-nine drugs from hepatic microsomal intrinsic clearance data: An examination of in vitro half-life approach and nonspecific binding to microsomes. *Drug Metabolism and Disposition*, 27:1350–1359.

[65] Riley R.J., McGinnity D.F., Austin R.P. (2005) A unified model for predicting human hepatic, metabolic clearance from in vitro intrinsic clearance data in hepatocytes and microsomes. *Drug Metabolism and Disposition*, 33:1304–1311.

[66] Rodgers T., Rowland M. (2007) Mechanistic approaches to volume of distribution predictions: Understanding the process. *Pharmaceutical Research*, 24:918–933.

[67] Jones H.M., Houston J.B. (2004) Substrate depletion approach for determining in vitro metabolic clearance: Time dependencies in hepatocyte and microsomal incubations. *Drug Metabolism and Disposition*, 32.

[68] Drugbank (28-01-2010) Diclofenac. *http://drugbank.ca/drugs/DB00586*.

[69] Drugbank (28-01-2010) Warfarin. *http://www.drugbank.ca/drugs/DB00682*.

[70] Jung D., Mayersohn M., Perrier D., Calkins J., Saunders R. (1982) Thiopental disposition in lean and obese patients undergoing surgery. *Anesthesiology*, 56:269–274.

[71] Russo H., Simon N., Duboin M.P., Urien S. (1997) Population pharmacokinetics of high-dose thiopental in patients with cerebral injuries. *Clinical Pharmacology and Therapeutics*, 62:15–20.

[72] Löscher W. (1978) Serum protein binding and pharmacokinetics of valproate in man, dog, rat and mouse. *The Journal of Pharmacology and Experimental Therapeutics*, 204:255–261.

[73] Poulin P., Theil F.P. (2000) A priori prediction of tissue:plasma partition coefficients of drugs to facilitate the use of physiologically-based pharmacokinetic models in drug discovery. *Journal of Pharmaceutical Sciences*, 89:16–35.

[74] Poulin P., Schoenlein K., Theil F.P. (2001) Prediction of adipose tissue:plasma partition coefficients for structurally unrelated drugs. *Journal of Pharmaceutical Sciences*, 90:436–447.

[75] Willmann S., Lippert J., Schmitt W. (2005) From physicochemistry to absorption and distribution: Predictive mechanistic modelling and computational tools. *Expert Opinion on Drug Metabolism and Toxicology*, 1:159–168.

[76] Blakey G.E., Nestorov I.A., Arundel P.A., Aarons L.J., Rowland M. (1997) Quantitative structure pharmacokinetics relationship I: Development of a whole-body physiologically based pharmacokinetic model to characterize changes in pharmacokinetics across a homologous series of barbiturates in the rat. *Journal of Pharmacokinetics and Biopharmaceutics*, 25:277–312.

[77] U.S. Food and Drug Administration (2004) Lidocaine. *NDA 8-816/S-032*.

[78] Greenblatt D.J., Bolognini V., Koch-Weser J., Harmatz J.S. (1976) Pharmacokinetic approach to the clinical use of lidocaine intravenously. *The Journal of the American Medical Association*, 236:273–277.

[79] Bernhard C.G., Bohm E., Hojeberg S. (1955) A new treatment of status epilepticus: Intravenous injections of a local anesthetic (Lidocaine). *Archives of Neurology and Psychiatry*, 74:208–214.

[80] Hattori H., Yamano T., Hayashi K., Osawa M., Kondo K., Aihara M., Haginoya K., Hamano S., Izumi T., Kaneko K., et al. (2008) Effectiveness of lidocaine infusion for status epilepticus in childhood: A retrospective multi-institutional study in japan. *Brain and Development*, 30:504–512.

[81] Tucker G.T., Boas R.A. (1971) Pharmacokinetic aspects of intravenous regional anesthesia. *Anesthesiology*, 34:538–549.

[82] Boyes R.N., Adams H.J., Duce B.R. (1970) Oral absorption and disposition kinetics of lidocaine hydrochloride in dogs. *The Journal of Pharmacology and Experimental Therapeutics*, 174:1–8.

[83] Adjepon-Yamoah K.K., Scott D.B., Prescott L.F. (1974) The effect of atropine on the oral absorption of lidocaine in man. *European Journal of Clinical Pharmacology*, 7:397–400.

[84] Burm A.G.L., Van Kleef J.W., Spierdijk J., De Boer A.G., Vermeulen N.P.E., De Leede L.G.J., Breimer D.D. (1988) Pharmacokinetics of Lidocaine and Bupivacaine and stable isotope labelled analogues: A study in healthy volunteers. *Biopharmaceutics and Drug Disposition*, 9:85–95.

[85] von Kleist M., Huisinga W. (2007) Physiologically based pharmacokinetic modelling: A sub-compartmentalized model of tissue distribution. *Journal of Pharmacokinetics and Pharmacodynamics*, 34:789–806.

[86] Berezhkovskiy L.M. (2004) Volume of distribution at steady state for a linear pharmacokinetic system with peripheral elimination. *Journal of Pharmaceutical Sciences*, 93:1628–1640.

[87] Yates J.W.T., Arundel P.A. (2008) On the volume of distribution at steady state and its relationship with two-compartmental models. *Journal of Pharmaceutical Sciences*, 97:111–122.

[88] Heizmann P., Eckert M., Ziegler W.H. (1983) Pharmacokinetics and bioavailability of midazolam in man. *British Journal of Clinical Pharmacology*, 16:43–49.

[89] Zomorodi K., Donner A., Somma J., Barr J., Sladen R., Ramsay J., Geller E., Shafer S.L. (1998) Population pharmacodynamics of midazolam administered by target controlled infusion for sedation following coronary artery bypass grafting. *Anesthesiology*, 89:1418–1429.

[90] Swart E.L., Zuideveld K.P., de Jongh J., Danhof M., Thijs L.G., van Schijndel R.M.J.S. (2003) Comparative population pharmacokinetics of lorazepam and midazolam during long-term continuous infusion in critically ill patients. *British Journal of Clinical Pharmacology*, 57:135–145.

[91] Stanski D.R., Maitre P.O: (1990) Population pharmacokinetics and pharmacodynamics of thiopental: The effect of age revisited. *Anesthesiology*, 72:399–402.

[92] Gugler R., Schell A., Eichelbaum M., Fröscher W., Schulz H.U. (1977) Disposition of valproic acid in man. *European Journal of Clinical Pharmacology*, 12:125–132.

[93] Blanco-Serrano B., Otero MJ, Santos-Buelga D., Garcia-Sanchez MJ, Serrano J., Dominguez-Gil A. (1999) Population estimation of valproic acid clearance in adult patients using routine clinical pharmacokinetic data. *Biopharmaceutics and Drug Disposition*, 20:233–240.

[94] Rostami-Hodjegan A., Peacey S.R., George E., Heller S.R., Tucker G.T. (1998) Population-based modeling to demonstrate extrapancreatic effects of tolbutamide. *American Journal of Physiology - Endocrinology And Metabolism*, 274:758–771.

[95] Price P.S., Conolly R.B., Chaisson C.F., Gross E.A., Young J.S., Mathis E.T., Tedder D.R. (2003) Modeling interindividual variation in physiological factors used in PBPK models of humans. *Critical Reviews in Toxicology*, 33:469–503.

[96] Willmann S., Höhn K., Edginton A., Sevestre M., Solodenko J., Weiss W., Lippert J., Schmitt W. (2007) Development of a physiologically-based whole-body population model for assessing the influence of individual variability on the pharmacokinetics of drugs. *Journal of Pharmacokinetics and Pharmacodynamics*, 34:401–431.

[97] Ette E.I., Williams P.J. (2007) *Pharmacometrics: The science of quantitative pharmacology*. John Wiley & Sons.

[98] U.S. Food and Drug Administration (1999) *Guidance for Industry: Population Pharmacokinetics.*

[99] Ribbing J., Jonsson E.N. (2004) Power, selection bias and predictive performance of the population pharmacokinetic covariate model. *Journal of Pharmacokinetics and Pharmacodynamics*, 31:109–134.

[100] Pilari S., Solms A., Fronton L., Huisinga W. A mechanistic approach to covariate modelling, in preparation.

[101] Keizer R., Huitema A.D.R., Schellens J.H.M., Beijnen J.H. (2010) Clinical pharmacokinetics of therapeutic monoclonal antibodies. *Clinical Pharmacokinetics*, 49:493–507.

[102] European Medicines Agency (EMEA) (2007) *Guideline on the clinical investigation of the pharmacokinetics of therapeutic proteins.*

[103] Lu J.F., Bruno R., Eppler S., Novotny W., Lum B., Gaudreault J. (2008) Clinical pharmacokinetics of bevacizumab in patients with solid tumors. *Cancer Therapy and Pharmacology*, 62:779–786.

[104] Wiczling P., Rosenzweig M., Vaickus L., Jusko W.J. (2010) Pharmacokinetics and pharmacodynamics of a chimeric/humanized anti-CD3 monoclonal antibody, Otelixizumab (TRX4), in subjects with psoriasis and with type 1 diabetes mellitus. *The Journal of Clinical Pharmacology*, 50:494–506.

[105] Dirks N.L., Nolting A., Kovar A., Meibohm B. (2008) Population pharmacokinetics of cetuximab in patients with squamous cell carcinoma of the head and neck. *The Journal of Clinical Pharmacology*, 48:267–278.

[106] Azzopardi N., Lecomte T., Ternant D., Piller F., Ohresser M., Watier H., Gamelin E., Paintaud G. (2010) Population pharmacokinetics and exposition-PFS relationship of Cetuximab in metastatic colorectal cancer. *Population Approach Group Meeting.*

[107] Lammerts van Bueren J.J., Bleeker W.K., Bogh H.O., Houtkamp M., Schuurman J., van de Winkel J.G.J., Parren P.W.H.I. (2006) Effect of target dynamics on pharmacokinetics of a novel therapeutic antibody against the epidermal growth factor receptor: Implications for the mechanisms of action. *Cancer Research*, 66:7630–7638.

[108] Mager D.E., Jusko W.J. (2001) General pharmacokinetic model for drugs exhibiting target-mediated drug disposition. *Journal of Pharmacokinetics and Pharmacodynamics*, 28:507–532.

[109] Mager D.E., Krzyzanski W. (2005) Quasi-equilibrium pharmacokinetic model for drugs exhibiting target-mediated drug disposition. *Pharmaceutical Research*, 22:1589–1596.

[110] Gibiansky L., Gibiansky E., Kakkar T., Ma P. (2008) Approximations of the target-mediated drug disposition model and identifiability of model parameters. *Journal of Pharmacokinetics and Pharmacodynamics*, 35:573–591.

[111] Grimm H.P. (2009) Gaining insights into the consequences of target-mediated drug disposition of monoclonal antibodies using quasi-steady-state approximations. *Journal of Pharmacokinetics and Pharmacodynamics*, 36:407–420.

[112] Krippendorff B.F., Kuester K., Kloft C., Huisinga W. (2009) Nonlinear pharmacokinetics of therapeutic proteins resulting from receptor mediated endocytosis. *Journal of Pharmacokinetics and Pharmacodynamics*, 36:239–260.

[113] Hansen R.J., Balthasar J.P. (2003) Pharmacokinetic/pharmacodynamic modeling of the effects of intravenous immunoglobulin on the disposition of antiplatelet antibodies in a rat model of immune thrombocytopenia. *Journal of Pharmaceutical Sciences*, 92:1206–1215.

[114] Garg A., Balthasar J.P. (2007) Physiologically-based pharmacokinetic (PBPK) model to predict IgG tissue kinetics in wild-type and FcRn-knockout mice. *Journal of Pharmacokinetics and Pharmacodynamics*, 34:687–709.

[115] Baxter L.T., Zhu H., Mackensen D.G., Jain R.K. (1994) Physiologically based pharmacokinetic model for specific and nonspecific monoclonal antibodies and fragments in normal tissues and human tumor xenografts in nude mice. *Cancer Research*, 54:1517–1528.

[116] Davda J.P., Jain M., Batra S.K., Gwilt P.R., Robinson D.H. (2008) A physiologically based pharmacokinetic (PBPK) model to characterize and predict the disposition of monoclonal antibody CC49 and its single chain Fv constructs. *International Immunopharmacology*, 8:401–413.

[117] Covell D.G., Barbet J., Holton O.D., Black C.D.V., Parker RJ, Weinstein J.N. (1986) Pharmacokinetics of monoclonal immunoglobulin G_1, $F(ab')_2$, and Fab' in mice. *Cancer Research*, 46:3969–3978.

[118] Popov S., Hubbard J.G., Kim J.K., Ober B., Ghetie V., Ward E.S. (1996) The stoichiometry and affinity of the interaction of murine Fc fragments with the MHC class I-related receptor, FcRn. *Molecular Immunology*, 33:521–530.

[119] El-Masri H.A., Portier C.J. (1998) Physiologically based pharmacokinetics model of primidone and its metabolites phenobarbital and phenylethylmalonamide in humans, rats, and mice. *Drug Metabolism and Disposition*, 26:585–594.

[120] Davies B., Morris T. (1993) Physiological parameters in laboratory animals and humans. *Pharmaceutical Research*, 10:1093–1095.

[121] Kawai R., Lemaire M., Steimer J.L., Bruelisauer A., Niederberger W., Rowland M. (1994) Physiologically based pharmacokinetic study on a cyclosporine derivative, SDZ IMM 125. *Journal of Pharmacokinetics and Pharmacodynamics*, 22:327–365.

[122] Junghans R.P., Anderson C.L. (1996) The protection receptor for IgG catabolism is the β_2-microglobulin-containing neonatal intestinal transport receptor. *Proceedings of the National Academy of Sciences of the United States of America*, 93:5512–5516.

[123] Pilari S., Fronton L., Huisinga W. (2011) Monoclonal antibody disposition beyond target binding: Impact of FcRn on clearance and derivation of mechanistic compartment models, submitted.

[124] Kola I., Landis J. (2004) Can the pharmaceutical industry reduce attrition rates? *Nature Reviews Drug Discovery*, 3:711–716.

[125] Wagner J.G. (1968) Kinetics of pharmacologic response I. Proposed relationships between response and drug concentration in the intact animal and man. *Journal of Theoretical Biology*, 20:173–201.

[126] Sheiner L.B., Stanski D.R., Vozeh S., Miller R.D., Ham J. (1979) Simultaneous modeling of pharmacokinetics and pharmacodynamics: application to d-tubocurarine. *Clinical Pharmacology and Therapeutics*, 25:358–371.

[127] Kanehisa M. (2002) The KEGG database at GenomeNet. *Nucleic Acids Research*, 30:42–46.

[128] Le Novere N., Bornstein B., Broicher A., Courtot M., Donizelli M., Dharuri H., Li L., Sauro H., Schilstra M., Shapiro B., Snoep J.L., Hucka M. (2006) Biomodels database: A free, centralized database of curated, published, quantitative kinetic models of biochemical and cellular systems. *Nucleic Acids Research*, 34:D689–D691.

[129] Ronen M., Rosenberg R., Shraiman B.I., Alon U. (2002) Assigning numbers to the arrows: parameterizing a gene regulation network by using accurate expression kinetics. *Proceedings of the National Academy of Sciences of the United States of America*, 99:10555–10560.

[130] Kreutz C., Timmer J. (2009) Systems biology: Experimental design. *FEBS Journal*, 276:923–942.

[131] Held M., Metzner P., Prinz J.H., Noé F. (2011) Mechanisms of protein-ligand association and its modulation by protein mutations. *Biophysical Journal*, 100:701–710.

[132] Baldwin A.S. (2001) Series introduction: The transcription factor NF-κB and human disease. *Journal of Clinical Investigation*, 107:3–6.

[133] Hoffmann A., Baltimore D. (2006) Circuitry of nuclear factor κB signaling. *Immunological Reviews*, 210:171–186.

[134] Hayden M.S., Ghosh S. (2008) Shared principles in NF-κB signaling. *Cell*, 132:344–362.

[135] Malek S., Chen Y., Huxford T., Ghosh G. (2001) IκBβ, but not IκBα, functions as a classical cytoplasmic inhibitor of NF-κB dimers by masking both NF-κB nuclear localization sequences in resting cells. *Journal of Biological Chemistry*, 276:45225–45235.

[136] Huang T.T., Kudo N., Yoshida M., Miyamoto S. (2000) A nuclear export signal in the N-terminal regulatory domain of IκBα controls cytoplasmic localization of inactive NF-κB/IκBα complexes. *Proceedings of the National Academy of Sciences of the United States of America*, 97:1014–1019.

[137] Li Z.W., Chu W., Hu Y., Delhase M., Deerinck T., Ellisman M., Johnson R., Karin M. (1999) The IKKβ subunit of IκB kinase (IKK) is essential for nuclear factor κB activation and prevention of apoptosis. *Journal of Experimental Medicine*, 189:1839–1845.

[138] Karin M. (1999) How NF-κB is activated: The role of the IκB kinase (IKK) complex. *Oncogene*, 18:6867–6874.

[139] Delhase M., Hayakawa M., Chen Y., Karin M. (1999) Positive and negative regulation of IκB kinase activity through IKK subunit phosphorylation. *Science*, 284:309–313.

[140] Rothwarf D.M., Zandi E., Natoli G., Karin M. (1998) IKK-γ is an essential regulatory subunit of the IκB kinase complex. *Nature*, 395:297–300.

[141] Martin M.U., Wesche H. (2002) Summary and comparison of the signaling mechanisms of the Toll/Interleukin-1 receptor family. *Biochimica et Biophysica Acta*, 1592:265–280.

[142] Baud V., Liu Z.G., Bennett B., Suzuki N., Xia Y., Karin M. (1999) Signaling by proinflammatory cytokines: Oligomerization of TRAF2 and TRAF6 is sufficient for JNK and IKK activation and target gene induction via an amino-terminal effector domain. *Genes and Development*, 13:1297–1308.

[143] Yang J., Lin Y., Guo Z., Cheng J., Huang J., Deng L., Liao W., Chen Z., Liu Z., Su B. (2001) The essential role of MEKK3 in TNF-induced NF-κB activation. *Nature Immunology*, 2:620–624.

[144] Bourke E., Kennedy E.J., Moynagh P.N. (2000) Loss of IκB-β is associated with prolonged NF-κB activity in human glial cells. *Journal of Biological Chemistry*, 275:39996–40002.

[145] Arenzana-Seisdedos F., Turpin P., Rodriguez M., Thomas D., Hay R.T., Virelizier J.L., Dargemont C. (1997) Nuclear localization of IκBα promotes active transport of NF-κB from the nucleus to the cytoplasm. *Journal of Cell Science*, 110:369–378.

[146] Griffin B.D., Moynagh P.N. (2006) Persistent Interleukin-1β signaling causes long term activation of NFκB in a promoter-specific manner in human glial cells. *Journal of Biological Chemistry*, 281:10316–10326.

[147] Suyang H., Phillips R., Douglas I., Ghosh S. (1996) Role of unphosphorylated, newly synthesized IκBβ in persistent activation of NF-κB. *Molecular and Cellular Biology*, 16:5444–5449.

[148] Yamamoto Y., Gaynor R.B. (2001) Therapeutic potential of inhibition of the NF-κB pathway in the treatment of inflammation and cancer. *Journal of Clinical Investigation*, 107:135–142.

[149] Tak P.P., Firestein G.S. (2001) NFκB: A key role in inflammatory diseases. *The Journal of Clinical Investigation*, 107:7–11.

[150] Hoffmann A. (2009). Personal Communication.

[151] Heilker R., Freuler F., Vanek M., Pulfer R., Kobel T., Peter J., Zerwes H.G., Hofstetter H., Eder J. (1999) The kinetics of association and phosphorylation of IκB isoforms by IκB kinase 2 correlate with their cellular regulation in human endothelial cells. *Biochemistry*, 38:6231–6238.

[152] Zandi E., Chen Y.I., Karin M. (1998) Direct phosphorylation of IκB by IKKα and IKKβ: Discrimination between free and NF-κB-bound substrate. *Science*, 281:1360–1363.

[153] Nomenclature Committee of the International Union of Biochemistry (NC-IUB) (1979) Units of enzyme activity: Recommendations 1978. *European Journal of Biochemistry*, 97:319–320.

[154] Baldwin A.S. (2001) Control of oncogenesis and cancer therapy resistance by the transcription factor NF-κB. *Journal of Clinical Investigation*, 107:241–246.

[155] Nabel G., Baltimore D. (1987) An inducible transcription factor activates expression of human immunodeficiency virus in T cells. *Nature*, 326:711–713.

[156] Hiscott J., Kwon H., Genin P. (2001) Hostile takeovers: Viral appropriation of the NF-κB pathway. *Journal of Clinical Investigation*, 107:143–151.

[157] Yin M.J., Yamamoto Y., Gaynor R.B. (1998) The anti-inflammatory agents aspirin and salicylate inhibit the activity of IκB kinase-β. *Nature*, 396:77–80.

[158] Kopp E.B., Ghosh S. (1994) Inhibition of NF-κB by sodium salicylate and aspirin. *Science*, 265:956–959.

[159] Palayoor S.T., Youmell M.Y., Calderwood S.K., Coleman C.N., Price B.D. (1999) Constitutive activation of IκB kinase α and NF-κB in prostate cancer cells is inhibited by ibuprofen. *Oncogene*, 18:7389–7394.

[160] Yamamoto Y., Yin M.J., Lin K.M., Gaynor R.B. (1999) Sulindac inhibits activation of the NF-κB pathway. *Journal of Biological Chemistry*, 274:27307–27314.

[161] Wahl C., Liptay S., Adler G., Schmid R.M. (1998) Sulfasalazine: A potent and specific inhibitor of Nuclear Factor Kappa B. *Journal of Clinical Investigation*, 101:1163–1174.

[162] Keifer J.A., Guttridge D.C., Ashburner B.P., Baldwin Jr. A.S. (2001) Inhibition of NF-κB activity by thalidomide through suppression of IκB kinase activity. *Journal of Biological Chemistry*, 276:22382–22387.

[163] Luby-Phelps K. (2000) Cytoarchitecture and physical properties of cytoplasm: Volume, viscosity, diffusion, intracellular surface area. *International Review of Cytology*, 192:189–221.

[164] Cheong R., Bergmann A., Werner S.L., Regal J., Hoffmann A., Levchenko A. (2005) Transient IκB kinase activity mediates temporal NF-κB dynamics in response to a wide range of tumor necrosis factor-α doses. supplemental data. *Journal of Biological Chemistry*, 281:2945–2950.

[165] Voet D., Voet J.G. (1995) *Biochemistry*. John Wiley & Sons.

[166] Aggarwal B.B., Sethi G., Baladandayuthapani V., Krishnan S., Shishodia S. (2007) Targeting cell signaling pathways for drug discovery: An old lock needs a new key. *Journal of Cellular Biochemistry*, 102.

[167] Arrell D.K., Terzic A. (2010) Network systems biology for drug discovery. *Clinical Pharmacology and Therapeutics*, 88:120–125.

[168] Azmi A.S., Wang Z., Philip P.A., Mohammad R.M., Sarkar F.H. (2010) Proof of concept: Network and systems biology approaches aid in the discovery of potent anticancer drug combinations. *Molecular Cancer Therapeutics*, 9:3137.

[169] U.S. Food and Drug Administration (2009) Drug safety oversight board meeting: Public summary. *http://www.fda.gov/AboutFDA/CentersOffices/CDER/ucm191353.htm*.

[170] U.S. Food and Drug Administration (2011) Systems Biology Division. *http://www.fda.gov/AboutFDA/CentersOffices/NCTR/WhatWeDo/*.

[171] Bois F.Y. (2009) Physiologically based modelling and prediction of drug interactions. *Basic and Clinical Pharmacology and Toxicology*, 106:154–161.

[172] McLeay S.C., Morrish G.A., Kirkpatrick C.M., Green B. (2009) Encouraging the move towards predictive population models for the obese using propofol as a motivating example. *Pharmaceutical Research*, 26:1626–1634.

Ehrenwörtliche Erklärung

Hiermit erkläre ich, dass ich diese Arbeit selbständig verfasst und keine anderen als die angegebenen Hilfsmittel und Quellen verwendet habe.

Berlin, den 18.02.2011

Sabine Pilari

Zusammenfassung

In der Wirkstofffindung und -entwicklung wird pharmakokinetische und pharmakodynamische Modellierung erfolgreich zur Analyse und Vorhersage des zeitlichen Verlaufes von Wirkstoffkonzentrationen und Wirkstoffeffekten im Patienten genutzt.
Zur Bestimmung der Pharmakokinetik (PK) neuer Wirkstoffe finden sowohl empirische Kompartimentmodelle als auch physiologiebasierte PK (PBPK) Modelle routinemäßig Anwendung. Bislang jedoch werden beide Modellierungsansätze nur parallel und mit wenigen Überschneidungen angewendet. Während die PBPK-Modellierung hauptsächlich genutzt wird, um die Wirkstofffindung und prä- und frühe klinische Entwicklung zu unterstützen, wird die empirische, kompartimentelle Modellierung routinemäßig zur Analyse humaner *in vivo* Daten aus klinischen Studien herangezogen. Eine Methode, die die Modellierungsstrategien aus der präklinischen und klinischen PK verbindet, ist daher von großem Interesse.
Die pharmakodynamische (PD) Modellentwicklung ist bislang hauptsächlich empirisch, obwohl Modelle mit mechanistischen Elementen und Interpretationen existieren. Die mechanistische PD-Modellierung kann von der steigenden Anzahl systembiologischer Modelle, die sowohl komplexe metabolische und genregulatorische Netzwerke als auch Signalwege detailliert beschreiben, profitieren. Die Verknüpfung von PBPK und systembiologischen PD-Modellen stellt eine neuartige Herangehensweise für die Vorhersage von zeitlichen Wirkstoffeffekten dar.

In dieser Dissertation, wird eine neue Methode zur mechanistischen Herleitung von klassischen Kompartimentmodellen entwickelt, die auf der Dimensionsreduktion von PBPK-Modellen mittels Lumping basiert. Unsere Lumping-Strategie erlaubt es, eine physiologische Interpretation der niedrigdimensionalen Modellstruktur sowie der Modellparameter beizubehalten. Damit werden die mechanistischen Kenntnisse, die im PBPK-Modell vorhanden sind, in die in späteren, klinischen Entwicklungsphasen verwendeten Kompartimentmodelle transferiert. Außerdem wird gezeigt, inwiefern die neue Lumping-Methode die mechanistische Kovariaten-Modellierung in populationspharmakokinetischen Studien unterstützt. Mittels Lumping eines PBPK-Modells, welches interindividuelle Variabilität in physiologischen Parametern, wie zum Beispiel Organvolumina und Blutflussraten, berücksichtigt, leiten wir ein allgemeingültiges, niedrigdimensionales Kompartimentmodell mit mechanistischen Kovariaten her. Wir erweitern außerdem unseren Lumping-Ansatz, um die empirische PK-Modellentwicklung für monoklonale Antikörpern zu unterstützen. Dieses Beispiel ist von besonderer Bedeutung, da es für diese Wirkstoffklasse bislang keine etablierte Strategie zur Modellentwicklung und -evaluation gibt, die mit dem existierendem Wissen über relevante molekulare Verteilungs- und Eliminationsprozesse konsistent ist.

Im letzten Teil der Dissertation zeigen wir beispielhaft, inwiefern PBPK und systembiologische Modelle miteinander verknüpft werden können, um den zeitlichen Verlauf von Wirkstoffeffekten *in vivo* vorherzusagen. Wir erläutern die Strategie am Beispiel von Wirkstoffen, die mit dem IKK-NFκB-Signalweg interagieren, um die Aktivität des inflammatorischen Biomarkers NFκB zu senken. Wir entwickeln ein neues mathematisches Modell, welches die Aktivierung und Inaktivierung von IKK, den wichtigsten Regulator von NFκB, in der Anwesenheit eines Wirkstoffes beschreibt. Durch die Integration eines bereits veröffentlichten Modells der NFκB-Aktivierung in das Modell der IKK-Regulation und die Verknüpfung der systembiologischen Modelle mit einem PBPK-Modell, können wir den zeitlichen und gewebsspezifischen Effekt eines Wirkstoffes sowohl auf IKK als auch auf NFκB vorhersagen.